

INAUGURAL-DISSERTATION

am Leibniz-Institut für Atmosphärenphysik in Kühlungsborn
zur Erlangung der Doktorwürde
der Mathematisch-Naturwissenschaftlichen Fakultät
der Universität Rostock

Investigation of gravity waves with VHF radar measurements

von
Andrei Serafimovich

Abstract: Temporal and spatial behaviour of gravity waves is investigated based on continuous radar measurements of zonal and meridional winds. Gravity wave parameters have been estimated at different locations separately and by a complex cross-spectral analysis of the data of collocated radars. A case study carried out in a region with no large orography (Northern Germany) at Kühlungsborn (54.1°N , 11.8°E) and Lindenberg (52.2°N , 14.1°E) shows the appearance of strong inertia-gravity waves in connection with Rossby wave breaking events. Two kinds of gravity waves occurring simultaneously are detected. One wave is generated by a jet stream in the tropopause region, leading to a downward energy propagation in the troposphere and moving against the mean background wind, whereas the other, slightly weaker wave moves downwind and shows at both locations upward directed energy propagations. During another Rossby wave breaking event the generation of a secondary wave by non-linear wave-wave interactions has been proved by the bispectral analysis. To investigate the generation and propagation of gravity waves additionally influenced by orographically excited mountain waves over Northern Scandinavia two campaigns were carried out at Andenes (69.2°N , 16.0°E) and Kiruna (67.9°N , 21.9°E). The analyses indicate the presence of a long period horizontal gravity wave with larger wave amplitude on the East-side of the Scandinavian mountain ridge at Kiruna. It has been shown that this gravity wave is generated in the tropopause region in connection with a strong eastward directed jet. Detailed gravity wave analyses based on the mesoscale MM5 model data for the winter MaCWAVE/MIDAS campaign have been used for comparison with results obtained from radar observations. Experimental evidence was found to confirm connections between layering processes in the mesosphere and long period gravity waves. Additionally, a gravity wave climatology confirms the strongest correlation between the daily occurrence rate of multiple PMSE layers and the variances of the meridional winds for periods between 5 – 7 h at an altitude of 86 km in the center of the PMSE layers.

Postal address:
Schloss-Str. 6
18225 Ostseebad Kühlungsborn
Germany

IAP Kühlungsborn
Januar 2006
IAP Nr. 13/2006
ISSN 1615–8083

Contents

1	Introduction	1
1.1	Vertical structure of the atmosphere	2
1.2	The momentum budget	3
1.3	Gravity waves	7
1.4	Thesis overview	8
2	Gravity waves and their characteristics	10
2.1	Wave mechanics	10
2.2	Dispersion and polarization relations	12
2.3	Wave-mean flow interactions	16
2.4	Estimation of gravity wave parameters	19
3	Experimental methods to study gravity waves	22
4	Radar fundamentals	25
4.1	Radio Refractive Index and Radar equation	25
4.2	Beam forming	28
4.3	Radar measurements of wind	28
4.3.1	Doppler techniques	29
4.3.2	Spaced Antenna techniques	31
4.4	Description of the radars	32
4.4.1	OSWIN VHF radar and UHF wind profiler	33
4.4.2	ALOMAR VHF radar ALWIN and Esrange MST radar	34
4.4.3	Comparisons with ECMWF data	34
5	Detection of gravity waves	37
5.1	Bandpass filtering with a Fourier technique	37
5.2	Detection of wave packets by wavelets	38
5.3	Improved bandpass filtering with a Fourier technique	43
5.4	Down- and upward directed ground-based phase propagation	44
5.5	Bispectral analysis	46
6	Methods for investigation of gravity waves	49
6.1	Rotary spectra	50
6.2	Hodograph analysis	50
6.3	Stokes-Parameter spectra	52
6.4	Combined radar and radiosonde measurements	54
6.5	Direct solution of basic equations	55
6.6	Cross-spectral analysis	55

6.7	Gravity waves and Momentum Fluxes	57
7	IGWs observed with collocated radars	60
7.1	Northern Germany: A case study	60
7.1.1	Observations from 17 - 19 December 1999	61
7.1.2	Inertia-gravity wave parameters estimation	63
7.1.3	An example of nonlinear wave-wave interaction in February 2002	78
7.2	Scandinavian mountain ridge: A case study	81
7.2.1	Inertia-gravity wave parameters estimation	81
7.2.2	Comparison with the MM5 model	86
7.2.3	Gravity waves during the MaCWAVE/MIDAS campaign in July 2002	90
8	Long period gravity waves and PMSE	94
8.1	A case study of gravity waves during PMSE	96
8.2	Climatology of gravity waves and multiple PMSE layers	97
9	Summary and Outlook	100
A	Linear gravity wave theory	103
B	Structure of the developed software	107
C	Partial list of symbols and abbreviations	110
	References	115

Chapter 1

Introduction

There are a lot of different forms of motion in the atmosphere and they are governed by the fundamental physical laws of conservation of mass, momentum, and energy. The atmospheric motions are influenced by different kinds of forces, which can be classified as either body forces or surface forces. Body forces act on the center of mass of a fluid parcel and they have magnitudes proportional to the mass of parcel. Gravity force is a good example of a body force. Surface forces act across the boundary surface separating a fluid parcel from its surroundings. Their magnitudes are independent of the mass of the parcel. The pressure force is an example of a surface force.

Most motions in the atmosphere are wavelike motions which result from a balance between inertia and restoring forces acting on fluid parcels displaced from their equilibrium latitudes or altitudes. Due to their primary forces, atmospheric waves occur with different wavelengths and periods; they can be classified into planetary or Rossby waves, atmospheric thermal tides with periods of 12 and 24 h, and gravity waves with periods from about 5 min up to several hours. For a detailed review on the role of waves in the middle atmosphere we refer the reader to *Holton and Alexander* [2000].

This thesis deals with observation and investigation of gravity waves in the atmosphere. Gravity waves are wave motions in a stratified fluid arising from restoring gravity forces acting downwards and buoyancy acting upwards on vertically displaced fluid parcels. For these waves the primary restoring force is provided by the buoyancy force. Propagating to higher altitudes, the gravity wave amplitude generally increases due to the exponential decrease in atmospheric density with height (Figure 1.1), until the waves encounter their breaking level. Here, the amplitude is so large that entailed atmospheric changes become irreversible and the waves deposit energy and momentum into the mean flow.

Due to their ability to redistribute momentum and energy from one region in the atmosphere, the knowledge of gravity waves is therefore essential to understand vertical coupling processes. First investigations of gravity waves have been done in the early works of *Queney* [1948], *Scorer* [1949], *Gossard and Munk* [1954], and *Sawyer* [1959].

The theory to describe these waves has been essentially stimulated by the pioneering work of *Hines* [1960], at first applied to understand irregularities and irregular motions at ionospheric heights. Based on this work, a comprehensive review to understand numerous atmospheric effects is given by *Hines* [1974]. Over the last decades, a multitude of experimental observations, theoretical and modelling studies have considerably improved our understanding of gravity waves and their effects on the atmosphere [*Fritts*, 1984, 1989; *Fritts and Alexander*, 2003].

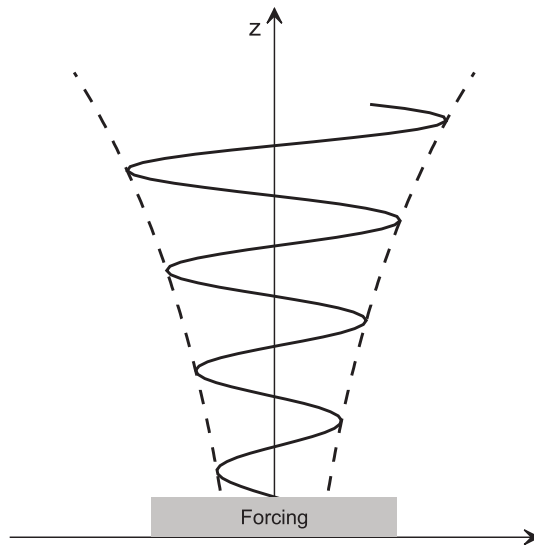


Figure 1.1: Vertical structure of a gravity wave with upward exponentially increasing amplitudes.

To understand the important role of gravity waves for the general circulation, a short introduction follows about the vertical structure of the atmosphere.

1.1 Vertical structure of the atmosphere

The structure of the atmosphere can be considered in different ways, depending on the property of interest. The atmosphere is basically divided in neutral and ionized parts. Below a height of about 100 km, atmospheric motions can be treated as motions of the neutral atmosphere, while motions above ~ 100 km are mainly determined by the ionized plasma. Here we focus on motions in the neutral atmosphere which are closely related to the temperature structure of the Earth's atmosphere. Therefore it is widely accepted to use the vertical structure of the temperature field to divide the Earth atmosphere into different height ranges. Figure 1.2 shows zonal mean temperature profiles for July (solid line) and January (dashed line) from the COSPAR International Reference Atmosphere 1986 (CIRA 86) at a latitude of 50° N.

From the sign of the vertical temperature gradient one can distinguish four regions called troposphere, stratosphere, mesosphere, and thermosphere. The heights between those regions where the temperatures reach local extremes are identified as the tropopause, the stratopause, and the mesopause. In the troposphere, the thermal structure is mainly determined due to heating of CO_2 , H_2O and other "greenhouse gases" by infrared radiation. This radiation results from the heating of the Earth's surface due to solar insolation and reradiation at infrared wavelengths. If the troposphere did not contain these gases, the temperature there would be 20-30 K less. This temperature enhancement is called the "greenhouse effect". The decrease in temperature through the troposphere ceases at the height of approximately 8-12 km.

The stratosphere is characterized by a positive temperature gradient from about 220 K at the tropopause to about 270 K at approximately 50 km where the temperature reaches a local maximum. The reason for the temperature increase with height in the stratosphere is absorption of ultraviolet solar radiation by ozone.

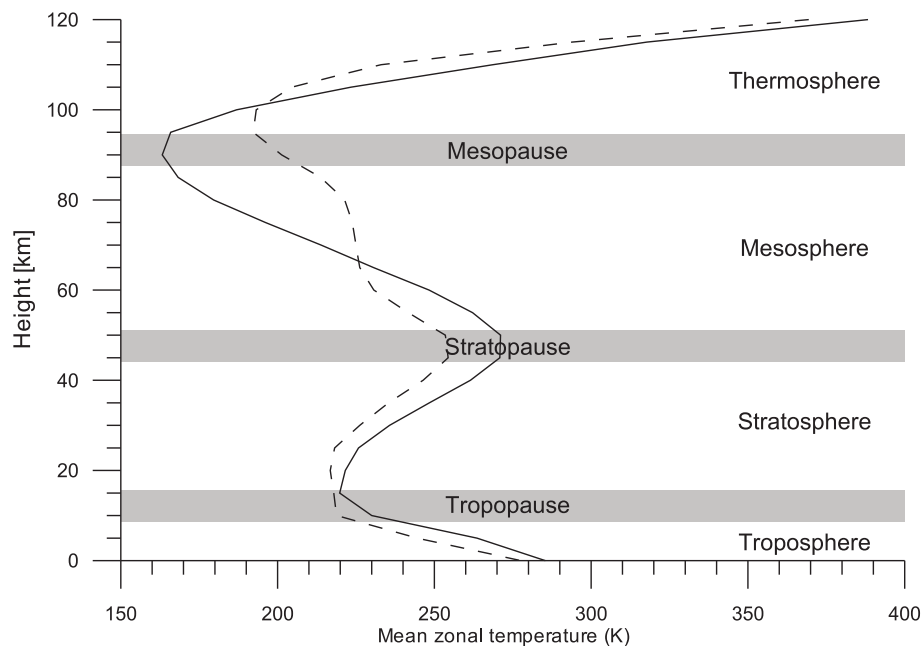


Figure 1.2: Identification of the different regions of the atmosphere using mean zonal temperature profiles for July (solid line) and January (dashed line) from COSPAR International Reference Atmosphere 1986 (CIRA 86) at a latitude of 50° N.

Above the stratopause, the temperature decreases with the height again due to rapidly decreasing ozone concentrations until the temperature reaches its minimum at the mesopause leading to the coldest parts of Earth's atmosphere with temperatures that can fall below 130 K at polar latitudes during the summer months [Lübken, 1999]. Above these heights, in the thermosphere, the temperature once again increases due to photo absorption by various chemical species up to values of about 1000 K depending on the solar activity [Goody and Yung, 1989].

1.2 The momentum budget

The thermal structure of the atmosphere can be understood by the effects of solar irradiation, atmospheric photochemistry, radiative transfer and turbulence, which lead to heating and cooling processes at different heights. The mean state of the atmosphere is described (Figure 1.3) by the contour plots of the zonal mean temperatures and winds of the COSPAR International Reference Atmosphere 1986 (CIRA 86) for January as a function of latitude and height.

As expected, the warmest temperatures on the surface of the earth are found in the tropics. In the stratopause, the temperature maxima occurs at the summer pole due to the maximum solar ozone heating there. At heights of about 90 km, the temperatures reach their minima at high latitudes during summer. The mean zonal wind field shows an eastward jet around the tropopause for both winter and summer. In the mesosphere, the wind direction is eastward in winter and westward in summer, respectively.

However, the temperature and mean zonal wind of the CIRA 86 in Figure 1.3 depart significantly from model results by Geller [1983], shown in Figure 1.4, and based on the radiative equilibrium alone. The presented model calculations of temperatures and the corresponding

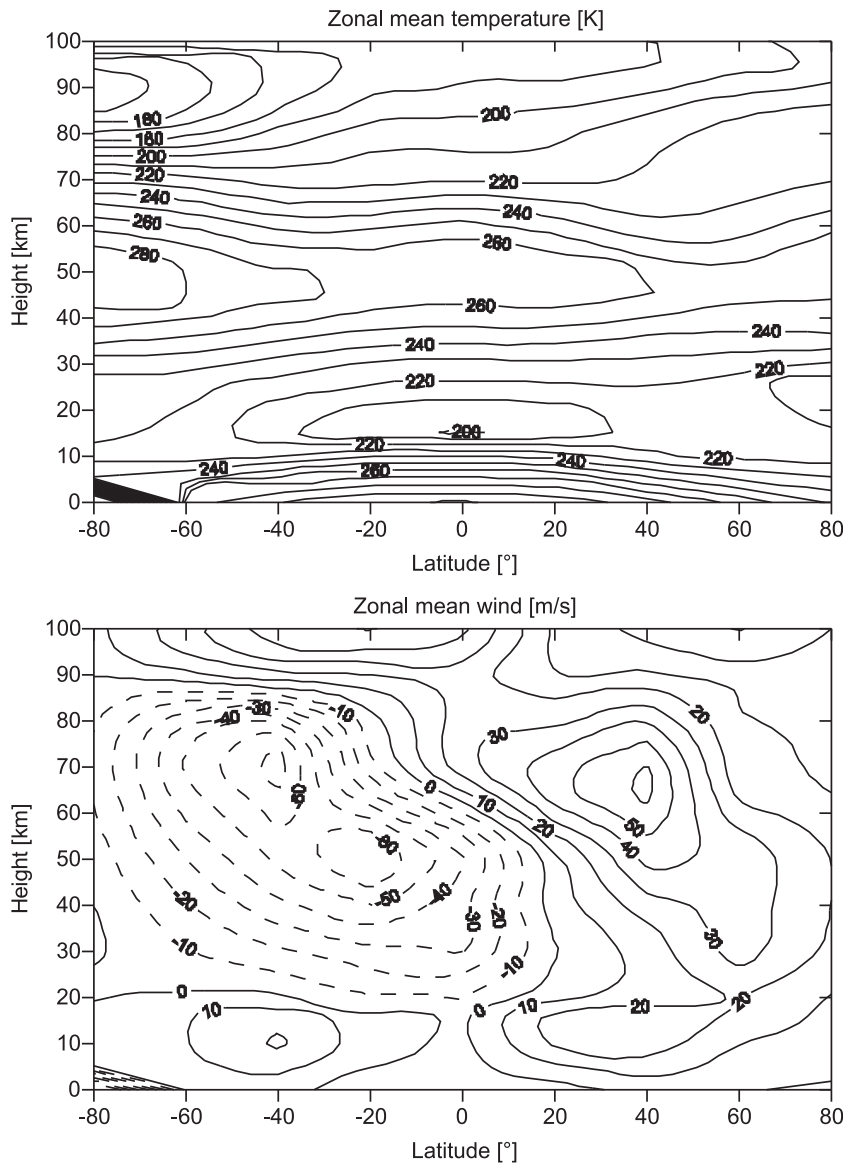


Figure 1.3: Contour plots of zonal mean temperature (top) and zonal mean wind (bottom) of the COSPAR International Reference Atmosphere 1986 (CIRA 86) for January as a function of latitude and height.

geostrophic mean zonal winds, which are given by the balance between the pressure gradient force and the Coriolis force, assume, that the atmosphere is in radiative equilibrium, i.e. the heating due to the absorption of solar radiation and the cooling through infrared reradiation are reflected by the local environment, and no dynamic effects are included. The grey band in the center of the lower panel denotes the region, where the pressure gradient force and the Coriolis force are unbalanced and therefore the horizontal wind cannot be approximated by the geostrophic wind.

Therefore, the temperature gradient in the mesosphere, the local temperature minimum at the tropical tropopause, and the temperature and wind distributions as represented by the CIRA 86 in Figure 1.3 cannot be reproduced by model calculations based on radiative equilibrium conditions.

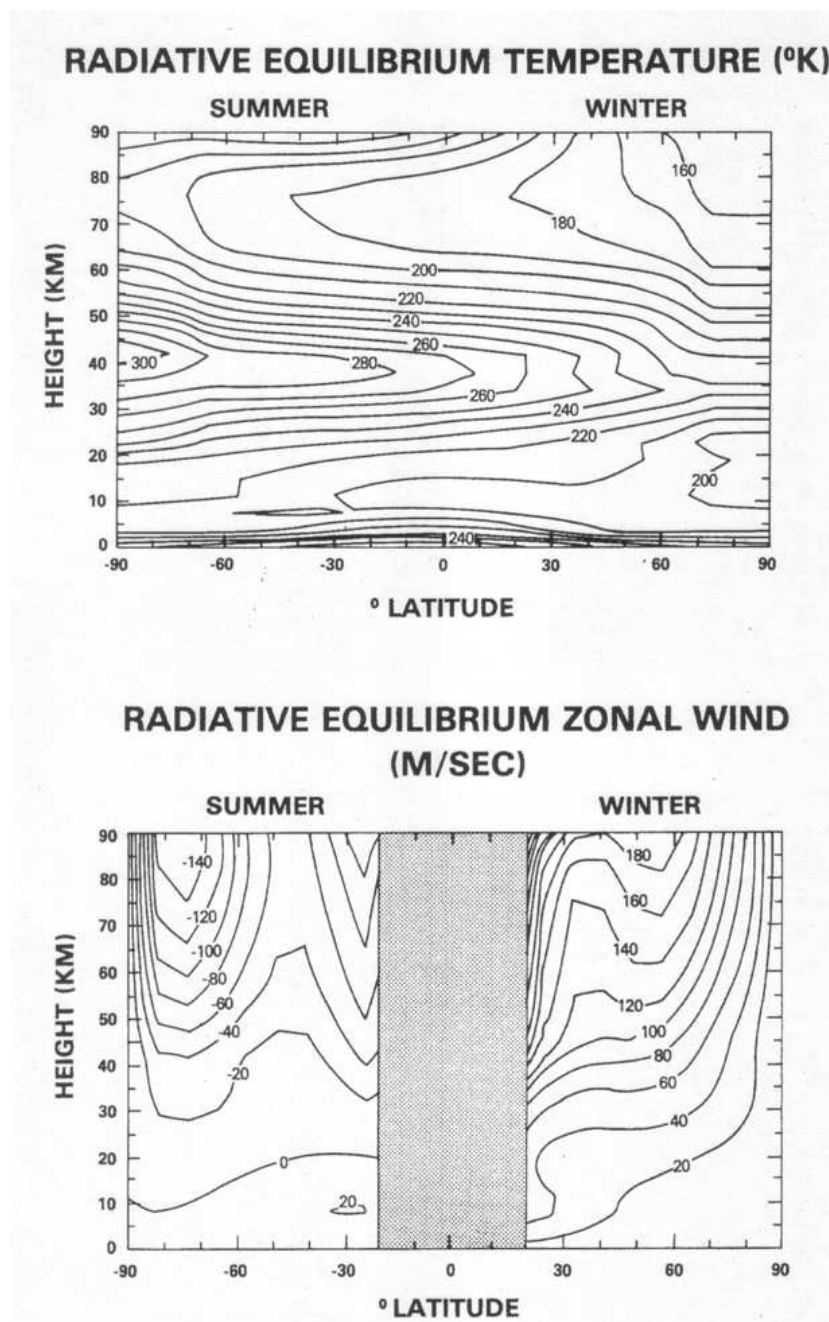


Figure 1.4: Radiative equilibrium temperatures (top) and corresponding geostrophic mean zonal winds (bottom). (After Geller [1983])

To improve the agreement between model and observations, Leovy [1964], Schoeberl and Strobel [1978], Holton and Wehrbein [1980] proposed a zonal momentum dissipation mechanism, a so-called Rayleigh drag. This mechanism decelerates the mean zonal wind speed linearly and closes the jet stream. Application of the Rayleigh drag leads to a better agreement in temperature and zonal wind distributions between observations and model results [Geller, 1983]. However for equilibrium conditions, an additional force is required to counterbalance the Rayleigh drag. In existence of a mean meridional motion from the summer pole to the winter pole this can be provided by the Coriolis effect. Mass continuity then requires an

upward motion at the summer pole and a compensating downward motion at the winter pole as shown in Figure 1.5 [Dunkerton, 1978]. The circulation also leads to a rising motions at the tropical tropopause and falling motions across the extratropical tropopause. Therefore, the deviations of the temperature from the radiative equilibrium are explained by the vertical motions near the poles, and the associated expansion cooling and compression heating of the air parcels as they rise and fall over summer and winter pole, respectively [Geller, 1983].

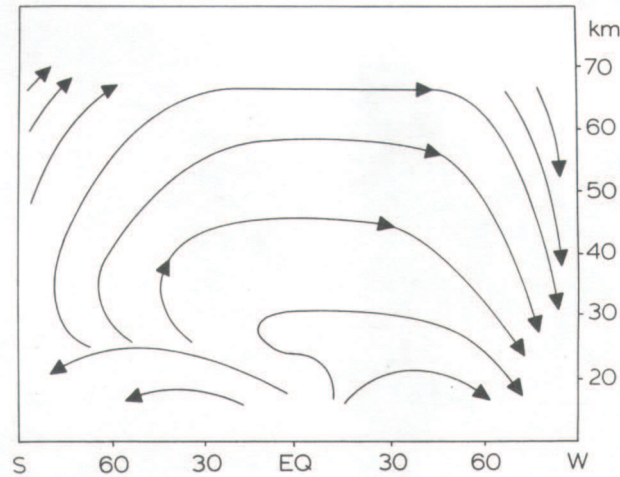


Figure 1.5: Global meridional circulation in the middle atmosphere. (After Dunkerton [1978])

But the Rayleigh drag was still a convenient parameterization that had no physical explanation. Houghton [1978] proposed, that various types of waves could take part to balance the mesospheric momentum budget. He concluded that gravity waves are the most likely type of waves responsible for this process. Hence, accurate parameterizations of gravity wave effects in the model simulations are required.

Several schemes to parameterize the influence of gravity waves have been developed and applied in general circulation models (GCMs) [Lindzen, 1981; Fritts and VanZandt, 1993; Hines, 1997; Warner and McIntyre, 1999]. However, due to the small spatial scales, gravity waves cannot be explicitly resolved in these models, and a number of fundamental scientific problems remain.

For example, one needs more quantitative information about the degree of gravity wave intermittency in the real atmosphere for implementation in parametrization schemes. Another problem is the current absence of detailed observations to characterize the wave spectrum and its behavior with altitude. First steps to improve the information about global climatology of gravity waves have been initiated by Allen and Vincent [1995] in the frame of the SPARC campaign [e.g. Schöllhammer, 2002; Wang et al., 2005]. More detailed observations and comparisons with modelling studies are required to address the geographic and seasonal variability of gravity waves and relative importance of different source mechanisms. Precise descriptions of sources, propagation, wave-wave interactions, mixing and climatologies will help to describe the gravity waves in large-scale models more adequately [Fritts and Alexander, 2003].

1.3 Gravity waves

To understand the general structure and dynamics of the atmosphere and its variability, it is important to know the coupling between different atmospheric regions from the troposphere up to the thermosphere. Often changes caused by solar or non-solar sources are observed at heights which may be different from the origin of this effect. Important coupling processes are radiative exchanges, transport of chemically active minor constituents and dynamical processes. The dynamical coupling mainly includes the forcing of different atmospheric waves (gravity waves, tides, planetary waves), their propagation through the atmosphere, the interaction between different waves and their impact upon the mean circulation.

Today it is recognized that gravity waves are an essential part of the dynamics of the atmosphere on all meteorological scales. On the largest atmospheric scale, studies, for example, by *Lindzen* [1981] and *Holton* [1982], examined the effects of gravity waves on the upper atmosphere and the general circulation. On the mesoscale, *Uccellini* [1975], *Stobie et al.* [1983], *Uccellini and Koch* [1987], and *Chimonas and Nappo* [1987] investigated the interactions between gravity waves and thunderstorms. *Lilly and Kennedy* [1973], *Clark and Peltier* [1977], and *Smith* [1979] demonstrated the generation of gravity waves by mountains. On the microscale, studies by *Chimonas* [1972], *Einaudi and Finnigan* [1981], and *Fua et al.* [1982] proved the interactions between gravity waves and turbulence in the stable planetary boundary layer.

Hines [1988], *Chimonas and Nappo* [1989], and *Nappo and Chimonas* [1992] showed the interactions of gravity waves generated by small-scale terrain features with the mean boundary-layer flow to produce turbulence in the upper regions of the stable planetary boundary layer. Recently, *Pavelin and Whiteway* [2002] investigated stratospheric VHF radar data for an impressive experimental study of turbulence generated by the interaction of different types of gravity waves.

Particularly in the lower stratosphere, transport and mixing processes due to inertia-gravity waves (IGW) with frequencies close to the Coriolis frequency f_c are expected to be important, as shown by *Plougonven et al.* [2003]. These waves can alter the mean stratospheric temperature locally with amplitudes up to 10 K, which supports for instance at polar latitudes the generation of Polar Stratospheric Clouds during the winter months as investigated by *Dörnbrack et al.* [2002] and *Buss et al.* [2004].

Gravity waves are observed in various regions of the Earth. The most important property of these waves is their ability to transport energy away from their sources. The main sources for gravity waves are:

- orographic forcing [*Smith*, 1979, 1989; *Queney*, 1948; *Röttger*, 2000],
- jet streams in the tropopause region, e.g. ageostrophic adjustment or secondary wave emission from wave breaking regions [*O'Sullivan and Dunkerton*, 1995; *Plougonven et al.*, 2003; *Zülicke and Peters*, 2004],
- deep convection processes [*Nastrom et al.*, 1990; *Clark and Kuettner*, 1986; *Alexander and Holton*, 2004; *Böhme et al.*, 2004],
- wave-wave interactions [*Rüster*, 1994b],
- frontal activity [*Schöllhammer*, 2002],
- thunderstorms [*Chimonas and Nappo*, 1987; *Finke*, 1995].

The propagation of gravity waves is mainly controlled by the atmospheric wind field. For the normal case of tropospheric sources, the gravity wave spectrum in the mesopause region depends markedly on the filtering effect of the wind field in the strato- and mesosphere [Lindzen, 1981; Holton, 1982; McLandress, 1998] due to reflection and absorption of gravity waves at critical levels. Therefore, the observed gravity wave signatures observed in the mesosphere/lower thermosphere (MLT) region contain information about their sources and also about the wind field between the source and the observing region. The energy and momentum transfer from the gravity waves into the circulation of the MLT region is closely connected with the gravity wave breaking and the creation of turbulence. A comprehensive overview about gravity wave saturation and breaking can be found in *Fritts* [1984] and *Fritts and Alexander* [2003]. In spite of many different investigations during the last years, there remain a lot of open questions about

- the generation and propagation of gravity waves from their sources,
- the temporal and spatial properties of gravity waves,
- the modulation and interaction of gravity waves with other atmospheric waves (tides and planetary waves),
- the processes connected with the transition from gravity waves to turbulence in the upper regions of the atmosphere.

Atmospheric radars are widely used to find answers to the aforementioned unsolved questions. Detailed investigations of gravity waves based on measurements with single radars have been done e.g. by [Sato, 1994; Thomas *et al.*, 1999; Cho, 1995; Kuo *et al.*, 2003]. Inspired by *Ecklund et al.* [1985] and *Carter et al.* [1989], the usage of collocated radars will improve the statistical reliability of the results as well as the knowledge on mesoscale gravity waves as recently shown by *Trexler and Koch* [2000], using the NOAA wind profiler network data. In Germany, similar improved technical conditions are available since January 2004 with the new operational UHF wind profiler network of the Deutscher Wetterdienst [Lehmann *et al.*, 2003].

The evaluation of continuously running modern radar experiments with new methods will considerably contribute to the investigation of gravity waves.

1.4 Thesis overview

Most of the work presented here was carried out under the LEWIZ project (**L**etzter **W**inter im **Z**wanzigsten Jahrhundert) [Peters *et al.*, 2003, 2004]. As shown by *O'Sullivan and Dunkerton* [1995], inertia-gravity waves with a relatively long horizontal wavelength can be generated during Rossby wave breaking events. They propagate under certain conditions both horizontally and vertically, and can play a significant role in exchange processes of the upper troposphere and lower stratosphere. Therefore the main objective of this project was to investigate in a region with no large orography (Mecklenburg-Vorpommern, Northern Germany), via case studies, the appearance of strong IGWs, their generation and properties in connection with Rossby wave breaking events.

The other studies of gravity waves were carried out under the MaCWAVE/MIDAS-project. The main aim of the MaCWAVE/MIDAS campaigns was to investigate waves produced by the Scandinavian mountain ridge, to track these waves using different instruments such as

radar/rocket/lidar/radiosondes data from troposphere up to the mesosphere, and attempt to detect energy dissipation in that region produced by wave breaking.

The main aims of this work are in particular:

- determine the properties of inertia-gravity waves using continuous collocated VHF radar measurements at different locations in the frame of different campaigns;
- application of wavelets to consider the height and time dependence of gravity waves;
- to apply methods developed in the frame of these projects to investigate inertia-gravity waves and their sources in the upper troposphere and lower stratosphere generated by jet streams:
 - in a region without large orography at Kühlungsborn and Lindenberg;
 - to investigate inertia-gravity waves in a region with additional influence of orographically induced mountain waves using the radar data from two sites (Andenes and Kiruna) in front of and behind the Scandinavian mountain ridge;
- extension and application of the developed methods to study the influence of long period gravity waves on Polar Mesosphere Summer Echoes (PMSE).

The thesis is organized as follows.

In Chapter 2 an introduction is given to basic gravity wave characteristics based on the linear theory for a better understanding of the other part of this work. The detailed derivation of the relations to describe the connection between the main gravity wave characteristics is shown in Appendix A.

Different experimental techniques for the investigation of gravity waves are listed and compared in Chapter 3. The fundamentals of atmospheric radars are presented in Chapter 4.

In Chapter 5 various algorithms are introduced and discussed for the detection and extraction of gravity wave packets. A description and comparison of developed and applied methods for the investigation of gravity waves is given in Chapter 6. For the application of these methods, the structure of the developed software is presented in Appendix B.

Chapter 7 deals with the analysis of data obtained with collocated radar measurements during several campaigns carried out in Northern Germany and Northern Scandinavia. Chapter 8 is devoted to the role and characteristics of long period gravity waves in connection to the structure of Polar Mesosphere Summer Echoes.

Finally, a thesis summary with suggestions for future research is provided in Chapter 9.

Chapter 2

Gravity waves and their characteristics

In the previous chapter the importance of gravity waves in the atmosphere and requirements for their measurements have been discussed. The interpretation of observations needs deep knowledge about gravity wave motions and the propagation of waves through the atmosphere. In this chapter we will reproduce some principles of the wave mechanics and discuss the main characteristics of gravity waves. The dependencies between different wave characteristics are based on linearized solutions of fluid-dynamical equations (see Appendix A). More details on gravity wave theory can be found in the textbooks of *Gossard and Hooke* [1975], *Gill* [1982], *Holton* [1992], and *Nappo* [2002]. Finally, an outline is given for the estimation of characteristic parameters for long period gravity waves and their related momentum fluxes.

2.1 Wave mechanics

In this section, we define some space and time characteristics needed to describe the waves. A monochromatic wave is described by

$$\psi(x, y, z, t) = a_0 \cdot \exp(i(kx + ly + mz - \omega t)), \quad (2.1)$$

where ψ can be perturbations with amplitude a_0 of zonal u' or meridional v' winds, temperature T' or pressure p' with a time t . The zonal, meridional and vertical wavenumbers are denoted by k , l and m in x -, y -, z -directions, respectively, $i = \sqrt{-1}$, and ω is the wave frequency, observed at a fixed location.

The lines of constant phase ϕ determine the spatial orientation of the wave fronts:

$$\phi = kx + ly + mz - \omega t. \quad (2.2)$$

With $k = 2\pi/L_x$, $l = 2\pi/L_y$ and $m = 2\pi/L_z$, the length L of the wave is given by

$$\left(\frac{1}{L}\right)^2 = \left(\frac{1}{L_x}\right)^2 + \left(\frac{1}{L_y}\right)^2 + \left(\frac{1}{L_z}\right)^2, \quad (2.3)$$

where L_x , L_y and L_z are wavelengths in zonal, meridional, and vertical direction, respectively (Figure 2.1).

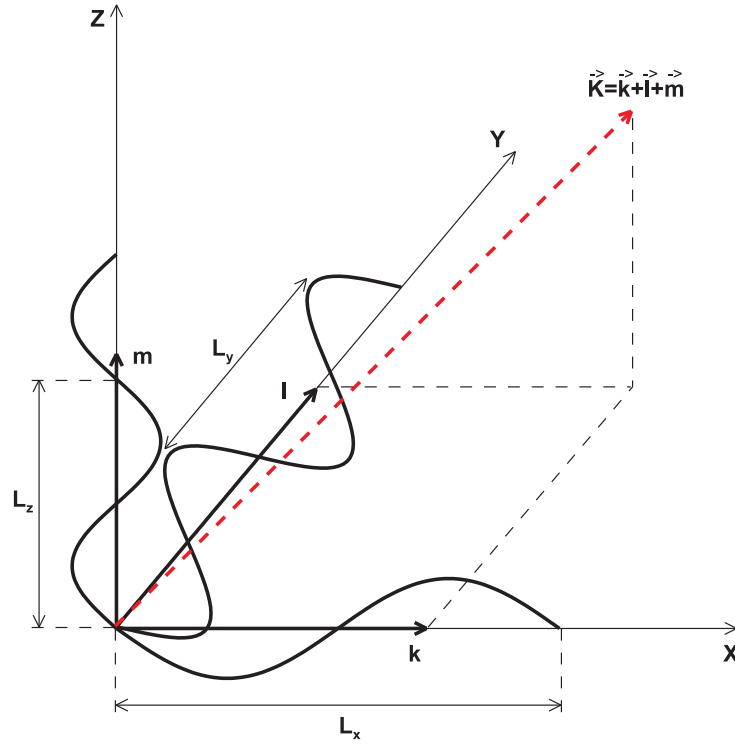


Figure 2.1: Schematic representation of spatially propagating wave.

The wave speed determined by the phase velocity v_p is the speed at which a point of constant phase moves in the direction of the wave propagation. Using the magnitude of the wave vector \vec{K}

$$|\vec{K}|^2 = k^2 + l^2 + m^2, \quad (2.4)$$

then the phase velocity is given by

$$v_p = \frac{\omega}{|\vec{K}|}. \quad (2.5)$$

The speed of the waves along the x-, y-, and z-axes is then given by

$$(v_{px}, v_{py}, v_{pz}) = \left(\frac{\omega}{k}, \frac{\omega}{l}, \frac{\omega}{m} \right). \quad (2.6)$$

There are two classes of waves: dispersive and nondispersive. The types of waves, whose phase velocities are independent from wavenumbers, are called nondispersive waves. In such waves, a spatially localized disturbance consisting of a number of Fourier wave components (a wave group) will preserve its shape as it propagates in space with the phase velocity of the wave. The waves in which phase velocity varies with wavenumber are denoted as dispersive waves, and the formula that relates wave frequency ω and wavenumber K is called a dispersion relationship, discussed in Section 2.2. For dispersive waves, however, the speed of the wave group is generally different from the average phase speed of individual components. Hence, individual wave components (and hence the energy) may move through the wave group with a group velocity c_g as the group propagates along. The group velocity in zonal, meridional and vertical directions is defined as

$$(c_{gx}, c_{gy}, c_{gz}) = \left(\frac{\partial \omega}{\partial k}, \frac{\partial \omega}{\partial l}, \frac{\partial \omega}{\partial z} \right) \quad (2.7)$$

In Figure 2.2 a wave profile is shown at different times. The bold line connects node points of the waves and corresponds to the phase velocity, and the dashed line connects crests of the envelope, which is travelling through the wave, and corresponds to the group velocity.

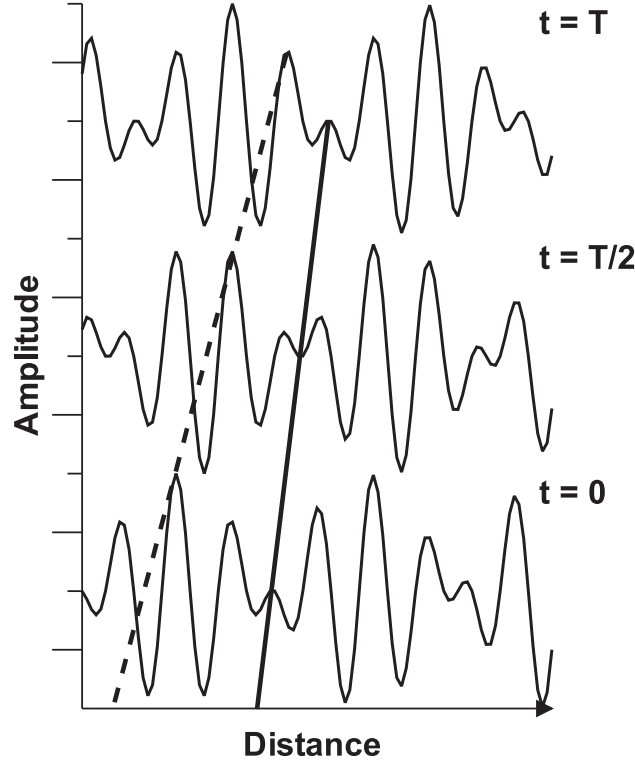


Figure 2.2: A modulated carrier wave. The bold line connects node points of the waves and the dashed line connects crests of the envelope.

From the line slopes it is clear that carrier waves are moving faster than the packet, it means that the group velocity differs from the phase velocity in all cases except the case when wave frequency depends linearly on their wavenumber ($\omega = const * K$).

2.2 Dispersion and polarization relations

Wave motions in the atmosphere are the result of parcel oscillation from equilibrium point under the influence of inertia and restoring forces. For gravity waves, the primary restoring forces are provided by the fluid buoyancy. Atmospheric gravity waves can exist only when the atmosphere is stably stratified so that a fluid parcel displaced vertically will undergo adiabatic oscillations from its equilibrium level. In these waves, parcels oscillate parallel to phase lines and perpendicular to the direction of phase propagation.

Almost all theoretical studies of gravity waves have been done under simplifications of linear theory. The linear theory provides dependencies between different wave characteristics under linearized solutions of fluid-dynamical equations. Details of this theory are given in Appendix A. From the solution of these equations, the common dispersion relation can be derived

$$\hat{\omega}^2 = \frac{N^2 (k^2 + l^2) + f_c^2 \left(m^2 + \frac{1}{4H_p^2} \right)}{k^2 + l^2 + m^2 + \frac{1}{4H_p^2}}. \quad (2.8)$$

This equation describes the relation between the intrinsic frequency of the wave $\hat{\omega}$, horizontal and vertical wavenumbers (k, l, m) and the corresponding Brunt-Väisälä frequency N , Coriolis parameter f_c , density scale height H_p .

The intrinsic frequency, i.e. the frequency in a coordinate system moving with the fluid, differs from the observed frequency which is relative to the fixed position at the ground. The relation connecting both frequencies is known as Doppler relation:

$$\omega_{ob} = \hat{\omega} + \bar{u}k_h, \quad (2.9)$$

where ω_{ob} is the observed frequency and \bar{u} is the mean background horizontal wind component in the same direction as the horizontal wavenumber $k_h = \sqrt{k^2 + l^2}$.

Furthermore, the resulting wind and normalized temperature perturbations (u', v', w', \hat{T}') are interrelated by the polarization relations:

$$\begin{aligned} v' &= \frac{l\hat{\omega} - ikf_c}{k\hat{\omega} + ilf_c} u' \\ w' &= -\frac{\hat{\omega}m}{\hat{\omega}k + if_cl} \frac{\hat{\omega}^2 - f_c^2}{N^2 - \hat{\omega}^2} u' \\ \hat{T}' &= \frac{T'}{T_0} = -i \frac{N^2}{g\hat{\omega}w'} = i \frac{N^2 (k^2 + l^2)}{mg} \frac{1}{\hat{\omega}k + if_cl} u', \end{aligned} \quad (2.10)$$

where g is acceleration of gravity, T_0 and T' are background temperature and temperature perturbations, respectively.

The dispersion relation (Equation 2.8) admits waves with different frequencies and broad range of properties. For vertically propagating gravity waves, k , l and m are real, and the intrinsic frequency must lie in the range $N > \hat{\omega} > |f_c|$. All parts of this spectrum can contribute to atmosphere dynamics. The model analysis describing the gravity wave propagation across a wide range may need to retain all terms in Equation 2.8. However, some simpler forms representing waves in certain limited regions of the spectral space provide considerable insight [Fritts and Alexander, 2003].

Considering the case of **high-frequency gravity waves** with intrinsic frequency $\hat{\omega}$ much larger than Coriolis frequency f_c and for which $m^2 \gg 1/4H_p^2$, we can neglect the Coriolis frequency. Then the dispersion relation simplifies to

$$\hat{\omega}^2 = \frac{N^2(k^2 + l^2)}{k^2 + l^2 + m^2} = N^2 \cos^2 \chi, \quad (2.11)$$

where χ is the angle between lines of constant phase and the vertical direction. The group velocity simplifies to

$$(c_{gh}, c_{gz}) = (\bar{u}_h, 0) + \frac{Nm}{k_h^2 + m^2} \frac{(m, -k_h)}{(k_h^2 + m^2)^{1/2}}, \quad (2.12)$$

where c_{gh} and c_{gz} are the horizontal and vertical components of group velocity, respectively. Gravity waves with high intrinsic frequency are observed in mesopause airglow image data [Swenson and Espy, 1995; Taylor and Garcia, 1995], also with VHF radar data [Reid et al., 1988; Fritts et al., 1990; Böhme et al., 2004].

The physical mechanism for the propagation of high-frequency gravity waves can be understood by considering a simple case with a fluid parcel, which is displaced by a distance δs along a line tilted with an angle χ as shown in the Figure 2.3. For simplicity, the two-dimensional case is discussed.

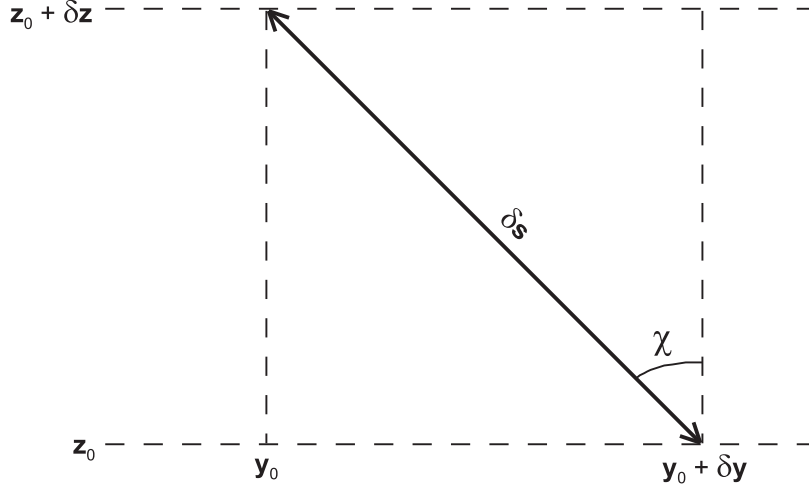


Figure 2.3: Parcel oscillation path in meridional plane for an inertia-gravity wave.

For a vertical displacement δz the buoyancy force component parallel to the slope of the parcel oscillation is $-N^2 \delta z \cos \chi$. With regard to $\delta z = \delta s \cos \chi$ the momentum equation for the parcel oscillation is

$$\frac{D^2 \delta s}{Dt^2} = -(N \cos \chi)^2 \delta s \quad (2.13)$$

where δs is the perturbation parcel displacement.

The momentum equation 2.13 has the general solution $\delta s = \exp[\pm i(N \cos \chi)t]$. Therefore, the parcel execute a harmonic oscillation at the frequency $\hat{\omega} = N \cos \chi$.

For **midrange gravity waves** with intrinsic frequencies in the range $N \gg \hat{\omega} \gg f_c$, the dispersion relationship simplifies to

$$\hat{\omega} = N \left| \frac{k_h}{m} \right|, \quad (2.14)$$

and the connection between vertical wavenumber m and intrinsic horizontal phase velocity \hat{v}_h can be written as

$$|m| = \frac{N}{|\hat{v}_h|}. \quad (2.15)$$

The group velocities for medium-frequency gravity waves are

$$(c_{gh}, c_{gz}) = (\bar{u}_h, 0) + N \left(\frac{1}{m}, -\frac{k_h}{m^2} \right) = (\bar{u}_h, 0) + \left(\frac{\hat{\omega}}{k_h}, \frac{-\hat{\omega}}{m} \right) \quad (2.16)$$

and have the same magnitude as the phase propagations but opposite signs in the vertical direction.

Main parts of this work are related to **gravity waves with low frequencies**. For these waves the rotation of the Earth has an important influence. As already mentioned in Section 1 these waves are also called inertia-gravity waves.

These kinds of gravity waves are commonly seen in the upper troposphere and lower stratosphere observations [Vincent and Alexander, 2000; Eckermann et al., 1995; Rapp et al., 2002]. When the Coriolis force is included in the linearized equations, then the dispersion relationship becomes approximately

$$\hat{\omega}^2 = f_c^2 + N^2 \frac{k^2 + l^2}{m^2} = N^2 \frac{k_h^2}{m^2} + f_c^2. \quad (2.17)$$

The wave group velocity in this case is given by

$$(c_{gh}, c_{gz}) = (\bar{u}_h, 0) + \frac{N^2 k_h}{\hat{\omega} m^2} \left(1, -\frac{k_h}{m} \right). \quad (2.18)$$

Parcel displacements in a case of low-frequency gravity waves are resisted by both rotation and buoyancy. Following the idea of parcel oscillation (Figure 2.3), the Coriolis force has to be added into the momentum equation 2.13. For meridional displacement δy the Coriolis (inertial) force component parallel to the slope of the parcel path is $-f_c^2 \delta y \sin \chi$. Substituting $\delta y = \delta s \sin \chi$, the momentum equation 2.13 for the parcel oscillation modifies to

$$\frac{D^2 \delta s}{Dt^2} = -(f_c \sin \chi)^2 \delta s - (N \cos \chi)^2 \delta s \quad (2.19)$$

The frequency now satisfies the dispersion relationship

$$\hat{\omega}^2 = N^2 \cos^2 \chi + f_c^2 \sin^2 \chi. \quad (2.20)$$

If gravity waves meet the condition $(k^2 + l^2)/m^2 \ll 1$, then the approximate dispersion relationship (Equation 2.17) is a particular case of Equation 2.20 when we let

$$\begin{aligned} \sin^2 \chi &\rightarrow 1 \\ \cos^2 \chi &= (k^2 + l^2)/m^2. \end{aligned}$$

By combination of the dispersion relation (Equation 2.17) and Doppler relation (Equation 2.9), the dependence of intrinsic and observed periods from horizontal and vertical wavelengths of the low-frequency gravity wave is plotted in Figure 2.4. The Coriolis parameter over Kühlungsborn ($54^\circ N$) is equal to $11.8 \cdot 10^{-5} \text{ s}^{-1}$ (Equation 2.26), the Brunt-Väisälä frequency in the troposphere can be approximated by a value of 0.013 s^{-1} . If we assume a mean horizontal wind 20 m/s, then the intrinsic period (Figure 2.4, left panel) and observed period (Figure 2.4, right panel) for corresponding horizontal and vertical wavelengths can be

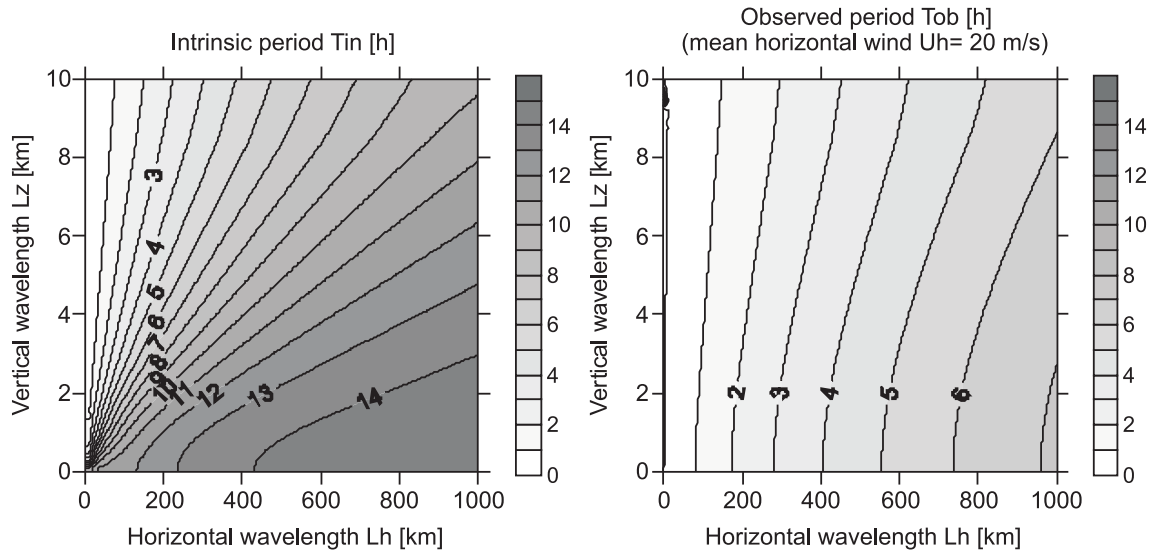


Figure 2.4: Dependence of intrinsic (left panel) and observed (right panel) periods from horizontal and vertical wavelengths of a gravity wave in the troposphere over Kühlungsborn (54°N) based on the linear theory (Equations 2.17 and 2.9) with a mean horizontal wind $U_h = 20$ m/s in direction of wave propagation, Coriolis frequency $f_c = 11.8 \cdot 10^{-5} \text{ s}^{-1}$, and Brunt-Väisälä frequency $N = 0.013 \text{ s}^{-1}$.

derived. As shown in Figure 2.4, the Doppler shift of the intrinsic period by a wind of 20 m/s leads to smaller values of the observed period.

A characteristic of gravity waves is that phase fronts and energy move in opposite direction vertically, while the intrinsic phase ($\hat{v}_{pz} = \hat{\omega}/m$) and group ($\hat{c}_{gz} = \partial\hat{\omega}/\partial m$) velocities have opposite signs. The horizontal propagation direction of phase fronts and energy are both in the direction of the horizontal component of k .

The dispersion relations (Equations 2.8, 2.11, 2.14, and 2.17) have an uncertainty in the sign of the vertical wavenumber m , which determines via the vertical group velocity c_{gz} the energy propagation, therefore we cannot assign a priory m to a positive or negative value. To illustrate how the appropriate wavenumbers are selected, upward and downward propagating waves are demonstrated in Figure 2.5.

Consider the case of upward energy propagation, where group velocities c_{gx} and c_{gz} are both positive, and wave speed greater than background wind $v_{px} > u_o$ (Figure 2.5b). Since zonal wavenumber k is positive, we see from Equation 2.18 that the vertical wavenumber has to be negative ($m < 0$). If wave speed is less than background wind $v_{px} < u_0$ (Figure 2.5a), then we must choose a vertical wavenumber $m > 0$ if vertical group velocity c_{gz} is positive. Consider now the case where $c_{gx} > 0$ and $c_{gz} < 0$ (Figure 2.5d), i.e., downward propagating energy. Now we must take $m > 0$ when $v_{px} > 0$ and $m < 0$ when $v_{px} < 0$.

2.3 Wave-mean flow interactions

The equations governing the dynamics of the atmosphere require a balance of quantities such as momentum, heat flux and mass flux. If the atmospheric density is ρ , the quantity $\rho u'$ is the horizontal momentum per unit volume. Under the influence of a vertical velocity w' , the amount of some quantity crossing an area A in unit time is $w'A$. Combining these concepts, it

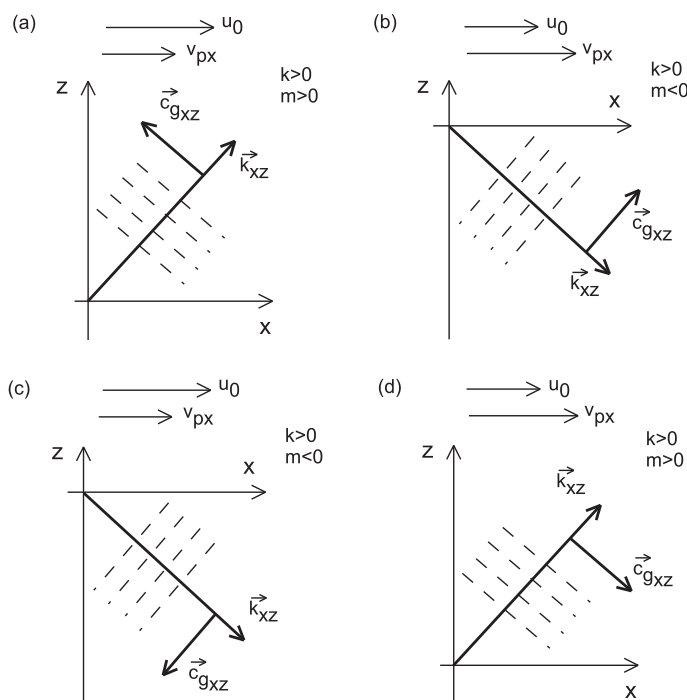


Figure 2.5: Wave vectors and group velocity vectors for (a) upward propagating energy and wave speed less than background wind speed; (b) upward propagating energy and wave speed greater than background wind speed; (c) same as (a) but with downward propagating energy; and (d) same as (b) but with downward propagating energy.

becomes clear that $\rho u'w'$ is the amount of zonal momentum per volume unit crossing an area in a definite time. This quantity has been called the vertical flux density of zonal momentum. In a similar manner, $\rho v'w'$ is defined as the vertical flux density of meridional momentum. The significance of these quantities lies in its variation with height. If the momentum passing through one level is different to those in other levels, a force must exist to account for this difference.

From the physical point of view, when a gravity wave propagates through the background atmosphere, air parcels are accelerated and displaced. Yet, when averaged over cycle, the net momentum flux of wave-induced particle motions is zero, and the displaced air parcels are returned to their equilibrium position as long as the processes are reversible. However, when material contours are deformed irreversibly, for example by wave breaking, then the momentum is transferred to the mean flow. Gravity waves are the most likely process of transporting momentum from the energy-dense troposphere into the mesosphere.

Mathematically, this momentum transfer can be described by the generalized Eliassen-Palm flux \vec{F} [Eliassen and Palm, 1961; Andrews and McIntyre, 1976, 1978]. Eliassen and Palm [1961] showed that for steady linear waves in a zonal flow, which was a function of latitude and height only, with no frictional or diabatic effects, the divergence of the Eliassen-Palm flux is zero (generalized Eliassen-Palm theorem):

$$\nabla \cdot \vec{F} \equiv 0. \quad (2.21)$$

In the case of gravity waves, the Eliassen-Palm flux takes a form $\vec{F} = (0, -\rho_0 \overline{u'w'}, -\rho_0 \overline{v'w'})$. Therefore, the resulting gravity wave induced mean-flow acceleration is zero

$$\begin{aligned}\frac{1}{\rho_0} \frac{\partial}{\partial z} (\rho_0 \overline{u'w'}) &= 0 \\ \frac{1}{\rho_0} \frac{\partial}{\partial z} (\rho_0 \overline{v'w'}) &= 0.\end{aligned}$$

According to the theorem, steady linear waves do not interact with the mean flow. Otherwise, when waves become dissipative, they will produce wave accelerations of the mean flow $-\rho_0^{-1} \partial(\rho_0 \overline{u'w'})/\partial z$ and $-\rho_0^{-1} \partial(\rho_0 \overline{v'w'})/\partial z$ in zonal and meridional directions, respectively.

The methods to obtain $\overline{u'w'}$ and $\overline{v'w'}$ with a radar technique are discussed in Section 6.7 and applied in Section 7.1.2. The measured quantity in the momentum flux analysis is considered in the following simple example as an introduction to the analysis method.

To get more insight into the behavior of the momentum fluxes we will apply a simulation for a direct estimation of these quantities. First we simulated zonal, meridional and vertical wind perturbations using Equation 2.17 and simple solutions of fluid-dynamical Equations A.7-A.11 [Holton, 1992]:

$$(u', v', w', p'/\rho_0) = \text{Re} [(\hat{u}, \hat{v}, \hat{w}, \hat{p}) \exp i(kx + ly + mz - \hat{\omega}t)], \quad (2.22)$$

where

$$\begin{aligned}\hat{u} &= (\hat{\omega}^2 - f_c^2)^{-1} (\hat{\omega}k + ilf_c) \hat{p} \\ \hat{v} &= (\hat{\omega}^2 - f_c^2)^{-1} (\hat{\omega}l - ikf_c) \hat{p} \\ \hat{w} &= -\frac{\hat{\omega}m}{N^2} \hat{p}\end{aligned} \quad (2.23)$$

The parameters used for the simulation of a gravity wave are shown in the Table 2.1.

IGW parameters	$z < h_{Tr}$	$z \geq h_{Tr}$
Zonal wavelength, $2\pi/k$, km	-890	-890
Meridional wavelength, $2\pi/l$, km	10000	10000
Vertical wavelength, $2\pi/m$, km	3.3	-2.0
Pressure amplitude, \hat{p} , hPa	0.5	
Tropopause height, h_{Tr} , km	8.5	

Table 2.1: List of the parameters used for the simulation of gravity waves in the upper troposphere and lower stratosphere.

In this simulation we create a downward directed energy propagation at heights below 8.5 km by using a positive vertical wavenumber $m = \frac{2\pi}{L_z}$, whereas at heights above 8.5 km, where the vertical wavenumber is negative, the energy propagates upward. Such a situation can be observed in the presence of a jet stream caused by breaking Rossby waves, as discussed in Peters *et al.* [2003]. The induced wind perturbations are shown in Figure 2.6. The vertical fluxes, flux densities and mean-flow accelerations of the zonal (Figure 2.7 upper part) and meridional (Figure 2.7 lower part) momenta have been estimated by averaging of wind perturbations with time and derivation with a height.

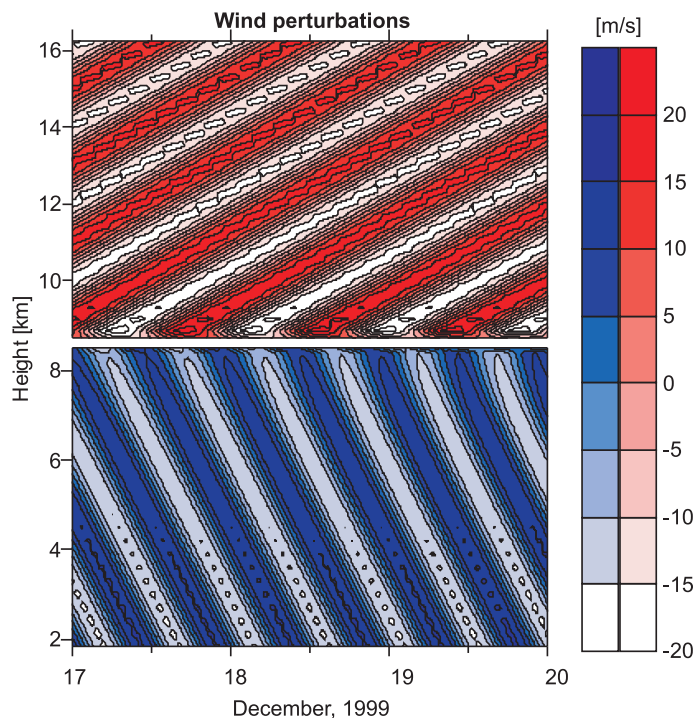


Figure 2.6: Wind perturbations of the simulated gravity wave.

With these simulations, the zonal flux shows larger amplitudes in comparison to the meridional flux confirming a zonal propagation of the simulated gravity wave. Also the sign of the zonal vertical flux of horizontal momentum has a positive value in the troposphere and a negative value in the lower stratosphere. The mean-flow acceleration is close to zero and shows two opposite peaks at the height, where the flux changes its sign. We used these simulations to understand the results obtained with real data, as later shown in Section 7.1.2.

2.4 Estimation of gravity wave parameters

The main representative characteristics of gravity waves are their intrinsic frequency, horizontal and vertical wavenumbers and phase and group velocities. For investigation of inertia-gravity waves we will define the way in which we estimate these parameters.

The zonal, meridional, and vertical winds are derived by continuous radar measurements. The data are analyzed with wavelet techniques (Section 5.2) or with spectral analysis to get the dominant observed periods $2\pi/\omega_{ob}$ and vertical wavenumbers m and to estimate wind perturbations.

Stokes-parameter analysis (Section 6.3) is used to estimate polarization ellipse ratio R and the horizontal direction of wave propagation.

The solution of the three equations, polarization, dispersion and Doppler equation, gives the intrinsic frequency $\hat{\omega}$ and horizontal wavenumber k_h of a gravity wave. The polarization relation including the wind shear terms $\partial\bar{u}/\partial z$ and $\partial\bar{v}/\partial z$ is defined as

$$R = \left| \frac{f_c}{\hat{\omega}} - \frac{k}{m\hat{\omega}} \frac{\partial\bar{v}}{\partial z} \right|. \quad (2.24)$$

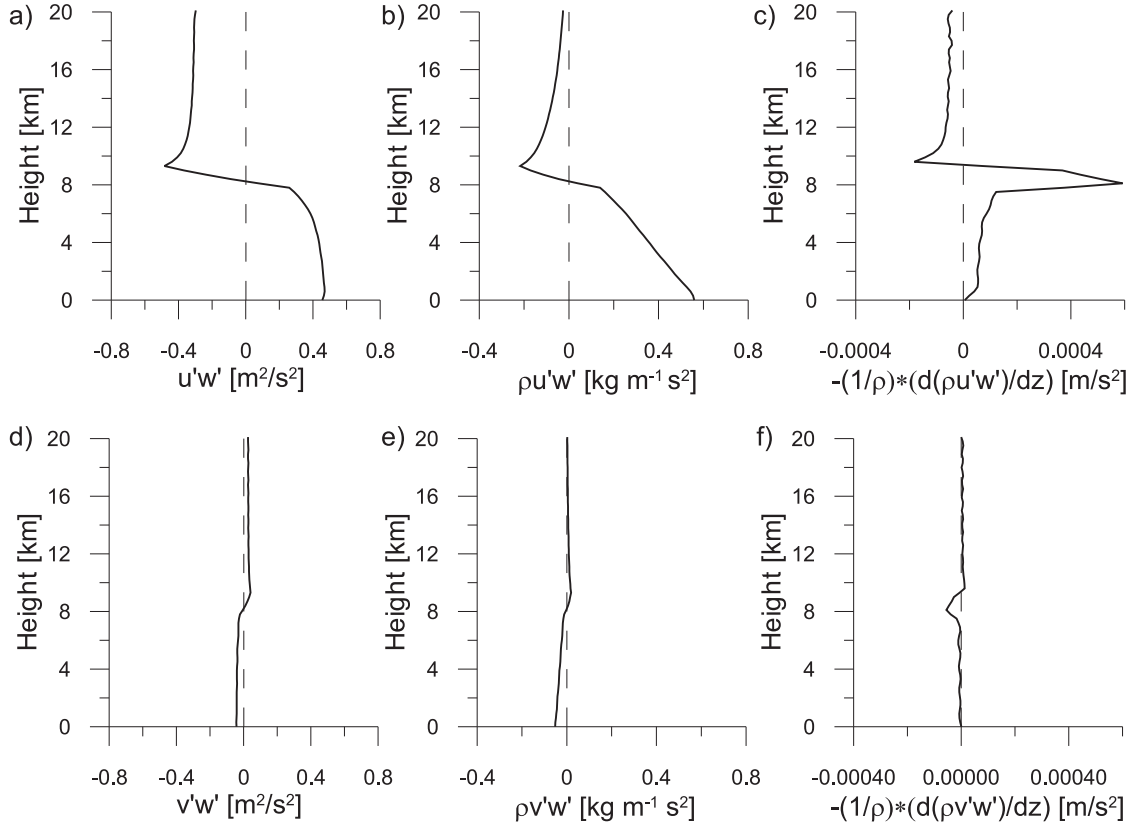


Figure 2.7: Vertical fluxes (a,d), flux densities (b,e) and mean-flow accelerations (c,f) of the zonal (upper part) and meridional (lower part) momenta.

Here the vertical wind shear effect in the background wind, as introduced by *Hines* [1989], is included by the term $\frac{\partial \bar{v}}{\partial z}$, where \bar{v} denotes the mean horizontal wind component perpendicular to the wave propagation. The dispersion relationship is given by

$$\hat{\omega}^2 = f_c^2 + \frac{N^2 k^2}{m^2} - \frac{2fk}{m} \frac{\partial \bar{v}}{\partial z}. \quad (2.25)$$

The Doppler relationship is given by Equation 2.9.

For a given location, the Coriolis frequency f_c has been calculated by

$$f_c = 2 * 7.292 \cdot 10^{-5} s^{-1} \cdot \sin \varphi \quad (2.26)$$

where φ is geographical latitude.

The Brunt-Väisälä frequency $N(z)$ can be estimated from radiosonde or lidar temperature soundings

$$N^2 = \frac{g}{T} \left(\frac{\partial T}{\partial z} + \frac{g}{c_p} \right), \quad (2.27)$$

where c_p is specific heat for constant pressure.

In the absence of temperature information in the case of pure radar investigation, mean Brunt-Väisälä frequencies are selected with values of $0.013 s^{-1}$ for the troposphere and of

0.021 s^{-1} for the stratosphere.

The mean background horizontal wind component in the direction of the wave propagation \bar{u} and the horizontal wind component perpendicular to the wave propagation \bar{v} are estimated by

$$\begin{aligned}\bar{u} &= u_x \cos \Theta + v_y \sin \Theta \\ \bar{v} &= -u_x \sin \Theta + v_y \cos \Theta,\end{aligned}\tag{2.28}$$

where u_x and v_y are the observed zonal and meridional winds, and Θ is the direction of the wave propagation. After that the vertical wind shear term $\partial\bar{v}/\partial z$ has been estimated.

The intrinsic horizontal and vertical phase velocities are

$$(\hat{v}_{ph}, \hat{v}_{pz}) = \left(\frac{\hat{\omega}}{k}, \frac{\hat{\omega}}{m} \right).\tag{2.29}$$

The intrinsic horizontal and vertical components of the group velocity are given by

$$\hat{c}_{gh} = \frac{\partial\hat{\omega}}{\partial k} = \frac{N^2 k}{\hat{\omega} m^2} - \frac{f_c}{\hat{\omega} m} \frac{\partial\bar{v}}{\partial z}\tag{2.30}$$

$$\hat{c}_{gz} = \frac{\partial\hat{\omega}}{\partial m} = -\frac{N^2 k^2}{\hat{\omega} m^3} + \frac{f_c k}{\hat{\omega} m^2} \frac{\partial\bar{v}}{\partial z}\tag{2.31}$$

The ground-based horizontal group velocity relative to observer is then given by

$$c_{gh} = \frac{\partial\omega_{ob}}{\partial k} = \hat{c}_{gh} + \bar{u}.\tag{2.32}$$

To conclude this chapter, we defined the main waves characteristics for the following discussion of different motions in the atmosphere. The physical nature of gravity wave motions is discussed with derivation of the main gravity wave characteristics under the linearized solutions of fluid-dynamical equations. Due to the broad range of properties, gravity waves are classified in high-frequency, midrange and low-frequency waves. For each case the corresponding approximations of the dispersion relationship are considered. Gravity waves are responsible for the momentum transport from the troposphere to the mesosphere. Hence, the terms of vertical fluxes, flux densities, and mean-flow accelerations are determined with their examination through a simple gravity wave simulation.

Chapter 3

Experimental methods to study gravity waves

To investigate properties of gravity waves, their generation and propagation from different sources, and to study atmospheric processes connected with gravity waves, different instruments and methods are used. All results presented in this thesis are based on VHF radar measurements, since they are able to measure 3D winds continuously with height and time resolution adapted to gravity wave parameters. Details of this technique are given in Chapter 4. Other experimental methods for the investigation of gravity waves based on estimations of temperature, wind, and energy perturbations are:

- **Radiosonde** measurements have been used for many years and still remain a very important tool for weather forecasting. The radiosonde usually contains pressure, temperature and humidity sensors. The outputs of these sensors vary in flight and are transmitted to the monitoring station. For the determination of winds, the sonde pinpoints its own position, using the **Global Positioning System** (GPS), and relays its location back to the ground station. From temporal changes of these locations, the wind speeds and directions are computed and used in the following gravity wave analysis. Radiosonde soundings have a vertical coverage from ground level up to ~ 35 km with a height resolution of 50 m. This allows us to examine accurately properties of gravity waves in the troposphere and lower stratosphere [*Guest et al.*, 2000]. The monitoring stations can cover different terrains, such as tropical islands, midcontinent plains, mountainous regions, or even in the Arctic. Measurements from these stations are useful to distinguish source effects from propagation effects of gravity waves and to get mean climatologies [*Allen and Vincent*, 1995; *Wang and Geller*, 2003; *Schöllhammer*, 2002].
- **LIght Detection And Ranging (lidar)** instruments transmit the light to the atmosphere. Some of this light is reflected/scattered back to the instrument where it is analyzed. The change in the properties of the backscattered light enables us to determine properties of the atmosphere, like the temperature, aerosol concentration as a function of altitude from the lower stratosphere (10 km altitude) up to the upper mesosphere (90 km altitude). The emitted laser beam has a narrow width. This advantage helps to locate, only with clear sky conditions and mostly during night time, the target more accurately in comparison to radar. Through the combined use of three different temperature lidar methods, the height range was recently extended from the planetary

boundary layer up to the lower thermosphere (1-105 km) [Alpers *et al.*, 2004]. Using these techniques, first gravity wave analyses have been successfully compared with model simulations [Rauthe *et al.*, 2005]. A few lidars allow us also to measure the wind, which has been used to estimate vertical and horizontal wavenumbers of gravity waves and their intrinsic and apparent frequencies [Hertzog *et al.*, 2001]. Combination of lidar measurements with radar provides the excellent possibility to investigate gravity wave content from the troposphere up to the stratosphere [Schöch *et al.*, 2004].

- The **European Center for Medium-range Weather Forecasts (ECMWF)** is an international organization supported by 25 European states. The center provides weather forecast data and manages a super-computer facility which provides resources for weather forecasting research and computer modelling of the global weather. The ECMWF data have a global coverage with a relatively accurate forecast in the height range 0–30 km and gives us a description of the atmosphere, which we can interpret in terms of "weather" - rain, temperature, sunshine and wind. The ECMWF data are available with a time resolution of 6 hours and as shown by Plougonven and Teitelbaum [2003], can be used for the investigation of the generation of large-scale inertia-gravity waves and their temporal-spatial behavior, but not for their evaluation. For gravity wave modelling these data are used to initialize the Mesoscale Model (MM5) [Zülicke and Peters, 2004].
- **Satellites** are able to give us considerable insight into the middle atmosphere. They provide valuable real-time cloud photographs, locate and accurately track hurricanes and typhoons, and carry many instruments used to measure the temperature, energy, and vertical wavenumbers. The main advantage of satellite measurements is their global, fairly uniform, coverage. However, a satellite needs approximately 36 days for global description of the atmosphere over the Earth [Khattatov *et al.*, 1996]. Satellites are limited in their horizontal (10-15 km) and vertical (~ 1 km) resolutions and in the duration of the utilization of these expensive instruments. From this satellite observation technique, horizontal winds and information near the wave source regions in the troposphere cannot be obtained, but a global mapping of energy and a morphology of gravity wave activity in the stratosphere can be derived [Preusse *et al.*, 2000; Tsuda *et al.*, 2000; Ratnam *et al.*, 2004]. As shown by Wu and Waters [1996], Jiang *et al.* [2002], Jiang *et al.* [2004], gravity waves distribution, generation, propagation and interaction with background atmospheric flows are investigated successfully by the analysis of small-scale radiance variances from the Upper Atmosphere Research Satellite (UARS) Microwave Limb Sounder (MLS).
- **Rockets** transport small, highly sensitive instruments up to mesospheric/lower thermospheric heights. These allow measurements of temperature and trace constituent concentrations. Rocket measurements give a snapshot of the atmosphere with a very fine vertical resolution, but they are expensive. They must therefore be used sparingly and do not have very good time coverage. With rocket measurements the temperature is measured with a high altitude resolution which enable us to study the spectra of gravity waves in the mesosphere and their interactions with other atmospheric phenomena like Noctilucent Clouds (NLC) [Rapp *et al.*, 2002] or Polar Mesosphere Summer Echoes (PMSE) (see Chapter 8). Furthermore, rocket experiments are used to transport **falling spheres** into mesospheric heights to investigate the wind, the density and the temperature in the middle atmosphere. The sphere is normally deployed at an altitude 115 km where it free-falls under gravitational and wind forces. The surface of

the sphere is metalized to enable radar tracking for position information as a function of time in height range from 35 km up to 90 km, which is used to estimate the atmospheric density, winds, pressure and temperature and also gravity waves [Eckermann and Vincent, 1989; Schmidlin et al., 1991; Lübken, 1999; Müllemann, 2003].

A similar idea is applied in the **foil chaff** technique. The foils are released by the rocket near the apogee point and form a foil cloud, which is then tracked by precision radar. Very detailed information about horizontal winds can be achieved with measurements of 50 points per second (50 Hz), which has been applied to investigate gravity waves in the mesosphere [Wu et al., 2001].

- **Aircraft** observations can be used to measure following atmospheric parameter: temperature, pressure, humidity, wind speed and direction, turbulence, icing, and the state of the sky. The observation includes the position and the altitude of the aircraft and time of observation. The main disadvantage is the time limitation of flight hours because they are expensive. But in situ aircraft observations enable us to operate high-quality instruments during in flight. These measurements can be used for observations of wind and temperature variances with further estimations of gravity waves, mostly in combination with mesoscale models [Dörnbrack et al., 2002; Buss et al., 2004].

Additionally, gravity waves in the boundary layer are investigated by a microbarograph array with pressure sensors forming a ground-based network [Hauf et al., 1996]. This technique evaluates pressure fluctuations and has been used e.g. to analyze interactions between gravity waves and deep convection in the atmosphere [Finke, 1995].

The techniques used for measurements are divided in two main groups, namely remote sensing and in situ measurements. The radar, lidar, and satellite measurements belong to the remote sensing experiments, whereas the radiosonde, falling sphere, rocket and aircraft measurements are in situ observations. In situ means that the measurements are made directly on the observed object usually with high accuracy at one single point. In remote sensing, where the accuracy is generally lower, large areas can be covered with a single measurement. These different characteristics mean that in situ and remote sensing measurements complement each other. In situ techniques have advantages when studying details of a process, or when it is sufficient to measure at one or a few different places, whereas remote sensing is preferable when continuous measurements from a remote or inaccessible area are required, or large-areas need to be covered.

Studies of different problems require measurement systems of varying accuracy and precision. Usually it is necessary to find a compromise between spatial resolution and coverage, and the exact balance is determined by the phenomena that are being studied. For global studies, good coverage is essential, which generally limits the resolution. When studying local environmental problems, resolution is often most important. If the measurements are performed over a short time period, it is usually only relative changes that are important, and hence high precision is required.

In the following we will concentrate on continuous radar measurements of winds to locate accurately wave events in time scale and to resolve main characteristics of gravity waves with high accuracy. Particular attention is devoted to the usage of collocated radars as a special form of a radar network to improve the statistical reliability of the results as well as the knowledge on the mesoscale behavior of gravity waves.

Chapter 4

Radar fundamentals

Radar is a general technique to observe different types of targets. A radar can be designed to measure a bullet, while another may observe a planet. For each case different radar frequencies are used to acquire data and to investigate different phenomena.

The targets of radar observations described in this thesis are clear atmospheric echoes from the Earth's atmosphere produced by fluctuations of atmospheric refractive index. We will refer to this kind of radar as atmospheric radar. Atmospheric radars usually use frequencies of MF/HF (1-30 MHz), VHF (30-300 MHz), or UHF (300 MHz-3 GHz) bands. Most atmospheric radars observe a narrow angular range around the zenith with larger vertical coverage.

In contrast to radiosonde data, which is usually spaced at least 3 or 6 hours apart and restricted to altitudes below 35 km, the atmospheric radars offer the advantage of time resolutions of a few minutes and, if powerful enough, can obtain measurements from altitudes up to some 100 km, but with a gap between 25 and 60 km. The lowest observable height, which is usually limited by the switching speed from transmission to reception, ranges from a few hundred meters to several kilometers. The measurements with radar can be continuous, but of course these observations require some reflectivity in the atmosphere. In this chapter we give an overview of the atmospheric radar technique. The main concepts discussed here are well described e.g. in *Atlas* [1990], *Doviak and Zrnic* [1984] and *Lafaysse* [1994].

4.1 Radio Refractive Index and Radar equation

Characteristics of the atmosphere seen by radio waves in the absence of liquid water is expressed in terms of the refractive index n which is defined as

$$n = \frac{c}{v}, \quad (4.1)$$

where c is the speed of light in free space and v is the velocity of the radiowave in the air. Macroscopic changes of n in space cause refraction or reflection, and microscopic changes cause scattering. Both processes are used by atmospheric radar.

Major contributions to n at frequencies of MF/HF to UHF bands are expressed approximately as [*Balsley and Gage*, 1980]

$$n - 1 = \frac{3.73 \times 10^{-1} e}{T^2} + \frac{77.6 \times 10^{-6} P_a}{T} - 40.3 \frac{N_e}{f_0^2}, \quad (4.2)$$

where e (mb) is the partial pressure of water vapor, P_a (mb) is total atmospheric pressure, T (K) is absolute temperature, N_e is the number density of electrons per m^3 , and f_0 is the operating frequency in Hz.

The first term, proportional to e/T^2 , represents the contribution from water vapor. As it is well known, the water molecule has a dipole moment, which varies with frequency. At extremely high frequency of light, only the polarized electric field of the water molecules counts for the refractivity. At lower frequencies of radiowave, the water molecules are not only polarized but they also reorient themselves rapidly enough to follow the changes of electric field. As a result, the contribution of the water vapor to n is greater for radio than for optical frequencies [*Battan, 1973*].

Above the tropopause height of 10-15 km, the partial pressure of water vapor becomes negligibly small. The second term, proportional to P/T , due to dry air becomes dominant in this region. Since the major constituents of the Earth's atmosphere, N_2 and O_2 , do not change their mixing ratio largely throughout the middle atmosphere of up to around 100 km, the coefficient stays unchanged. Unlike the first term due to the water vapor, this term is frequency independent, being the same for light and radio waves.

While these two terms concern the neutral atmosphere, the third term, proportional to N_e , gives the contribution from free electrons. This term is negligible below about 50 km, but is dominant at ionospheric heights above 60-70 km.

Using the differences in the echo characteristics, the scattering processes are divided in following groups:

- a) Bragg scatter or turbulence scatter results from irregularities in the refractive index, which is randomly distributed in the observed radar volume [*Balsley and Gage, 1980*];
- b) Fresnel reflection or partial reflection is produced by stable horizontal layers with a distinct refractive index gradient, which yields a strong, slowly varying signal [*Röttger, 1980*];
- c) Fresnel scatter or diffuse reflection occurs when several or many refractive index discontinuities exist, which produce a strong coherent signal [*Gage et al., 1981*].

These scatter mechanisms are presented in Figure 4.1. The Bragg scatter has a scale size of one-half the radar wavelength and results into homogeneously random radar echoes. The Fresnel reflection produces a sharp peak in the echo power, whereas in the case of the Fresnel scatter the radar echoes appears as a series of smaller peaks. The discrimination between the Fresnel scatter and Fresnel reflection depends on the height resolution Δz of the radar experiments.

Scattering from fluctuations in the refractive index n dominates the received echo of the atmospheric radar. Statistical fluctuations of the electron density due to random thermal motion of electrons and ions can be strong enough in the ionosphere to cause detectable scattering. This component is called incoherent scattering because scattered waves from individual electrons are random in phase. Rapidly increasing with height, echo power is then proportional to the number of electrons illuminated by the radar.

Fluctuations due to atmospheric turbulence are known to be the major source of scattering in the upper stratosphere and mesosphere. This component is often called coherent scattering in contrast to the incoherent scattering in the ionosphere. The main difference of coherent scattering from incoherent scattering is that fluctuations of n are caused by macroscopic

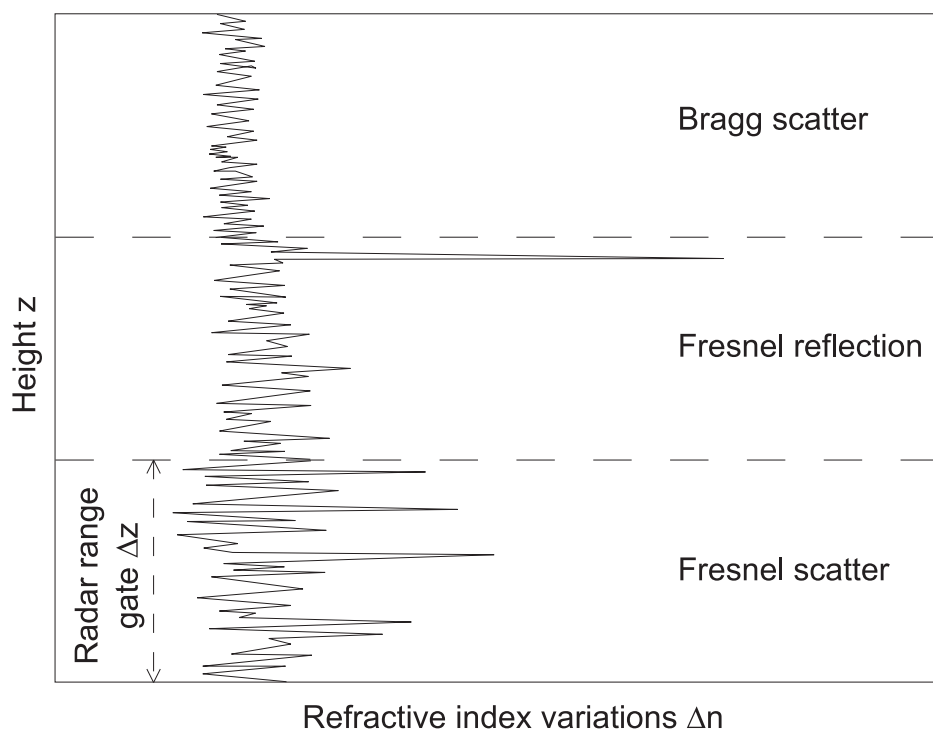


Figure 4.1: Schematic representation of the refractive index variations Δn . The radar range is indicated by Δz . (After Röttger and Larsen [1990]).

motions of air parcels with a large number of molecules and/or electrons, which contribute to the scattered electric field coherently in phase.

The strength of the received echo as a function of radar parameters and scattering cross sections is given by the radar equation, which has been formulated for a variety of situations [Tatarskii, 1961; Gage and Balsley, 1980; Doviak and Zrnic, 1984]. Here we will only quote the equations for the two cases, uniformly distributed targets and single sharply bounded discontinuity.

For isotropic scattering from distributed targets, the received power for scattering of a radar pulse of length ΔR at range R_0 is given by

$$P_r = \frac{\pi}{64} \frac{P_t A_e \alpha_r \Delta R}{R_0^2} \eta_r, \quad (4.3)$$

where P_t is the transmitted power, A_e is the effective antenna area, α_r is the total efficiency factor of the system, and η_r is the volume reflectivity. As the volume illuminated by the radar increases with the square of range, the volume scatter has an inverse square dependence on radar range, in contrast to the R_0^{-4} dependence of a point scatter.

For reflection from a single horizontal layer, which is sharply bounded, i.e. Fresnel reflection, the radar equation is given as

$$P_r = \frac{P_t A_e^2}{4\lambda_r^2 R_0^2} |\rho_r|^2, \quad (4.4)$$

with λ_r the radar wavelength and ρ_r the amplitude reflection coefficient.

With the appropriate expressions for the volume reflectivity η_r and the amplitude reflection coefficient ρ_r , the power of the radar echoes can be computed.

4.2 Beam forming

To get information for a range ΔR , pulsed operation is usually used to discriminate the distance R_0 (Figure 4.2). Radar pulses of a certain duration Δt_T are transmitted at time intervals of the inter-pulse-period T_{ipp} (Pulse 1). An echo pulse received at time T_R after transmission (Pulse 2) has then travelled over a distance cT_R , where $c = 3 \cdot 10^8$ m/s is the speed of light. For a mono-static radar, i.e. a radar with collocated transmitting and receiving antennas, this echo can then be attributed to a scatterer at range $R_0 = cT_R/2$ from the radar in the beam direction. Due to the limited bandwidth of the receiving path, the signal detected at the receiver at time T_R after transmission is effectively an average over a time interval Δt_R . For optimal operation, the receiver bandwidth is matched to transmitted pulse so that $\Delta t_T = \Delta t_R = \Delta t$. The echo pulse then contains information about the range interval from $R_0 - c\Delta t/2$ to $R_0 + c\Delta t/2$. Usually, the range resolution is expressed as $\Delta R = c\Delta t/2$, which corresponds to the full-width half-maximum of the weighted function. If the echoes from distant ranges are strong enough, range aliasing can occur (Pulse 3). Here the echo pulse is received after another pulse has been transmitted, and it is not clear, to which of the transmitted pulses the echo belongs. However, as the power of volume-scattered radar echoes has an inverse square dependence on radar range, the range-aliased echoes are generally much weaker than the direct ones. A high maximum unaliased range and small height resolution are desirable for most applications, but, in practice, the choice is limited by radar parameters like transmitted power and receiving bandwidth. Increasing the inter-pulse-period T_{ipp} increases the maximum unaliased range

$$R_0^{max} = c \frac{T_{ipp} - \Delta t}{2}, \quad (4.5)$$

but it also decreases the average transmitted power

$$\overline{P}_t = \frac{\Delta t_T}{T_{ipp}} P_t, \quad (4.6)$$

where P_t is the (peak) transmitted power, and, hence, decreases the maximum range of usable radar echoes. The height resolution ΔR of a radar system is limited by the bandwidth of the (receiving) system and the requirement of sufficient average transmitted power \overline{P}_t .

4.3 Radar measurements of wind

To make use of the backscattered signals from atmosphere in a qualitative manner in terms of physical parameters of geophysical interest, we apply the Taylor-hypothesis, that these scatters move with a mean wind $\mathbf{u} = (u, v, w)$, so that the determination of the 3-dimensional wind vectors is possible by measuring the motion of the scatters.

There are at least two different approaches for the determination of the mean winds. One is called the "Doppler Beam Swinging" (DBS) method and utilizes large antenna arrays with correspondingly narrow radiation patterns by measuring the Doppler frequencies for different radar beams tilted sequentially in different directions. The second class is called the spaced

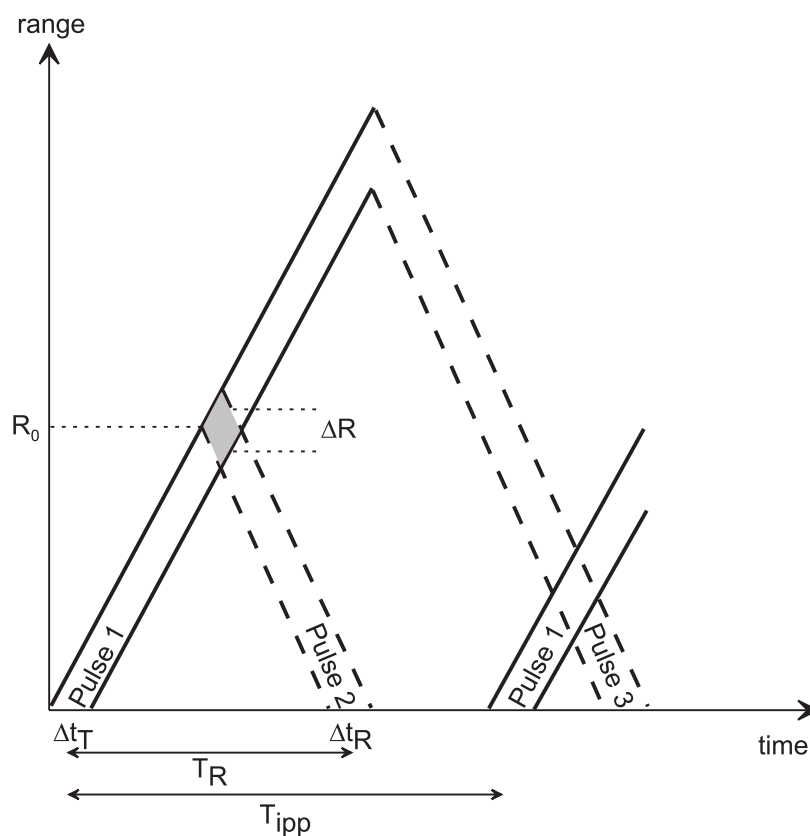


Figure 4.2: Range-time diagram of pulsed radar operation, where T_R is the received pulse time, T_{ipp} is pulse interval, ΔR is the range resolution, R_0 is range to target, Δt_T and Δt_R are pulse durations (After Röttger [1989]).

antenna method and calculates the winds by correlation analyses of simultaneously sampled time series of spatially separated (spaced) antennas/receiving channels.

4.3.1 Doppler techniques

The Doppler frequency shift of echoes f_d from a moving target relative to the radar is given by

$$f_d = \frac{2f}{c}v_d, \quad (4.7)$$

where v_d is the line-of-sight component of the velocity vector \mathbf{v} of the target relative to the radar. Since the maximum velocity encountered in the atmosphere is about 100 m/s, $|f_d| < 1$ kHz for any frequency f of less than 1 GHz. A typical value of f_d for 50 MHz radar is, for example, around 3 Hz, which corresponds to a line-of-sight velocity of 9 m/s. The line-of-sight velocity measured by a radar with the Doppler technique is the projection of velocity vector to the radial direction.

The Doppler-Beam-Swing (DBS) method makes use of multiple antenna beams, which are oriented in different directions (Figure 4.3). The velocity vector is computed from the line-of-sight velocities from these directions. Here we use the assumption that the velocity field is uniform in space and time over the volume which contains the range cells used to compute

a velocity vector.

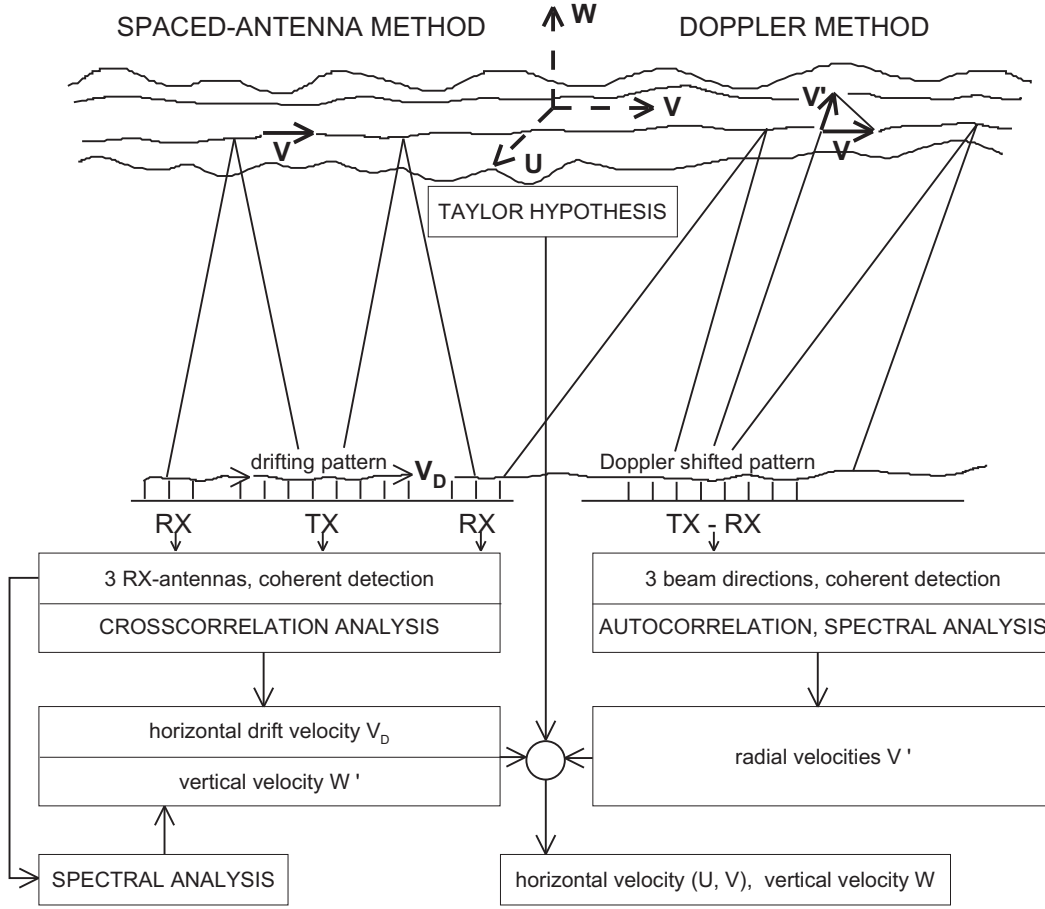


Figure 4.3: The principles of three dimensional velocity measurements with the spaced antenna drifts and the Doppler beam swinging method in the troposphere, stratosphere and mesosphere (After Röttger [1989]).

The line-of-sight component of the wind velocity vector $\mathbf{v} = (v_x, v_y, v_z)$ at a given height is expressed as

$$v_d = \mathbf{v} \cdot \mathbf{i} = v_x \cos \theta_x + v_y \cos \theta_y + v_z \cos \theta_z, \quad (4.8)$$

where \mathbf{i} is a unit vector along the antenna beam direction, and θ_x , θ_y and θ_z are the angles between \mathbf{i} and x , y and z axis, respectively. If we measure v_d at three different beam directions i_1 , i_2 and i_3 , we can obtain an estimate of \mathbf{v} as

$$\mathbf{v} = \begin{pmatrix} \cos \theta_{x1} & \cos \theta_{y1} & \cos \theta_{z1} \\ \cos \theta_{x2} & \cos \theta_{y2} & \cos \theta_{z2} \\ \cos \theta_{x3} & \cos \theta_{y3} & \cos \theta_{z3} \end{pmatrix}^{-1} \begin{pmatrix} v_{d1} \\ v_{d2} \\ v_{d3} \end{pmatrix} \quad (4.9)$$

If we observe more than three directions, then the estimation of \mathbf{v} is realized by the least-squares method, minimizing the residual of the following expression:

$$\varepsilon_v^2 = \sum_{i=1}^m (v_x \cos \theta_{xi} + v_y \cos \theta_{yi} + v_z \cos \theta_{zi} - v_{di})^2, \quad (4.10)$$

where m is the number of beam directions. The necessary condition for \mathbf{v} to give the minimum is that partial derivatives of ε_v^2 with respect to all three components of \mathbf{v} are zero:

$$\frac{\partial \varepsilon_v^2}{\partial v_j} = 0 \quad (j=x, y, z). \quad (4.11)$$

This set of equations can be solved in terms of \mathbf{v} as

$$\mathbf{v} = \begin{pmatrix} \sum \cos^2 \theta_{xi}, & \sum \cos \theta_{xi} \cos \theta_{yi}, & \sum \cos \theta_{xi} \cos \theta_{zi} \\ \sum \cos \theta_{yi} \cos \theta_{xi}, & \sum \cos^2 \theta_{yi}, & \sum \cos \theta_{yi} \cos \theta_{zi} \\ \sum \cos \theta_{zi} \cos \theta_{xi}, & \sum \cos \theta_{zi} \cos \theta_{yi}, & \sum \cos^2 \theta_{zi} \end{pmatrix}^{-1} \begin{pmatrix} \sum v_{d1} \cos \theta_{xi} \\ \sum v_{d2} \cos \theta_{yi} \\ \sum v_{d3} \cos \theta_{zi} \end{pmatrix} \quad (4.12)$$

where the summations are taken for $i = 1$ to m .

A potential problem with the Doppler technique is the accurate determination of the effective beam pointing angle which is smaller than the antenna beam direction due to anisotropy of scatterers [Hocking *et al.*, 1990]. But estimate of aspect sensitivity of radar echoes enable to calculate the effective beam pointing angle [Rüster, 1994a].

4.3.2 Spaced Antenna techniques

In the spaced antenna (SA) method, the diffraction pattern produced by a vertically directed radar beam scattering of irregularities in the atmosphere is sampled at a number of spaced receiving antennas (Figure 4.3). Each of the antennas essentially samples a cross section of the diffraction pattern. In the presence of horizontal wind, the fluctuations in echo strength at spaced antennas show relative time displacements, from which the apparent velocity \mathbf{v} of the diffraction pattern on the ground can be calculated.

The history of spaced antenna technique [Briggs *et al.*, 1950] has been reviewed by Briggs [1993], and theoretical details are summarized in Briggs [1984]. Here we will consider only the principle of the technique.

The space-time correlation function of the received signal pattern $q(x, y, z)$ on the ground plane is

$$\rho_c(\xi, \eta, \tau) = \frac{\langle q(x, y, z)q(x + \xi, y + \eta, t + \tau) \rangle}{|q(x, y, z)|^2}, \quad (4.13)$$

where $\langle \rangle$ means to take an ensemble average, which is often replaced by a temporal average in practical applications. This correlation function represents the statistical relations of the signal pattern at two points with a separation (ξ, η) on the ground and with a time difference of τ . For stationary pattern, we assume that the correlation function has a form

$$\rho_c(\xi, \eta, \tau) = \rho_c(J\xi^2 + O\eta^2 + K\tau^2 + 2M\xi\eta). \quad (4.14)$$

This assumption implies that the spatial and temporal correlations have the same functional shape, but the shape is arbitrary. Although this is not real in a rigorous sense, it is an acceptable approximation for most of the correlation functions at least around their origin.

We next suppose that the pattern is moving with a velocity $\mathbf{v} = (v_x, v_y)$. If we move the coordinates also at this velocity, then Equation 4.14 remains unchanged for the moving coordinates. The expression for the stationary coordinates is therefore obtained after a linear transformation of coordinates that

$$\rho_c(\xi, \eta, \tau) = \rho_c \left\{ J(\xi - V_x \tau)^2 + O(\eta - V_y \tau)^2 + K\tau^2 + 2M(\xi - V_x \tau)(\eta - V_y \tau) \right\}, \quad (4.15)$$

which is rewritten as

$$\rho_c(\xi, \eta, \tau) = \rho_c(J\xi^2 + O\eta^2 + K\tau^2 + 2F\xi\tau + 2G\eta\tau + 2M\xi\eta). \quad (4.16)$$

If we have two spaced receivers, we can determine the shape of the cross-correlation as a function of τ for a given set of (ξ, η) . Since Equation 4.16 is a function of second-order polynomial of τ , it is possible to determine three unknowns by fitting them to the measured cross-correlation function. It is thus clear that three spaced receivers, which provide us with two sets of independent cross-correlation functions, are sufficient to determine all coefficients in Equation 4.16. If we have more than three receivers, we can determine the coefficients in a least-squares manner as in the case of the DBS method (Section 4.3.1).

Once the coefficients are determined, we can retrieve the velocity vector \mathbf{v} from these coefficients. By comparing Equations 4.15 and 4.16, we obtain

$$\begin{aligned} Jv_x + Hv_y &= -F \\ Ov_y + Hv_x &= -G \end{aligned} \quad (4.17)$$

These equations can be readily solved to give (v_x, v_y) . The vertical component of the velocity vector needs to be determined separately from the Doppler shift of the echo.

From a practical point of view, the DBS and SA methods have their own advantages and disadvantages. The DBS is a straightforward mathematical method. However, it uses different volumes for analysis with approximation of uniform velocity. The SA method is a more complicated estimation of space-time correlation function determined from a single volume of the target. SA technique requires at least three sets of small receiving antennas and receivers with equal capability. The DBS method requires, on the other hand, a steerable larger antenna. The aspect sensitivity plays an important role in DBS technique, whereas in SA analysis the influence of noise on the correlation function takes place. The accuracy of the velocity estimates is known fairly well for the DBS method. The accuracy in the SA method shows some more dependencies from antenna spacing, noise, record length.

4.4 Description of the radars

The investigations presented in this thesis are based on observations mainly made by collocated radars. At midlatitudes we used the OSWIN-53.5 MHz-VHF radar (Ostsee Wind Radar) located at Kühlungsborn and the 482 MHz-wind profiler at Lindenberg. At high

latitudes in the vicinity of the Scandinavian mountain ridge we processed data from the ALOMAR VHF Radar ALWIN in Andenes and Esrange MST Radar in Kiruna. Details of the radar parameters used are summarized in Tables 4.1 and 4.2.

4.4.1 OSWIN VHF radar and UHF wind profiler

	OSWIN VHF radar	UHF wind profiler
Geographical location	54.1°N, 11.8°E	52.2°N, 14.1°E
Operating frequency	53.5 MHz	482 MHz
Peak power/duty cycle	90 kW/ 5 %	16 kW/ 10 %
Transmitting antenna	144 Yagi array	Phased array (CoCo)
Antenna aperture (area)	1900 m ²	140 m ²
Half-power beam width	6°	3°
Pulse length	4 μs	3.3 μs
N of transmitter/receiver	6	1
Code	Single pulse	8-bit-Complementary code
Coherent integration	128	30
Vertical resolution	300 m	250 m
Altitude range	1 - 18 km	2.7 - 16.0 km
Time resolution	~ 1 min	~ 33 sec
Methods	DBS, (SA)	DBS

Table 4.1: Parameters of the VHF radar OSWIN at Kühlungsborn and the UHF wind profiler at Lindenberg

The OSWIN VHF radar has been operating at Kühlungsborn since autumn 1999. The radar system was designed for continuous measurements and is running either in the spaced antenna (SA) or in the Doppler Beam Swinging mode (DBS). The antenna array consists of 144 four-element Yagis resulting in a transmitting half-power beam width of 6°. The beam is steerable in the vertical direction and towards the North, East, South, and West with an off-zenith angle of 7°. For the investigations presented here, we used 1024 point complex time series sampled with 0.05 s. The radar resolves a height region from 1 to 18 km. Data are averaged over 30 min for further investigations.

The 482 MHz wind profiler belongs to the Meteorological Observatory Lindenberg of the German Weather Service (DWD). The wind profiler is a fully coherent Doppler radar system with an additional RASS (Radio Acoustic Sounding System) component to estimate sound virtual temperatures [Gurvich *et al.*, 1987]. It has been in operation since August 1996 as a prototype system for a planned operational DWD profiler network [Lehmann *et al.*, 2003]. Wind measurements are carried out in the DBS mode using the vertical and four oblique beam directions with an off-zenith angle of 15° [Hogg *et al.*, 1983]. In contrast to the data processing technique used with the OSWIN VHF radar a statistical method for the incoherent integration of 17 individual spectra has been applied to reduce the noise variance and to suppress intermittent clutter contamination [Merritt, 1995].

4.4.2 ALOMAR VHF radar ALWIN and Esrange MST radar

Both radars, the ALOMAR VHF Radar ALWIN in Andenes and Esrange MST Radar in Kiruna, separated by about 200 km, have comparable characteristics. They are using the same antenna size and nearly the same operation frequency 53.5 and 52.0 MHz. Some details of the radar parameters are summarized in Table 4.2.

	ALWIN VHF Radar	Esrange MST Radar
Geographical location	69.2°N, 16.0°E	67.9°N, 21.9°E
Operating frequency	53.5 MHz	52.5 MHz
Peak power/duty cycle	36 kW/ 5 %	72 kW/ 10 %
Transmitting antenna	144 Yagi array	144 Yagi array
Antenna aperture (area)	1900 m ²	2025 m ²
Half-power beam width	6°	5°
Pulse length	4 μs	4 μs
N of transmitter/receiver	6	6
Code	Single pulse	Single pulse
Coherent integration	256	256
Vertical resolution	300 m	300 m
Altitude range	1 - 18 km	1 - 18 km
Time resolution	~ 2 min	~ 2 min
Methods	DBS, SA(FCA)	SA(FCA)

Table 4.2: Parameters of the VHF radar ALWIN at Andenes and the Esrange MST radar at Kiruna

The Esrange 52.0 MHz VHF radar (ESRAD) [Chilson *et al.*, 1999] as well as the Andenes 53.5 MHz VHF radar (ALWIN) [Latteck *et al.*, 1999] measure wind parameters in the ST mode at the height range of 2-18 km with a resolution in height of 300 m and in time of 2 min, respectively. The transmitter and the data acquisition system were built by ATRAD (Atmospheric Radar Systems Pty. Ltd, Thebarton, S.A., Australia). Wind measurements are carried out in the SA mode using the Full Correlation Analysis (FCA) method. For further investigations in this work the data are also averaged over 30 minute intervals.

4.4.3 Comparisons with ECMWF data

The advantage of radar technique is evident by a comparison of the winds measured by radars with the reanalysis data from the European Center for Medium-Range Weather Forecast (ECMWF). Such analyses of operational centers, available with a temporal resolution of 6 hours are commonly used in observational studies to describe the synoptic-scale situation within which smaller-scale phenomena are investigated from measurements.

For example, 6 hourly averaged mean zonal and meridional winds measured by the OSWIN radar from 14 December to 22 December 1999 are shown in Figure 4.4(a,b). The mean zonal and meridional winds derived from the ECMWF reanalysis data for the same period are

shown in Figure 4.4(c,d).

The wind fields show similar structures in the troposphere and lower stratosphere. The zonal wind increases until the end of 18 December and then decreases. The ECMWF zonal wind has the more denoted peak in the time as well as in the height. The maximum averaged radar wind is 40 m/s, whereas the wind maximum derived from ECMWF at about 9 km is 50 m/s. The meridional winds show two similar minima at 21 UT 16 December, and 21 UT 20 December. The minimum jet stream reaches the value -35 m/s at the heights between 8-9 km. But the wind from the radar measurements resolves a higher variability due to the better time resolution, as shown in Figure 4.4(e,f), which show the zonal and meridional winds with a time resolution of 30 minutes. The amplitude of winds varies from -10 m/s up to 50 m/s and from -40 m/s up to 20 m/s for in zonal and meridional directions, respectively. This gives a good opportunity to investigate atmospheric phenomena like gravity waves with a high temporal and spatial resolution.

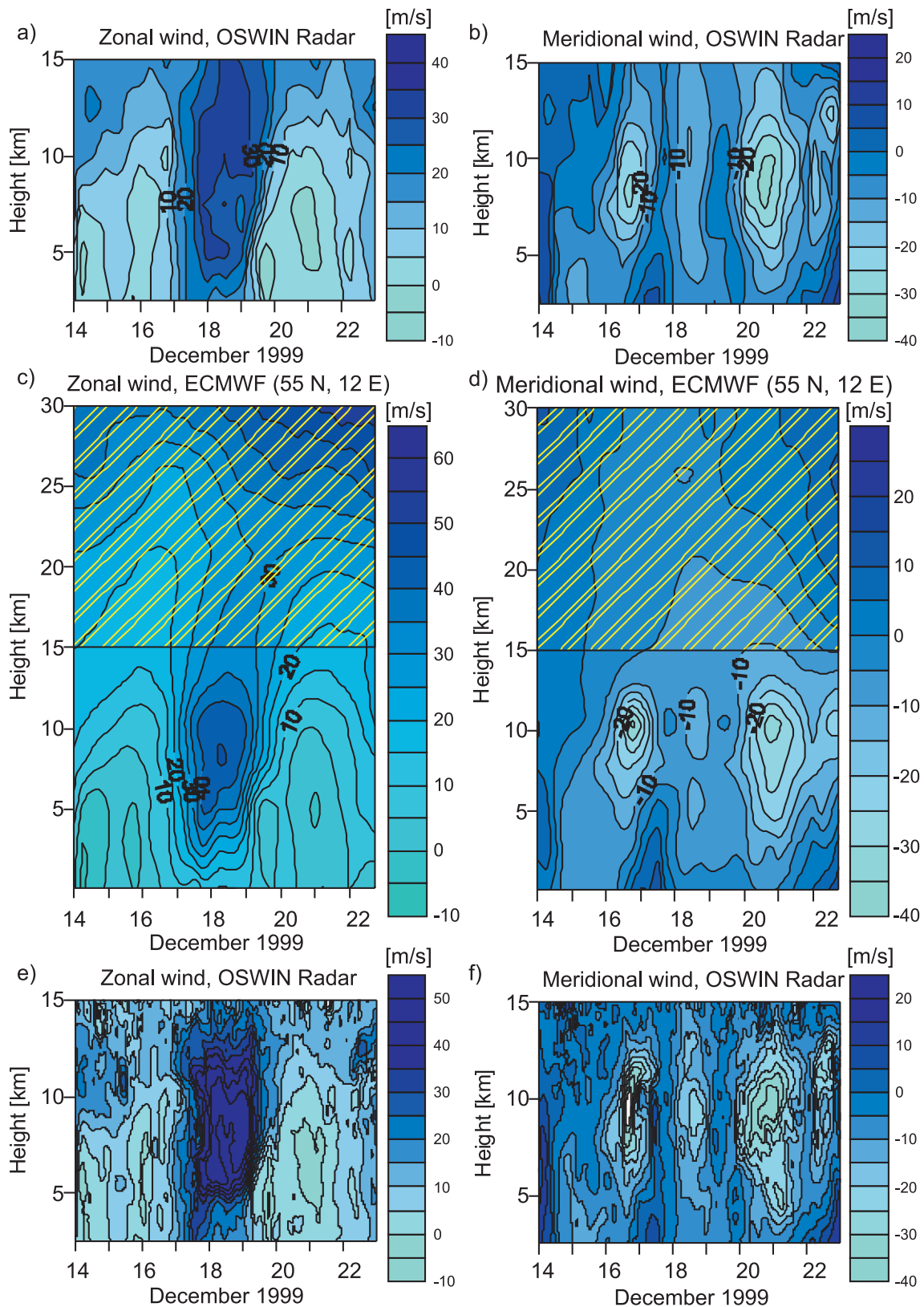


Figure 4.4: Six hourly averaged mean zonal and meridional winds measured by OSWIN radar (a,b) and derived from ECMWF reanalysis data (c,d) at Kühlungsborn from 14 - 22 December 1999. (e,f) are the same as (a,b), but with a better time resolution of 30 min. The shaded area shows the heights where radar data are unavailable.

Chapter 5

Detection of gravity waves

The calculation of gravity wave parameters is based on wind perturbations, which have been estimated from the wind measurements after linear interpolations to substitute missing values. In general the perturbations can be described by variations of amplitude $\psi(x, z, t)$ of the wind components

$$\psi(x, y, z, t) = |\psi| \cdot \exp(i(kx + ly + mz - \omega_{ob}t)), \quad (5.1)$$

where k , l , m are zonal, meridional and vertical wavenumbers, respectively, and ω_{ob} is the wave frequency, observed at a fixed location.

In practice, the wind profile often contains a superposition of different gravity waves and these waves may be quite different in frequency and wavelength and appear at a definite time and height. In order to get meaningful results, these waves have to be detected and isolated.

The Fourier transform is well known and a widely used technique in spectral analysis for many years. It allows to investigate spectral distribution of the waves, to separate dominant frequencies and suppress unwanted perturbations. As improvement of the Fourier transform, the wavelet technique is becoming a powerful tool for the examination of localized variations. Both methods discussed in the following chapter are used to filter gravity waves from radar wind measurements. Finally, the bispectral analysis is presented as a technique to investigate whether additional gravity waves have been generated by nonlinear wave-wave interactions between different waves.

5.1 Bandpass filtering with a Fourier technique

The estimation of wind perturbations from measured mean winds can be done easily by subtraction of trends or fitted polynomials. A more appropriate way consists in the application of digital band pass filtering techniques with well defined bandwidths. Here we are applying a bandpass filtering with the Fourier technique by using the Fast Fourier transform for the detection and separation of waves with dominant frequencies.

The block-scheme of the filtering applied on time series of horizontal winds is presented in Figure 5.1, starting with measured winds (upper left panel) to get finally the wind perturbations (lower right panel). Suppose that we have a signal in a certain frequency band that we want to filter (Figure 5.1a). The application of the FFT transform on discrete sampled data assumes that the samples can be continued without jumping transition, to avoid sidelobes and unwanted responses. Therefore, the signal is multiplied by the Hanning window (Figure 5.1b,c). Then the mean contribution of each frequency can be obtained by application

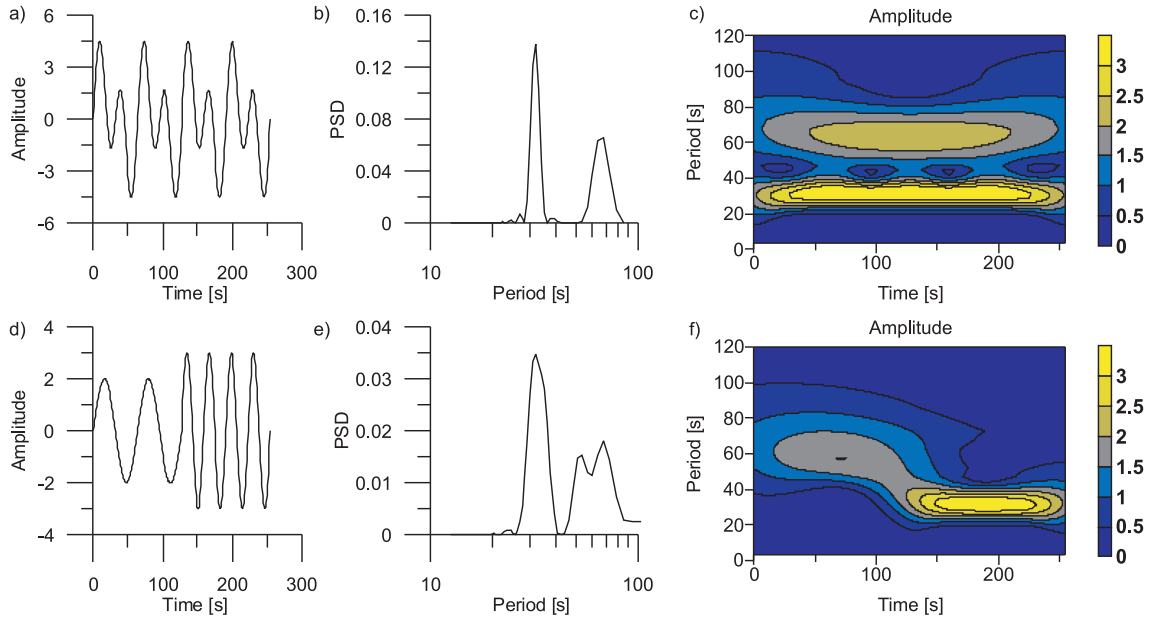


Figure 5.3: Fast Fourier (b, e) and Wavelet (c, f) transforms of signals consisting from sum (a) and sequence (d) of two frequencies.

The term "wavelets" refers to a family of small waves generated from a single wave, the so-called mother wavelet, by a series of dilations and translations. To be called a "wavelet" a function should be well localized in time and frequency, and its average should be zero [Farge, 1992]. These requirements are often called "admissibility conditions" and appropriate wavelets are characterized as "admissible".

The wavelet transform $W(t, s)$ itself denotes the correlation between the original function $\psi(t)$, where $\psi(t)$ represents the perturbations (Equation 5.1) observed at a fixed location, either for a constant height or time, and the version of the mother wavelet $g(\frac{t-b}{s})$, which is scaled with a factor s and translated by a dilation b . Mathematically, the continuous wavelet transform is defined as

$$W(t, s) = \frac{1}{s} \int_{-\infty}^{+\infty} \psi(t) g^*\left(\frac{t-b}{s}\right). \quad (5.4)$$

The choice of the mother wavelet is an important point in the wavelet transform. Since the horizontal wind perturbations of the gravity waves can be considered as amplitude-modulated sine waves, the selection of the Morlet wavelet seems to be reasonable, because the Morlet wavelet is nothing else than the plane wave modulated by a Gaussian function (Figure 5.4a). Its representations in time, $g(t)$, and Fourier space, $G(\omega)$, are given by

$$g_{morlet}(t) = \pi^{-1/4} e^{i\omega_0 t} e^{-t^2/2}, \quad (5.5)$$

$$G_{morlet}(s\omega) = \pi^{-1/4} H(\omega) e^{-(s\omega - \omega_0)^2/2}, \quad (5.6)$$

where ω_0 is the order of the wavelet, $H(\omega)$ is a Heaviside step function, which is equal to 1 if $\omega > 0$ and $H(\omega) = 0$ otherwise, and s is wavelet scale.

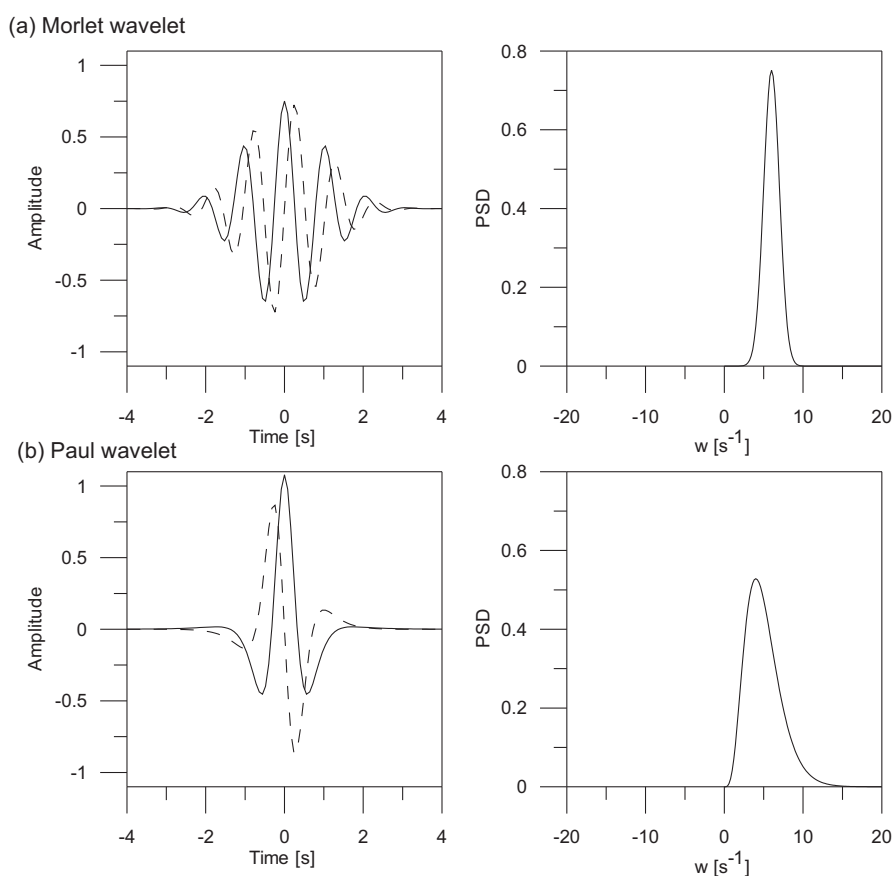


Figure 5.4: Left: real part (solid) and imaginary part (dashed) for the wavelets in the time domain. Right: corresponding wavelets in the frequency domain. The scale s was chosen to be 1. (a) - Morlet wavelet ($\omega_0 = 6$), (b) - Paul wavelet ($\omega_0 = 4$).

Using the convolution theorem, the wavelet transform (Equation 5.4) can also be expressed in Fourier space as inverse Fourier transform of the product:

$$W(t, s) = F^{-1} (G^*(s\omega)F(\omega)), \quad (5.7)$$

where $F(\omega)$ is the Fourier transform of the signal, and $G^*(s\omega)$ is the conjugated Fourier transform of the scaled wavelet. The block-scheme of the wavelet transform for vertical profiles of horizontal winds is presented in Figure 5.5.

Figure 5.5(a) shows a measured vertical profile of zonal wind, which is then extended up to 64 points (Figure 5.5b). Then the Fourier spectrum of the signal (Figure 5.5c) is multiplied by the spectra of the Morlet wavelet with different scales s (Equation 5.7). Figure 5.5(d) and (e) show an example of Morlet wavelet spectrum and the result of spectra multiplication for the scale s corresponding to the vertical wavelength 4 km. Finally, after the inverse Fourier transform the wavelet spectrum (Figure 5.5f) is estimated representing the frequency content of the vertical profile in dependence from height.

Wavelet transforms have been applied to time series of the zonal and meridional winds for constant height ranges as well as on wind profiles versus height for fixed time intervals.

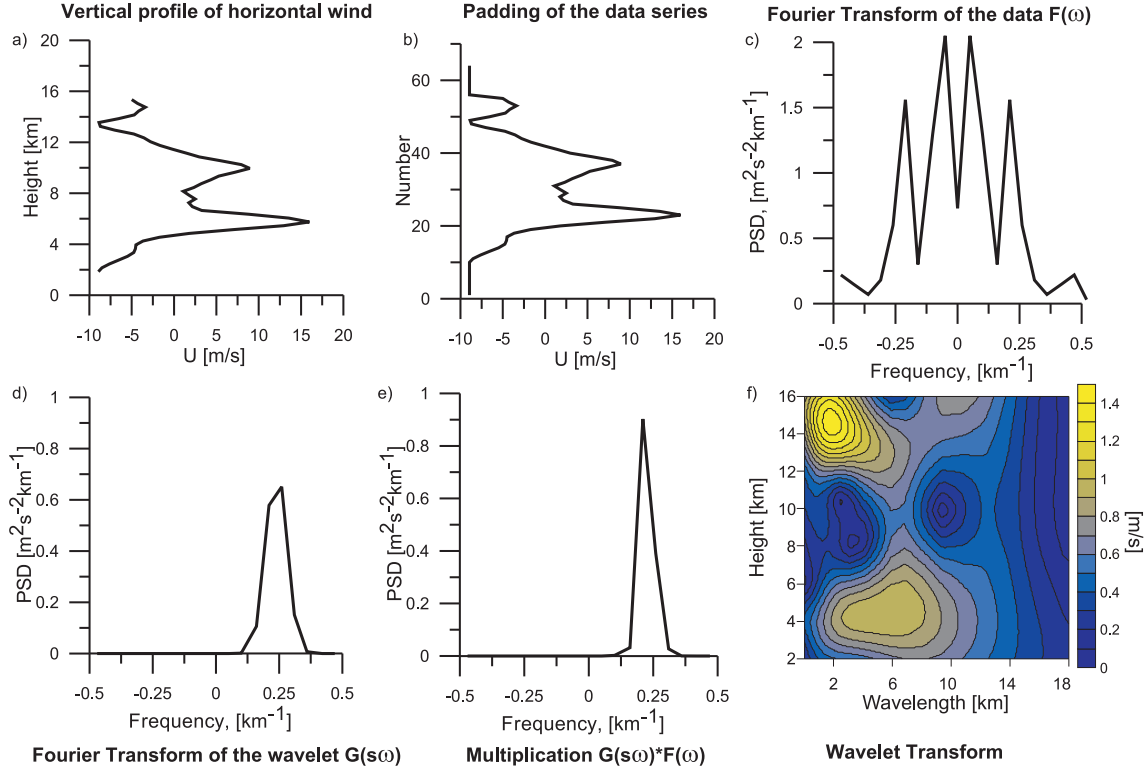


Figure 5.5: Block-scheme of the wavelet transform applied on vertical profiles of horizontal winds to get an information on dominant vertical wavelengths.

The significance of the results depends on the mother wavelet and the sample length, which is reduced at the boundaries of the time and height intervals, respectively [Torrence and Compo, 1998]. To minimize such boundary effects, we decided to apply the Paul wavelet (Figure 5.4b) with the order of 4 on the vertical profiles of horizontal winds due to their short record lengths:

$$g_{paul}(t) = \frac{2^{\omega_0} i^{\omega_0} \omega_0!}{\sqrt{\pi} (2\omega_0)!} (1 - it)^{-(\omega_0+1)}, \quad (5.8)$$

$$G_{paul}(s\omega) = \frac{2^{\omega_0}}{\sqrt{\omega_0(2\omega_0 - 1)!}} H(\omega) (s\omega)^{\omega_0} e^{-s\omega}, \quad (5.9)$$

where ω_0 is the order taken to be 4 to make the wavelet admissible. This wavelet leads to a better height localization of the dominant vertical wavelengths and smaller influences of the boundary effects, as shown by Torrence and Compo [1998]. For the wavelet transforms of time series for constant heights, the Morlet wavelet (with the order of $\omega_0 = 6$ due to the admissibility condition) has been applied resulting in an accurate frequency localization of the dominant observed periods. With the Morlet wavelet, the influence of limited data on the boundaries are larger in comparison with the Paul wavelet. However, with continuous radar measurements there are no problems to extend the time series. Details of the choice of the wavelet function can be found in Torrence and Compo [1998].

Because most of the wavelet functions are complex, the wavelet transform $W(t, s)$ is also complex, therefore the wavelet power spectrum is defined as $|W(t, s)|^2$. The wavelet scale s does not directly correspond to a Fourier wavelength λ . The relationship between the Fourier

period and the equivalent wavelet scale can analytically be derived by substituting a cosine wave of a known frequency into Equation 5.7 and calculating at which scale s the wavelet power spectrum has a maximum. For the Morlet wavelet with $\omega_0 = 6$, this leads to a value of $\lambda = 1.03s$ and for the Paul wavelet of the order 4 this leads to a value of $\lambda = 1.39s$ [Torrence and Compo, 1998]. Using Equation 5.7 one can calculate the continuous wavelet transform for different scales s at all time points simultaneously to estimate efficiently the dependence of dominant periods on the time.

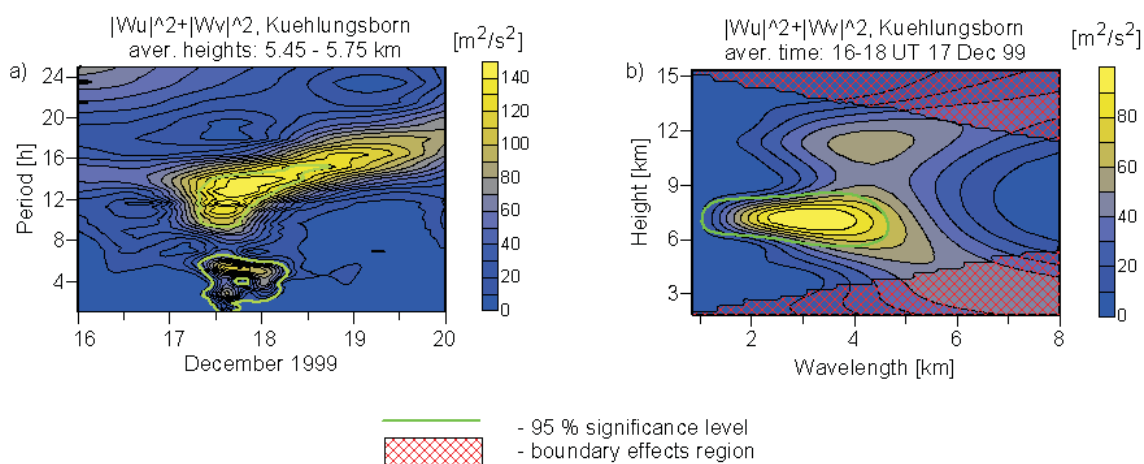


Figure 5.6: The sum of wavelet spectra applied to the zonal and meridional winds. The left panel (a) shows the wavelet transform of time series averaged over the altitude range from 5.45 to 5.75 km. The right panel (b) shows the wavelet transform applied to vertical profiles of horizontal winds averaged in time. (After *Serafimovich et al.* [2005]).

The results of the wavelet analysis applied on the wind time series and vertical profiles of horizontal winds are presented in Figure 5.6 by the sum of wavelet power spectra of the zonal and meridional wind components measured with OSWIN VHF radar at K uhlungsborn. From the wavelet transform of the wind time series averaged in height from 5.45 km to 5.75 km, shown in Figure 5.6(a), we detect the wave events with significant periods of about 12 h and 6 h on December, 17th. Furthermore, we find significant waves with vertical wavelength in the order of 2 - 4 km near the tropopause region from the wavelet transforms of vertical wind profiles averaged in time (Figure 5.6b). However, we cannot resolve vertical wavelengths larger than ~ 8 km due to the used vertical resolution and the record length available with the radar experiments. Figure 5.6 shows only the application of the wavelet transform. More detailed analyses and physical meaning are described in Section 7.1.2.

5.3 Improved bandpass filtering with a Fourier technique

Application of wavelet analysis gives clearer insight to the frequency content of the measured data. Usage of the additional information from wavelet transform assists to improve a FFT filtering routine by a more accurate definition of the frequency band.

Evaluating information from the wavelet transform, suitable filter parameters are defined for different time and height ranges to identify the waves with distinct periods. Band-pass filtering has been carried out using the Fast Fourier transform to extract the signals with dominant frequencies. Considering the case shown in Figure 5.6, one filter was constructed with a bandwidth of 8 - 18 h in the time and 2 - 4.5 km in the height domain to study the

waves with dominant observed periods of about 12 h.

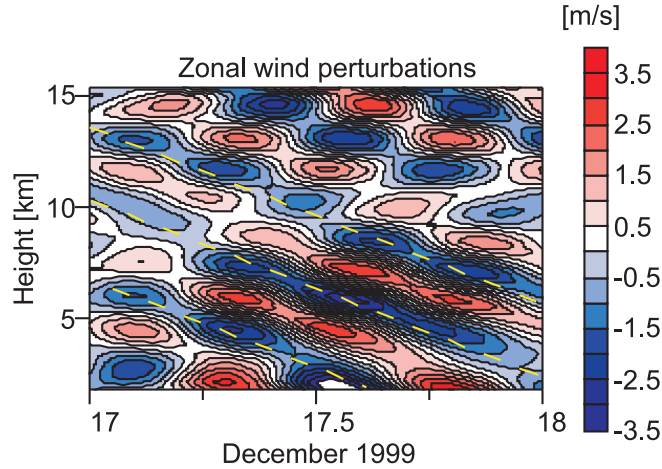


Figure 5.7: Zonal wind perturbations at Kühlungsborn on 17 December 1999 after band pass filtering with bandwidths of 8-18 h in time and 2-4.5 km in height (After *Serafimovich et al.* [2005]).

The resulting perturbations of the zonal winds at Kühlungsborn are shown in Figure 5.7. From Equation 5.1, the dashed lines indicate constant phases of the dominant wind perturbations

$$mz - \omega_{ob}t = const. \quad (5.10)$$

The vertical and temporal distances between the phase lines correspond to the vertical wavelength and the observed main period, respectively. The results confirm the information from the wavelet transform as shown in Figure 5.6 with dominant periods of ~ 12 h in the troposphere and vertical wavelengths of ~ 3.2 km. For the analysis of those waves with periods smaller than 10 h the filter with a bandwidth of 2 - 8 h in the time and 2 - 4.5 km in the height was applied.

These results and further details to estimate gravity wave parameters are described in Section 7.1.

5.4 Down- and upward directed ground-based phase propagation

One particular property of gravity waves are different signs of the intrinsic vertical phase speed and of the intrinsic vertical group velocity. This is not always true for the ground-based vertical phase velocity because in some cases the Doppler-shift between ω_{ob} and $\hat{\omega}$ (Equation 2.9) leads to a negative ground-based frequency ω_{ob} , so that in this case the ground-based vertical phase propagation has the same sign as the energy propagation of the wave packet. In order to identify a gravity wave source region, not only the phase velocity but also a group velocity has to be analyzed. As shown by [*Kuo et al.*, 2003], upward and downward energy propagating waves with the same frequency may be created simultaneously in the same place leading to a presence of multiple waves with upward and downward phase velocities. The separation of these waves is achieved by filtering of the negative and positive

parts of spectra and allows us to examine which waves are prevailing. In combination with knowledge about the sign of ω_{ob} we are able then to estimate the dominant direction of energy propagation.

The ground-based vertical phase velocity of a gravity wave is determined as $v_{pz} = \omega_{ob}/m$. It means that downward phase propagating waves have either a negative observed frequency $\omega_{ob} < 0$ and positive vertical wavenumber m or a positive observed frequency and negative vertical wavenumber. For upward phase propagating waves observed frequency and vertical wavenumber have the same signs. Thus, by application of two-dimensional filters which select between positive and negative frequencies the separation of the wave with opposite phase propagation is achieved.

Figure 5.8 presents schematically the bandpass filters applied to the wind field with cutoff frequencies of $2\pi/18 h$ and $2\pi/8 h$ and vertical cutoff wavenumbers of $2\pi/4.5 km$ and $2\pi/2 km$. The shaded areas in the four quadrants present the vertical and temporal scales that are passed by the filter.

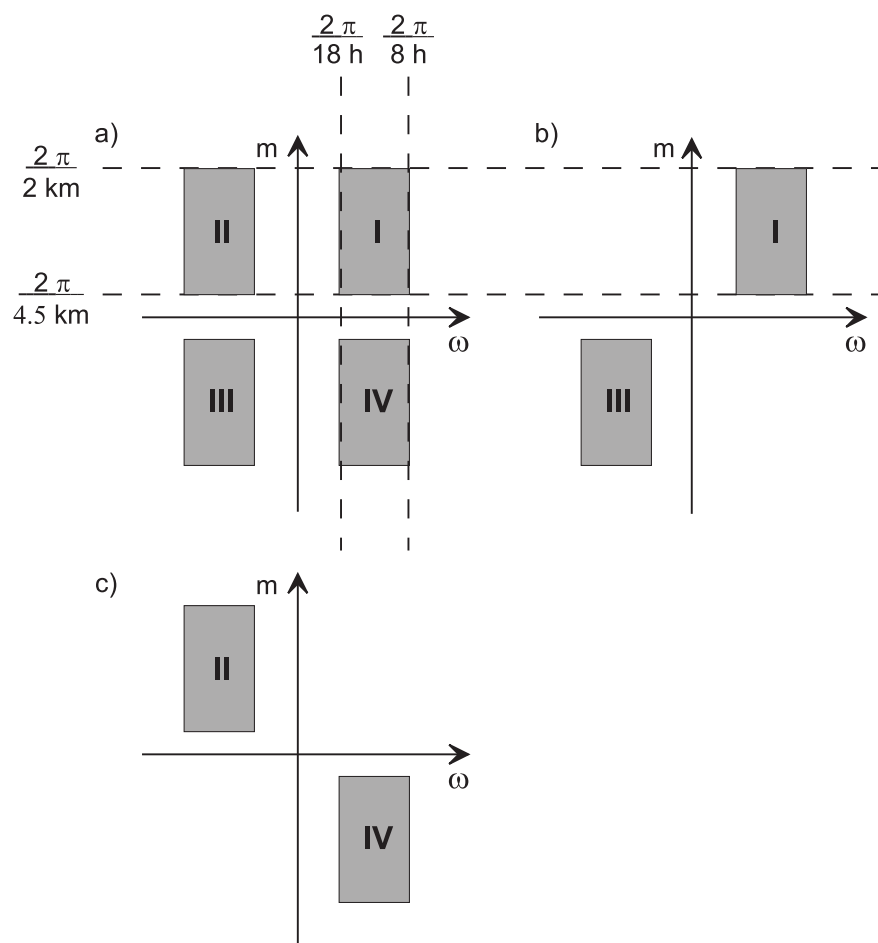


Figure 5.8: Schematic illustration of several bandpass filters in the frequency-wavenumber domain. The filter bands are 8–18 h in time and 2–4.5 km in height. The filters select upward and downward (a), only upward (b), and downward (c) phase propagating waves. (After Zink [2000]).

The separation is achieved by application of band pass filtering with Fourier analysis described in Section 5.1. For example, if we apply filtering in time and height domains with the following

reconstruction of positive parts of the spectrum only, we will have a wave with the upward phase propagation (Figure 5.8b, quadrant I). On the other hand, if we reconstruct the part of the spectra with positive ω and negative m (Figure 5.8c, quadrant IV) we will have a wave with the downward phase propagation.

For example, in Figure 5.8(a) all positive and negative frequencies are filtered, resulting in zonal wind perturbations with downward and upward phase propagation (Figure 5.9a). In Figure 5.8(b) only positive or only negative observed frequencies and vertical wavenumbers are filtered, resulting in wind perturbations with upward phase propagation (Figure 5.9b). The downward phase propagating waves (Figure 5.9c) are estimated by application of a filter selecting waves with either positive ω_{ob} and negative m or negative ω_{ob} and positive m (Figure 5.8c).

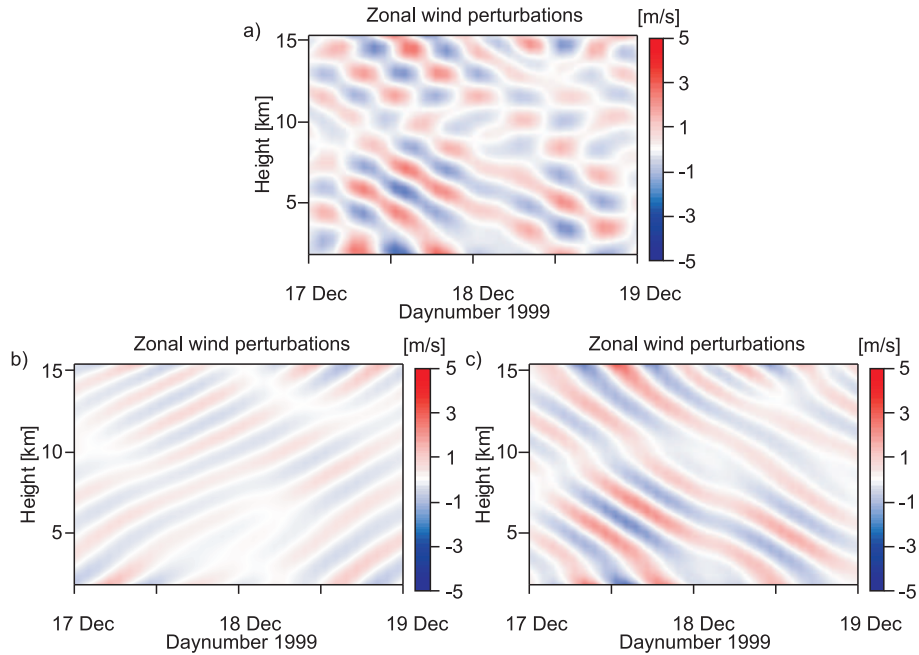


Figure 5.9: Zonal perturbation velocity fields. The time filter band is between 8-18 h, and height filter band is between 2-4.5 km. Figure on the top (a) corresponds to the waves with the downward and upward directed ground-based phase propagation. Left figure (b) corresponds to the waves with upward directed ground-based phase propagation only. Right figure (c) corresponds to the waves with the downward directed ground-based phase propagation.

Figure 5.9 shows clear wave packages on 17-18 December and the domination of downward phase propagating waves. The amplitudes of these waves (~ 3.7 m/s) are larger than amplitudes of the waves with upward directed ground-based phase propagation (~ 2 m/s). If the sign of ω_{ob} is negative downward energy propagation will dominate, and vice versa if the sign of ω_{ob} is positive upward energy propagating waves will prevail.

5.5 Bispectral analysis

Various observational results [Rüster, 1992; Clark and Bergin, 1997] and theoretical studies [Vial and Forbes, 1989; Teitelbaum et al., 1989; Teitelbaum and Vial, 1991] show the importance of nonlinear wave interactions in the atmosphere resulting in generation of secondary waves. The radar measurements sometimes show considerable temporal variations in the

amplitude and phase of long waves together with the presence of other shorter period waves [Rüster, 1994b]. Possible sources for these shorter waves are convection, frontal activity or nonlinear interactions between different components. In order to examine the role of nonlinear wave-wave interactions as a source for secondary waves, higher-order spectra are used. Special cases of higher-order spectra are bispectra and trispectra which are based on third and fourth-order Fourier transform. In this light, the power spectrum can be interpreted as second-order spectrum.

The mathematical and statistical basis of bispectral analysis has been reviewed by a number of authors (*Hinich and Clay* [1968]; *Nikias and Petropulu* [1993]). The bispectrum is an average of the product of three spectral components and reveals information on the phase coherence of three components. In particular, the bispectrum looks on the phase relationships of all sets of three frequencies where the sum of two frequencies yields the third frequency. The bispectrum has a non-zero result only if the three frequencies are phase coupled. This is described as quadratic coupling and expected to occur when a given component is the product of two other components [Clark and Bergin, 1997].

Here, a short description of the algorithm to detect phase coupling is presented. The bispectrum is, by definition, the 2-D Fourier transform of a third-order cumulant and can be divided into the indirect and direct classes [Beard et al., 1999]. Both classes require that the data are segmented. The indirect class estimates the third-order cumulants within data segments, averaging these and taking 2-D FFT [Kim and Powers, 1978]. In this thesis we used the direct class of bispectra. Here a mean of each segment is calculated and removed, then the 2-D FFT is taken first. The bispectrum $B(\omega_1, \omega_2)$ of the k th segment is calculated as

$$B(\omega_1, \omega_2) = \Psi_k(\omega_1)\Psi_k(\omega_2)\Psi_k^*(\omega_1 + \omega_2), \quad (5.11)$$

where Ψ_k is Fourier transform of the k^{th} segment. The bispectral estimates are then averaged across all segments [Beard et al., 1999].

The bispectrum estimator, $B(\omega_1, \omega_2)$, has high variance and it is desirable to have a large number of segments to smooth the results. However, this reduces the number of data points in each segment, and hence, lowering the frequency resolution of this technique.

Consider a signal, $\psi(t)$, consisting of two cosine waves

$$\psi(t) = a_{01} \cos(\omega_1 t + \phi_1) + a_{02} \cos(\omega_2 t + \phi_2), \quad (5.12)$$

where a_{0i} , ω_i and ϕ_i denote the amplitudes, angular frequency and phase of the i th signal, respectively. Let this signal pass through the quadratic system:

$$\psi'(t) = \psi(t) + K\psi^2(t), \quad (5.13)$$

where K is a constant. The output of the system is:

$$\begin{aligned} \psi'(t) = & a_{01} \cos(\omega_1 t + \phi_1) + a_{02} \cos(\omega_2 t + \phi_2) + 0.5K[a_{01}^2(1 + \cos 2(\omega_1 t + \phi_1)) + \\ & + a_{02}^2(1 + \cos 2(\omega_2 t + \phi_2)) + 2a_{01}a_{02}(\cos((\omega_1 + \omega_2)t + (\phi_1 + \phi_2)) + \\ & + \cos((\omega_1 - \omega_2)t + (\phi_1 - \phi_2)))] \end{aligned} \quad (5.14)$$

The signal $\psi'(t)$ contains cosinusoidal terms in (ω_1, ϕ_1) , (ω_2, ϕ_2) , $(2\omega_1, 2\phi_1)$, $(2\omega_2, 2\phi_2)$, $(\omega_1 + \omega_2, \phi_1 + \phi_2)$ and $(\omega_1 - \omega_2, \phi_1 - \phi_2)$. The system which produces such a phase relationship,

in other words a quadratic phase coupling (QPC), indicates a nonlinear interaction between primary signals [Beard *et al.*, 1999].

The simplest example of quadratic phase coupling showing nonlinear mixing is a signal which has components at two frequencies $f_1 = 0.1 \text{ h}^{-1}$ ($T_{ob}^1 = 10 \text{ h}$) and $f_2 \approx 0.4 \text{ h}^{-1}$ ($T_{ob}^2 = 24 \text{ h}$) and another at the sum of those two frequencies $f_3 = f_1 + f_2 = 0.14 \text{ h}^{-1}$ ($T_{ob}^3 \approx 7 \text{ h}$) with corresponding phases $\phi_1 = \pi/4$, $\phi_2 = 2\pi/3$ and $\phi_3 = \phi_1 + \phi_2 = 11\pi/2$:

$$\Psi(t) = 5 \cos(2\pi f_1 t + \phi_1) + 5 \cos(2\pi f_2 t + \phi_2) + 5 \cos(2\pi f_3 t + \phi_3) \quad (5.15)$$

Figure 5.10 shows the bispectrum of the simulated signal (Equation 5.15).

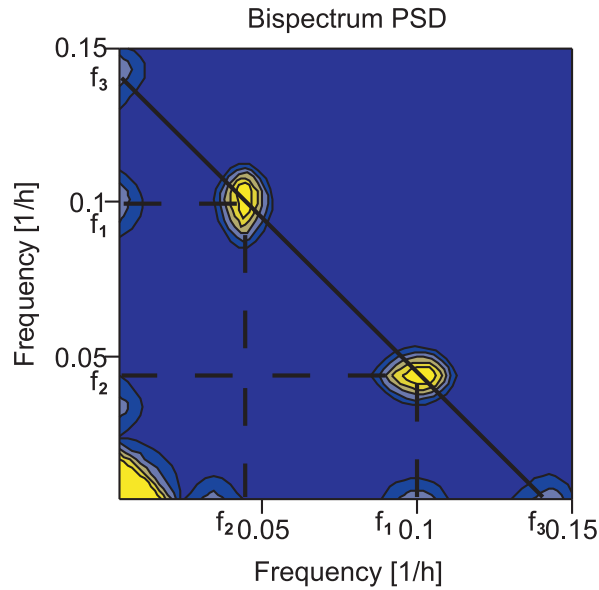


Figure 5.10: Bispectrum power spectral density of simulated signal $\Psi(t)$.

In absence of wave-wave interactions we would see flat spectrum without any peaks. However, the spectrum reveals the coupling between waves with frequencies f_1 and f_2 with resulting secondary waves with frequency f_3 by the peaks with coordinates (f_1, f_2) and (f_2, f_1) .

In general, the interpretation of any bispectrum follows this procedure: the peaks are symmetrically relative to the diagonal, therefore two peaks occur. The peak coordinates correspond to the frequencies involved in quadratic phase coupling. The resulting third frequency is located geometrically by the line connecting symmetrical peaks in the spectrum.

The application of the bispectral analysis to radar measurements for investigation of possible nonlinear interactions between waves and generation of secondary wave is presented in Section 7.1.3.

In summary to this chapter, filter routines have to be applied using the Fourier analysis in time and height domains for estimation of wind disturbances. By the application of the wavelet analysis, additional information on the spatial localization of gravity waves as well as on their incidence and duration are excellently resolved. To get additional information on the direction of the phase propagation, a filtering procedure to separate wind perturbations into downward and upward phase propagating waves has been applied. Finally, the bispectral analysis is presented as a tool for the investigation of nonlinear wave-wave interactions to detect generated secondary waves.

Chapter 6

Methods for investigation of gravity waves

For extracting gravity wave parameters, three methods have commonly been used. In this Chapter, we will describe their basic ideas including their strengths and weaknesses. The first one is the rotary spectrum, which was applied to atmospheric IGWs by *Thompson* [1978]. The calculation of the rotary spectrum allows directly to estimate the vertical direction of energy propagation. The next method, the hodograph analysis, is a standard tool in meteorology, described by *Gill* [1982] in connection with a rotating fluid and applied first to IGWs by *Cot and Barat* [1986]. The hodograph technique gives wave description in more detail. But this method is only a snapshot and applicable for monochromatic waves. In addition, *Vincent and Fritts* [1987] presented a Stokes-parameter method which results in a set of gravity wave parameters comparable to those of the hodograph analysis, but with the possibility to average over duration of the wave and selected wavenumbers bands.

Cho [1995] developed a cross-spectral technique, which allows to estimate coherence and phase difference between zonal and meridional winds in a spectral bin. It combines the advantages of the rotary and hodograph methods. As shown by *Eckermann* [1996], cross-spectrum is in principle a spectral analogue of the Stokes-parameter analysis.

To estimate horizontal wavelengths of the gravity waves, we will describe a method based on combined radar and radiosonde measurements [*Peters et al.*, 2003].

Furthermore, we will discuss another method to derive horizontal wavelengths of gravity waves which consists in the direct solution of the dispersion and Doppler equation and requires the solution of a second-order polynomial.

Ecklund et al. [1985] and *Carter et al.* [1989] showed the ability to determine atmospheric wave parameters in the troposphere and stratosphere using the cross-spectral analysis of vertical winds from three closely spaced vertical clear-air radars. Inspired by their work, we will introduce a cross-spectral analysis applicable to zonal and meridional winds measured by two collocated radars separated by ~ 250 km for the investigation of common waves, their horizontal wavelengths and phase velocities and their temporal and spatial differences [*Serafimovich et al.*, 2005].

Finally, we will consider direct measurements of wave momentum fluxes developed by *Vincent and Reid* [1983] and applied to atmospheric radars. Results obtained with these algorithms are presented in Chapter 7.

6.1 Rotary spectra

The rotary spectrum technique quantifies how energy is partitioned between upward- and downward-propagating gravity waves. The rotary spectrum is calculated by the Fourier transform of the complex velocity vector $u'(z)+iv'(z)$ and leads to an asymmetrical function. Following *Thompson* [1978] and *Guest et al.* [2000], this method allows to detect the rotation direction of the horizontal wind perturbations with height using the difference of the negative and positive parts of the spectrum which indicate the presence of a gravity wave in the measurements. The clockwise (counterclockwise) rotating waves there are associated with negative (positive) frequencies in the rotary power spectrum.

In the northern hemisphere the clockwise and counterclockwise rotations of horizontal wind perturbations with a height indicate the upward and downward vertical direction of gravity wave energy propagation, respectively.

To illustrate the ability of this method, we constructed three artificial signals and applied the FFT on the corresponding complex series. The results (Figure 6.2) are discussed in connection with the hodograph technique (see following Section 6.2). The application of the rotary spectra method during selected measuring campaigns is shown in Chapter 7.

6.2 Hodograph analysis

The estimation of the intrinsic frequency of gravity waves $\hat{\omega}$ can also be done with the hodograph analysis, which is a standard tool in meteorology. The idea of hodograph analysis is to trace the course of the deviation of the horizontal wind vector with respect to height. If enough points are taken to span one wavelength of a gravity wave, then an ellipse can be fitted. For inertia-gravity waves, linear theory without any wind shear effects [*Gill*, 1982] predicts

$$v' = -i \cdot u' \cdot \frac{f_c}{\hat{\omega}}, \quad (6.1)$$

where u' and v' are the zonal and meridional components of the horizontal perturbation wind profiles, f_c is the Coriolis frequency and $\hat{\omega}$ is the intrinsic frequency of the wave.

By the application of the hodograph one can extract the following parameters:

- the vertical sense of inertia-gravity wave propagation from the rotational sense;
- the direction of the horizontal wave propagation that is parallel to the major axis of the ellipse;
- vertical wavelength L_z ;
- the intrinsic frequency $\hat{\omega}$ from the ratio of the major to the minor axis of the ellipse, Equation 6.1.

An example of the hodograph derived from radar measurements in the mesosphere is shown in Figure 6.1 indicating the presence of an upward propagating gravity wave with an intrinsic period $T_{in}=4.5$ hours, vertical wavelength $L_z \approx 4$ km, and a horizontal propagation direction along the dotted line. We have to note, that the estimated horizontal wave propagation is undefined by 180° . Using additional temperature information or vertical winds from radar and the polarization Equations 2.10, this ambiguity can be solved.

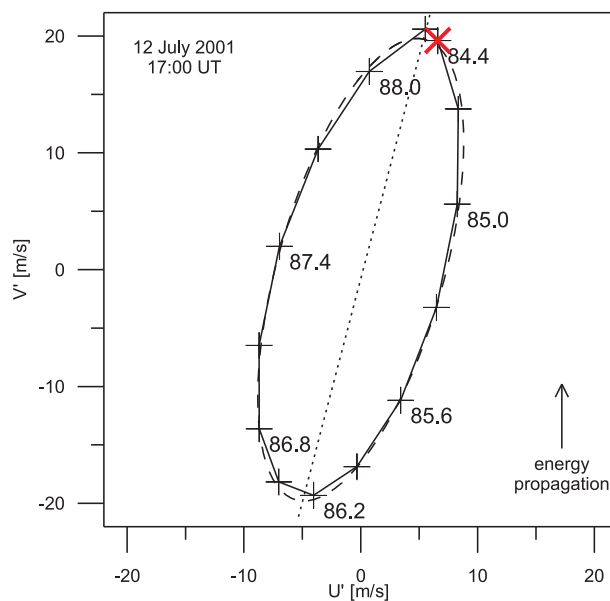


Figure 6.1: Hodograph of wind perturbations (u' , v') derived from filtered ALWIN VHF radar measurements between 84.4 and 88.3 km on 12 July 2001, at 17:00 UT (solid line - measured profiles, dashed line - fitted ellipse, **X** - starting point of the hodograph). The horizontal propagation direction of the gravity wave is parallel to the major axis (dotted line). The clockwise rotation indicates an upward propagating wave (northern hemisphere).

To compare the hodograph analysis with rotary spectra estimation, we constructed three artificial signals for zonal and meridional wind perturbations with different amplitudes (Figure 6.2).

The hodographs (Figures 6.2 a,b,c) indicate clear upward energy propagations from the clockwise rotational sense in the northern hemisphere. The rotary spectrum of a circular polarized wave (Figure 6.2 d) show a dominant peak in the negative frequency range. However, when waves have an elliptical polarization (Figures 6.2 e,f), small peaks at positive frequencies appear. In an extreme case of a nearly linear polarization (not shown here) with a large difference between amplitudes of zonal and meridional perturbations, the peaks in rotary spectrum tend to be equal, but are never exactly equal. Therefore, the sign of the difference between negative and positive parts of the rotary spectra is related to the direction of the energy propagation, i.e., the predominance of upward energy propagation over the downward propagation is connected with the prevalence of the spectra at negative frequencies.

However, the hodograph method represents an instantaneous status and the estimation of gravity wave parameters is valid only for monochromatic waves. Usually a hodograph gives variable results due to the superposition of different waves in the wind profiles. Recently, *Zhang et al.* [2004] gave a critical review on this method, especially devoted to the sensitivity of different polynomial filters used to separate the wave from a background flow, and their influence on the vertical wavelength and intrinsic frequency. One possibility to avoid such uncertain results in the gravity wave analysis is the determination of all parameters for a given wavenumber band, averaged for the duration of the wave. These ideas are successfully used in the following Stokes-parameter spectra.

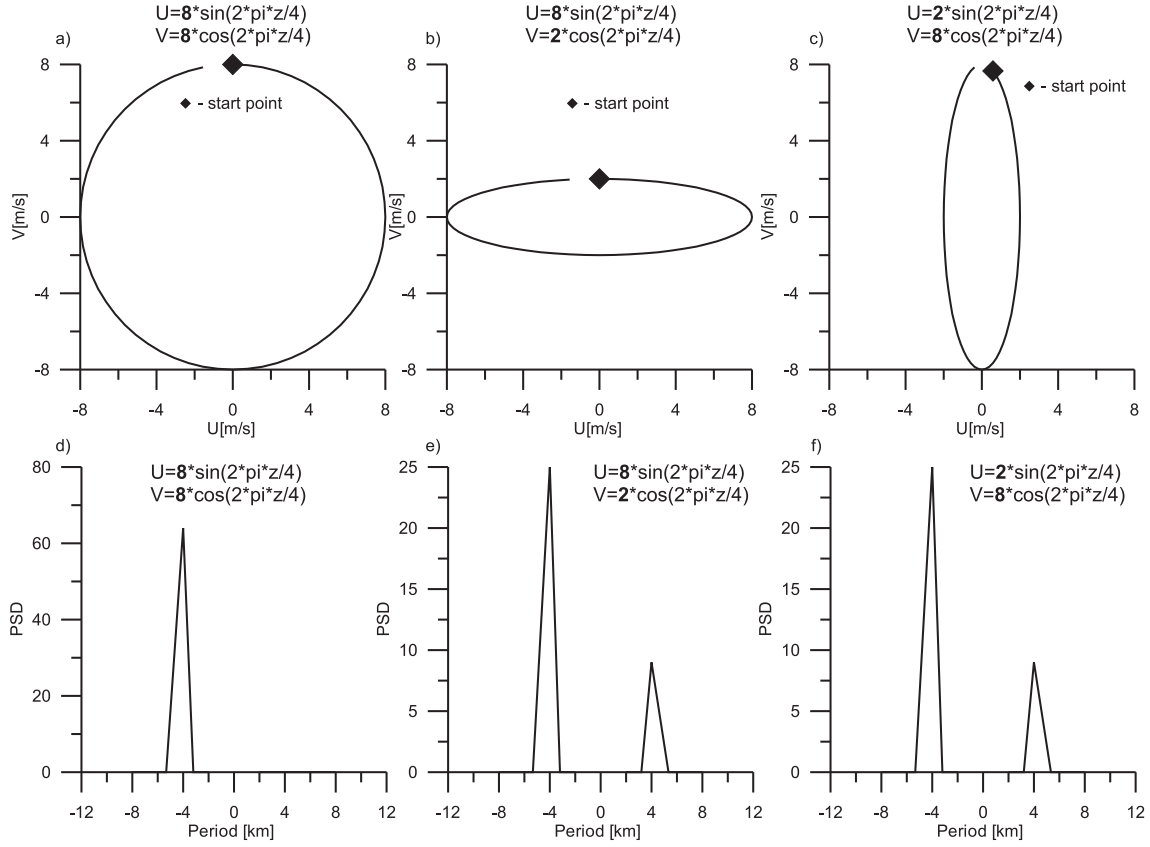


Figure 6.2: Results of the hodograph analysis (a, b, c) and corresponding rotary spectra (d, e, f) for the simulated height profiles of the zonal and meridional winds with different amplitudes corresponding to circular(a,d) and elliptical (b,c,e,f) polarized waves.

6.3 Stokes-Parameter spectra

In order to provide a more statistical description of the wave field, we use the technique, introduced by *Vincent and Fritts* [1987] and improved by *Eckermann and Vincent* [1989], in determining the so-called Stokes parameters of the gravity wave field. This method makes the analogy between partially polarized gravity waves and partially polarized electromagnetic waves, *Kraus* [1966].

The Stokes-parameter technique assumes that any given vertical profile of horizontal-velocity perturbations, $(u'(z), v'(z))$, contains a partially polarized wave field. It means that a single coherent wave of peak amplitude (\hat{u}, \hat{v}) exists within an unpolarized, isotropic, noiselike background velocity field variance $\overline{u_{noise}^2} + \overline{v_{noise}^2}$. The four Stokes parameters can then be defined as

$$I = \frac{1}{2}(\overline{\hat{u}^2} + \overline{\hat{v}^2}) + (\overline{u_{noise}^2} + \overline{v_{noise}^2}) = \overline{u'^2} + \overline{v'^2} \quad (6.2)$$

$$D = \frac{1}{2}(\overline{\hat{u}^2} - \overline{\hat{v}^2}) = \overline{u'^2} - \overline{v'^2} \quad (6.3)$$

$$P = \overline{\hat{u}\hat{v}} \cos \delta = 2\overline{u'v'} \quad (6.4)$$

$$Q = \overline{\widehat{u\widehat{v}} \sin \delta} \quad (6.5)$$

where overbars denote height and/or time averaging of the perturbation velocities; and $\delta = 0^\circ$ or 180° implies linear polarization ($Q = 0$), $\delta = 90^\circ$ or 270° implies circular polarization ($P = 0$), and anything between implies elliptical polarization. Thus P is the "in-phase" covariance associated with linear polarization, and Q is the "in quadrature" covariance associated with circular wave polarization, while I clearly quantifies the total variance or energy of gravity wave and D defines its axial anisotropy.

The analysis of profiles, which contain more than one wave, needs a decomposition of the generally polychromatic wave field. For this purpose, *Eckermann and Vincent* [1989] developed a method to calculate all Stokes parameters in the Fourier domain.

A Fourier transform of the given vertical profiles $u'(z)$ and $v'(z)$ over their full height ranges yields the following Fourier representations of the profiles:

$$U(m) = U_R(m) + iU_I(m) \quad (6.6)$$

$$V(m) = V_R(m) + iV_I(m) \quad (6.7)$$

where m is the vertical wavenumber, U_R , V_R are real parts of the spectra and U_I , V_I are imaginary parts of the spectra. From here, *Eckermann and Vincent* [1989] derived the following power spectral densities for the four Stokes parameters, based on definitions (6.2)- (6.5):

$$I(m) = K(\overline{U_R^2(m)} + \overline{U_I^2(m)} + \overline{V_R^2(m)} + \overline{V_I^2(m)}) \quad (6.8)$$

$$D(m) = K(\overline{U_R^2(m)} + \overline{U_I^2(m)} - \overline{V_R^2(m)} - \overline{V_I^2(m)}) \quad (6.9)$$

$$P(m) = 2K(\overline{U_R(m)V_R(m)} + \overline{U_I(m)V_I(m)}) \quad (6.10)$$

$$Q(m) = 2K(\overline{U_I(m)V_R(m)} + \overline{U_R(m)V_I(m)}) \quad (6.11)$$

Overbars denote averages over a number of independent spectral realizations, to remove the effects of incoherent motions, and K is constant which scales the squared Fourier terms to power spectral densities. Consequently, any Stokes parameter $X = \{I, D, P, Q\}$ can now be evaluated over the full range of heights within any wavenumber band, according to Parseval's relation

$$X_{m_1, m_2} = \int_{m_1}^{m_2} X(m) dm, \quad (6.12)$$

where X_{m_1, m_2} is one of the Stokes parameters (6.2)- (6.5) evaluated over a wavenumber band between m_1 and m_2 from corresponding power spectral density $\overline{X}(m)$. This Fourier decomposition of the Stokes parameters clearly allows for more than one coherent wave to be isolated from any given sequence of velocity profiles, as long as the various coherent waves in the profile exist within well-defined and well-separated vertical wavenumber bands.

In the Stokes-parameter analysis a coherent wave is identified through the degree of wave polarization (6.13), so that, within a wavenumber band $m_1 \leq m \leq m_2$

$$d_{m_1, m_2} = \frac{(D_{m_1, m_2}^2 + P_{m_1, m_2}^2 + Q_{m_1, m_2}^2)^{\frac{1}{2}}}{I_{m_1, m_2}} \quad (6.13)$$

The phase difference δ between zonal and meridional wind perturbations, the major axis orientation Θ , and the averaged ellipse axial ratio R are given by

$$\delta_{m_1, m_2} = \arctan\left(\frac{Q_{m_1, m_2}}{P_{m_1, m_2}}\right) \quad (6.14)$$

$$\Theta_{m_1, m_2} = \frac{1}{2} \arctan\left(\frac{P_{m_1, m_2}}{D_{m_1, m_2}}\right) \quad (6.15)$$

$$R_{m_1, m_2} = \tan \mu \quad (6.16)$$

where

$$\mu = \frac{1}{2} \arcsin\left(\frac{Q_{m_1, m_2}}{d_{m_1, m_2} \cdot I_{m_1, m_2}}\right) \quad (6.17)$$

As already mentioned in Section 6.2, the horizontal wave propagation determined by the major axis orientation Θ is uncertain by 180° without additional information of temperatures or vertical winds. Note, that the averaging time can be selected on the base of the times of maxima of total variances described by the Stokes parameter I , which characterizes the mean kinetic energy for the investigated interval and vertical wavenumber band. The most attractive feature of these parameters is that any partially polarized wave motion can be described completely and uniquely in terms of its Stokes parameters due to the averaging in time and wavenumber bands.

6.4 Combined radar and radiosonde measurements

Based on the intrinsic frequency, either obtained with the hodograph technique or by the Stokes parameters, now the horizontal wavelength of gravity waves have to be estimated.

An approved method for this task is given by a combination of continuous radar measurements with radiosonde soundings, launched every 2-3 hours and covering the height range $\sim 0-35$ km with fine vertical resolution (up to 50 m). This method has been successfully applied to investigate tropospheric/lower stratospheric inertia-gravity waves with periods in the near of the inertia or Coriolis frequency and long horizontal wavelengths [*Peters et al.*, 2003].

Here, for the estimation of the intrinsic frequency $\hat{\omega}$ and horizontal direction of wave propagation Θ , radiosonde soundings have been used. The observed frequency ω_{ob} as well as mean zonal and meridional winds are derived from continuous radar observations. Using Θ , the mean horizontal wind in direction of the wave propagation u_h is calculated. By substitution of all values to the Doppler shift relation (2.9) the horizontal wavenumber k_h can be derived:

$$k_h = \frac{\omega_{ob} - \hat{\omega}}{u_h} \quad (6.18)$$

6.5 Direct solution of basic equations

If there are no radiosondes to estimate directly the intrinsic frequency, a direct method to derive the zonal wavenumber k of the gravity wave is based on the solution of the Doppler equation 2.9 and dispersion equation 2.8. Assuming that $k^2 \ll m^2$, $l \approx 0$ and $2\pi/m \ll H_p$, then the dispersion relation (Equation 2.8) reduces to

$$\hat{\omega}^2 = f_c^2 + \frac{N^2 k^2}{m^2}. \quad (6.19)$$

By substitution the Doppler relation (2.9) to the dispersion relation (6.19), the second-order polynomial (6.20) is given by

$$k^2(\bar{u}^2 m^2 - N^2) - 2k\bar{u}\omega_{ob}m^2 + m^2(\omega_{ob}^2 - f_c^2) = 0. \quad (6.20)$$

The observed frequency ω_{ob} and vertical wavenumber m can be derived from continuous radar measurements. The last step in this method is to obtain all roots of the polynomial (6.20) by numerical methods. This method shows an appropriate result only at the time, when the background wind is constant. This idea to estimate gravity wave parameters is implemented in Section 7 taking into account the wind shear effect (see Equations 2.24 and 2.25 in Section 2.4).

6.6 Cross-spectral analysis

To investigate temporal and spatial differences of gravity waves and their horizontal wavelengths and phase velocities we applied cross-spectral analysis on zonal and meridional winds measured by two collocated radars separated by ~ 250 km. This method is extended to measurements from two or three radars.

In such a case we can investigate gravity waves as they are propagated across the radars. Horizontal parameters of propagating gravity waves (e.g., wavelength or phase velocity) can be determined by measuring the phase differences in the wind fluctuations between radars, provided that wavelength is resolved by the distance between stations.

As an example of cross-spectral analysis we consider an analysis of radar measurements from two stations: OSWIN radar in Kühlungsborn and wind profiler in Lindenberg.

First we need to separate the events of interest from undesired processes. The wavelet analysis locates the event in time and resolves it in spectral content. This location in time and frequency space enables the discrimination of various events. After detection of the events in both data sets and filtering without phase distortion, the cross spectrum (6.21) can be calculated

$$S_{U_1 U_2}(\nu) = \frac{\langle U_1(\nu) U_2^*(\nu) \rangle}{\langle |U_1(\nu)|^2 \rangle^{\frac{1}{2}} \langle |U_2(\nu)|^2 \rangle^{\frac{1}{2}}}, \quad (6.21)$$

where U_1 and U_2 are Fourier transforms of zonal wind time series measured by radars, ν is an independent variable in the frequency domain, the brackets denote the averaging in the height range. The magnitude of $S_{U_1 U_2}$ is a coherence function, which varies from 0 to 1. This gives a measure of the correlation between signals from both stations for a given spectral bin. Note that the ensemble averaging denoted by the brackets means that the cross spectrum is

smoothed, because if no smoothing is carried out, the coherence, regardless of the nature of the processes, is equal to one. The phase value $\Delta\phi$ of corresponding cross-spectrum maximum gives the time delay τ between the appearance of the wave maxima at both locations, which is given by

$$\tau = T_{ob} \frac{\Delta\phi}{360^\circ}, \quad (6.22)$$

where T_{ob} is the observed wave period. Here particular attention must be directed to avoid changes of the phases due to the application of any filtering procedures.

Usually to investigate the spatial characteristics of a wave one needs at least three points, forming a triangle. Such a method to analyze gravity waves moving across an array of surface-based meteorological atmospheric pressure sensors has been described by *Hauf et al.* [1996] and *Nappo* [2002]. We applied here the cross-spectral analysis only for a pair of the radars, however using additional information for the wave propagation directions Θ derived from the Stokes-parameter analysis at both locations and provided that they don't diverge significantly. Following the ideas of *Nappo* [2002], we consider a wave perturbation of some variable, ψ , observed at the same altitude range at each station. If we imagine a wave with constant amplitude and horizontal wave vector \vec{k}_h observed at both stations (solid and dashed blue lines on the block-scheme), then the crests or any other phase point of the wave observed at radar 1 (x_1, y_1, z_1) at the time t and at radar 2 (x_2, y_2, z_2) at the time $t + \tau$ (Figure 6.3) correspond to

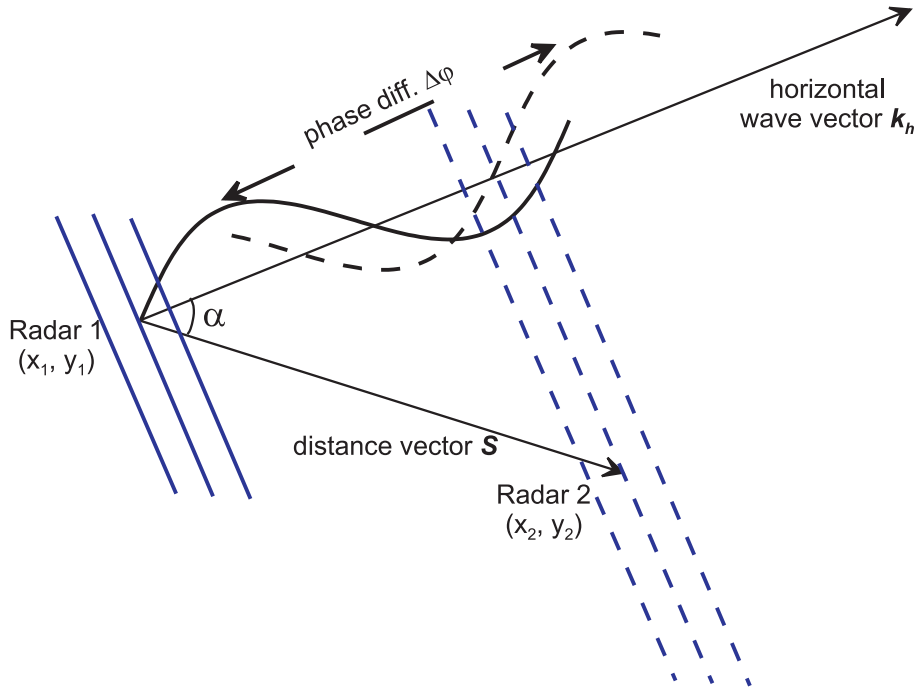


Figure 6.3: Block-scheme of the gravity wave propagation from radar 1 (solid lines) to radar 2 (dashed lines). The blue lines correspond to the wave phase fronts (After *Serafimovich et al.* [2005]).

$$\psi_1(kx_1 + ly_1 + mz_1 - \omega_{ob}t) = \psi_2(kx_2 + ly_2 + mz_2 - \omega_{ob}(t + \tau)), \quad (6.23)$$

where k , l and m are the wavenumbers in the x -, y - and z - directions, respectively. It is

assumed that the wave does not change its main characteristics propagating from radar to radar, we can write

$$kx_1 + ly_1 + mz_1 - \omega_{ob}t = kx_2 + ly_2 + mz_2 - \omega_{ob}(t + \tau), \quad (6.24)$$

which reduces to

$$k(x_2 - x_1) + l(y_2 - y_1) = \omega_{ob}\tau - m(z_2 - z_1). \quad (6.25)$$

The left-hand side of the Equation 6.25 can be written in vector form as a scalar multiplication of the vectors $\vec{k}_h \cdot \vec{S}$ or as a multiplication of the vector absolute values with $\cos \alpha$

$$|k_h||S|\cos\alpha = \omega_{ob}\tau - m(z_2 - z_1), \quad (6.26)$$

where \vec{S} is the distance vector between both radars and α is the angle between \vec{S} and the wave propagation vector \vec{k}_h . Substituting $\omega_{ob} = 2\pi/T_{ob}$, the horizontal and vertical wavenumbers k_h and m by their wavelengths $L_h = 2\pi/k_h$ and $L_z = 2\pi/m$ to Equation 6.26 we can write

$$L_h = \frac{|S|\cos\alpha}{\tau/T_{ob} - (z_2 - z_1)/L_z}. \quad (6.27)$$

Using the distance between both radars $|S|$ and the time delay τ between gravity wave events one can estimate the ground-based horizontal phase velocity of the wave propagation v_{ph}

$$v_{ph} = \frac{|S|\cos\alpha}{\tau - (z_2 - z_1)T_{ob}/L_z}. \quad (6.28)$$

Since the cross-spectral analysis yields the dominant observed frequency ω_{ob} , then the ground-based horizontal phase velocity v_{ph} corresponds to the term ω_{ob}/k .

In order to apply Equations 6.27-6.28, the radar coordinates and the direction of the wave propagation as estimated by the Stokes-parameter analysis have been used to estimate the angle α . Note that the directions of the wave propagation at both locations should be comparable so that there are no ambiguities to estimate α and to apply the cross-spectral analysis.

6.7 Gravity waves and Momentum Fluxes

As shown in Section 2.3, gravity waves transport momentum from energy sources. These processes are characterized by the momentum fluxes. Ground based radars have the advantage to measure wave momentum fluxes directly [Vincent and Reid, 1983]. This method requires the comparison of the Doppler shifts in backscattered radar echoes from the atmosphere, using two or more narrow beams tilted with a small angle from the vertical direction.

Consider two radar beams pointed at equal and opposite angles θ to the zenith, and the beams are arranged in the zonal direction (Figure 6.4). Because of the motion of the irregularities, the echoes will be Doppler shifted by an amount proportional to the wind component along a given beam direction.

Considering small-scale motions, the instantaneous Doppler velocity $v(\theta, R_0, t)$ measured at the height R_0 along the positive θ pointing beam can be written as

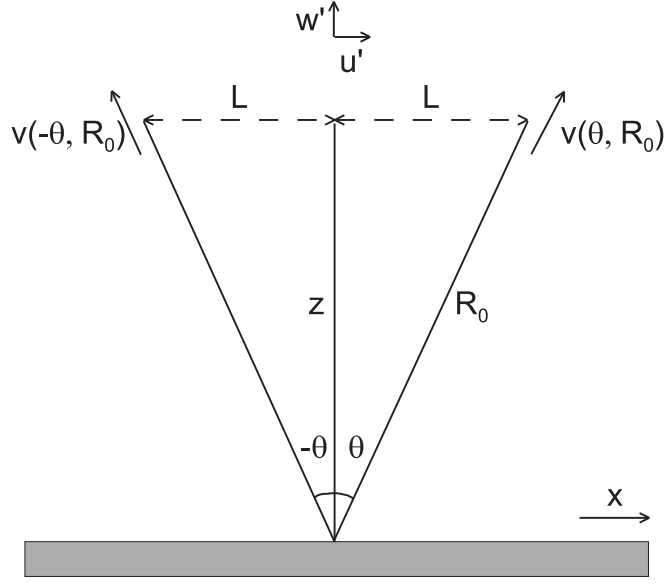


Figure 6.4: Schematic representation of the two dimensional radar situation, in which two narrow radar beams are directed at angles θ and $-\theta$ to the zenith. (After *Vincent and Reid* [1983]).

$$v(\theta, R_0, t) = w'(\theta, R_0, t) \cos \theta + u'(\theta, R_0, t) \sin \theta. \quad (6.29)$$

Similarly, the Doppler velocity measured along the complementary beam at $-\theta$ is

$$v(-\theta, R_0, t) = w'(-\theta, R_0, t) \cos \theta - u'(-\theta, R_0, t) \sin \theta. \quad (6.30)$$

If overbars denote the time average, then

$$\overline{v^2(\theta, R_0)} = \overline{w'^2(\theta, R_0)} \cos^2 \theta + \overline{u'^2(\theta, R_0)} \sin^2 \theta + 2\overline{u'w'(\theta, R_0)} \sin \theta \cos \theta, \quad (6.31)$$

$$\overline{v^2(-\theta, R_0)} = \overline{w'^2(-\theta, R_0)} \cos^2 \theta + \overline{u'^2(-\theta, R_0)} \sin^2 \theta - 2\overline{u'w'(-\theta, R_0)} \sin \theta \cos \theta. \quad (6.32)$$

If the statistics of the motions are assumed to be independent of the horizontal position, then

$$\left. \begin{aligned} \overline{u'^2(\theta, R_0)} &= \overline{u'^2(-\theta, R_0)} = \overline{u'^2(z)} \\ \overline{w'^2(\theta, R_0)} &= \overline{w'^2(-\theta, R_0)} = \overline{w'^2(z)} \\ \overline{u'w'(\theta, R_0)} &= \overline{u'w'(-\theta, R_0)} = \overline{u'w'(z)} \end{aligned} \right\}, \quad (6.33)$$

where $z = R_0 \cos \theta$. These seem to be reasonable assumptions for propagating waves for the horizontal separation which we are considering here. Subtracting 6.32 from 6.31 gives

$$\overline{v^2(\theta, R_0)} - \overline{v^2(-\theta, R_0)} = 4\overline{u'w'} \sin \theta \cos \theta, \quad (6.34)$$

or

$$\overline{u'w'}(z) = \frac{\overline{v^2(\theta, R_0)} - \overline{v^2(-\theta, R_0)}}{2 \sin 2\theta}. \quad (6.35)$$

By estimation of the mean-square Doppler velocities at a number of successive ranges, it is possible to measure the vertical profile of the vertical flux of the zonal momentum. The vertical flux of the meridional momentum can be derived by using the Doppler velocities from the N-S pointed beams.

The measured momentum fluxes are thought to be due to the action of waves with different frequencies. It is therefore instructive to obtain momentum flux values for various frequency or period ranges. The method of separating the contributions from different frequencies is suggested by *Fritts and Vincent* [1987]. The lower limit of each period range was set by averaging the data. For example, averaging of data for 4 hours gives a lower limit of 8 hours. The upper limit is defined by the length of the data block used for the analysis.

The Vincent-Reid method described above involves the difference between two quantities which are similar in magnitude. The quantities that are being subtracted are variances and these are susceptible to the effects of outliers. If a bad data point occurs and lies some distance r from the line of best fit, its contribution to the variance sum r^2 , could easily dominate the contributions of the good data points. It is therefore important to remove the outliers from the data.

In conclusion, methods described here supplement each other and allow to estimate the main characteristics of gravity waves like horizontal and vertical wavelengths, the direction and velocities of wave (energy) propagation, observed and intrinsic frequencies of waves, vertical fluxes and mean-flow accelerations. The combination of methods gives the ability for more detailed analysis of gravity waves propagating from their sources in the troposphere to the lower thermosphere, resulting in a better understanding of general structure and dynamics of the atmosphere.

Chapter 7

IGWs observed with collocated radars

Based on the methods described in the previous Chapters, here the results of case studies are presented, obtained mainly during two campaigns carried out in Northern Germany without large orography and in Northern Scandinavia with an additional influence of orographically induced mountain waves. In both campaigns, the data of measurements with collocated radars separated by about 250 km have been used. First the data from each radar are analyzed independently and the main gravity wave parameters are estimated. The detailed analyses of the data, including the comparison with MM5 model simulations and momentum flux estimations are then compared with results derived by a cross-spectral analysis using combined measurements to identify common waves over a distance of about 250 km, to estimate their horizontal wavelengths and phase velocities, and to investigate their temporal and spatial differences. Additionally, an evidence for the generation of a secondary wave due to nonlinear wave-wave interaction has been provided by the bispectral analysis.

7.1 Northern Germany: A case study

The dynamics, transport and exchange in the tropopause region are determined partially by propagating Rossby waves which are observed in the upper troposphere and lower stratosphere of mid-latitudes. Rossby wave breaking events in regions of weak wind flow can be classified in 4 types [*Peters and Waugh, 1996*]: equatorward upstream (LC1) and downstream (LC2); poleward upstream (P1) and downstream (P2). During a life cycle of a Rossby wave, inertia-gravity waves with relatively long horizontal wavelengths can be generated [*O'Sullivan and Dunkerton, 1995*]. They can propagate regionally both horizontally and vertically and can play an essential role in interaction processes between the upper troposphere and the lower stratosphere. Therefore, the study of forcing mechanisms and propagation of inertia-gravity waves in connection with breaking Rossby waves is important.

To investigate the appearance of long period inertia-gravity waves in connection with a jet stream in the upper troposphere during a Rossby wave breaking event, a first field campaign has been carried out at Kühlungsborn from 17-19 December 1999 in the frame of the LEWIZ project. This project is described in details in *Peters et al. [2003]* and *Peters et al. [2004]*. First results were based on a series of 17 radiosondes released every 3 h supported by VHF radar observations at the same location [*Peters et al., 2003*]. It has been found that the source of the dominating inertia-gravity wave with a period of about 12 h is placed in the region

of the zonal wind jet just below the tropopause. In extension to this, the main objectives of a following continuative study presented here, are to get more insight into the structure of gravity waves including of those with shorter periods in the upper troposphere which cannot be resolved by 3-hourly radiosondes. These investigations are done with detailed analyses of the data of the OSWIN-53.5 MHz-VHF radar located at Kühlungsborn, and the 482 MHz-wind profiler at Lindenberg, separated by about 265 km.

7.1.1 Observations from 17 - 19 December 1999

As shown by *Swanson et al.* [1997], Rossby waves tend to break in the regions of weaker zonal winds. In such a situation one can expect inertia-gravity wave generation [*Uccellini and Koch*, 1987] at the exit region of the jet, as indicated in Figure 7.1.

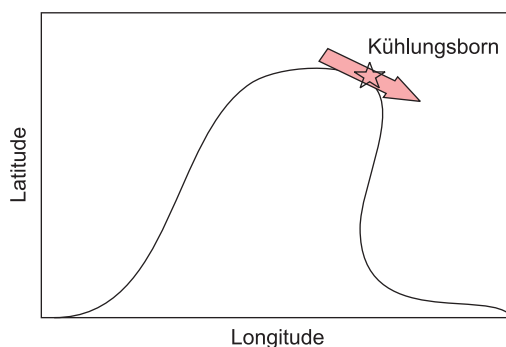


Figure 7.1: Schematic diagram of Rossby wave breaking and jet stream position over Northern Germany for LEWIZ campaign at 17 – 19 December, 1999. The star marks the position of Kühlungsborn. (After *Peters et al.* [2004]).

The meteorological situation during 17 - 19 December 1999 was connected with a poleward breaking Rossby wave, classified as a P2 event [*Peters and Waugh*, 1996], and leading to a strong eastward directed jet near the tropopause over Northern Germany.

The planning of the campaign was based on forecasts from the German Weather Service (DWD). A strong eastward directed jet over Northern Germany on 18 December 1999 in the upper troposphere was induced during the second phase of the Rossby wave breaking event north-eastwards of the anticyclone. For a more detailed description of this event we refer to *Peters et al.* [2003] and *Zülicke and Peters* [2004].

Figure 7.2 shows wind vectors larger than 20 m/s and geopotential heights derived from the ECMWF data at 12:00 UT on 18 December 1999 for the 300 hPa level corresponding to a height of approx. 9 km. The Rossby wave structure is indicated by the variations of the geopotential heights.

In Figure 7.3 height-time cross-sections of the smoothed zonal and meridional wind are presented for both locations at Kühlungsborn and at Lindenberg. The eastward directed zonal wind over Kühlungsborn (Figure 7.3a) increases until 19 December, 00:00 UT and then decreases. The maximum jet stream reaches values of more than 50 m/s at heights between 6 and 10 km. The meridional component (Figure 7.3b) shows southward directed winds with maxima of more than 20 m/s on 18 December (12-18 UT).

The observations with the wind profiler at Lindenberg (Figure 7.3c, Figure 7.3d) separated by about 265 km from the Kühlungsborn VHF radar, show the occurrence of the eastward and southward directed jets at nearly the same times and altitudes, whereas e.g. the reversal

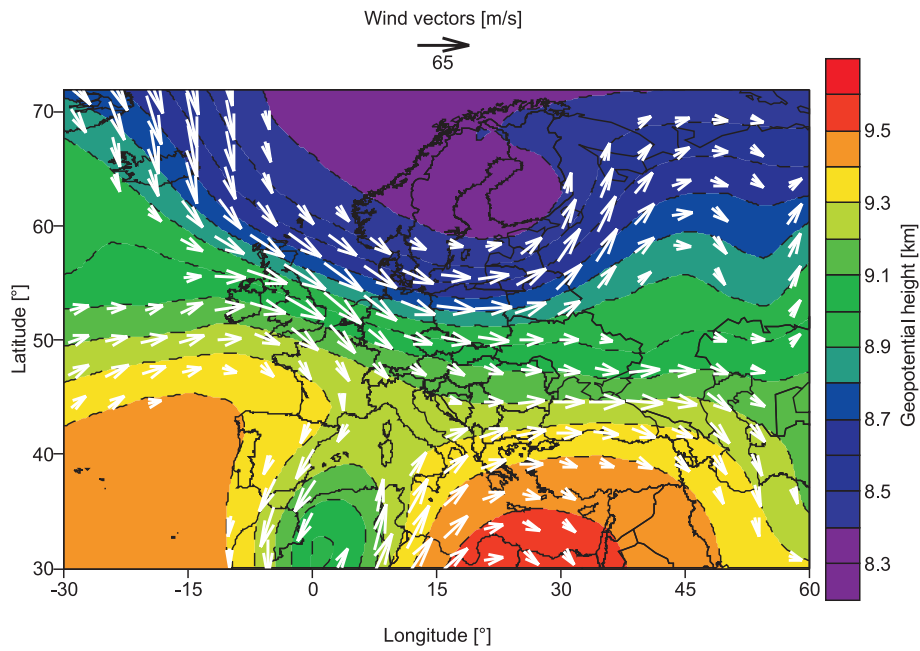


Figure 7.2: Wind vectors and geopotential height derived from ECMWF analyses for the 300 hPa level on 18 December 1999, 12:00 UT. Vectors are plotted only for wind speeds larger than 20 m/s. (After *Serafimovich et al.* [2005]).

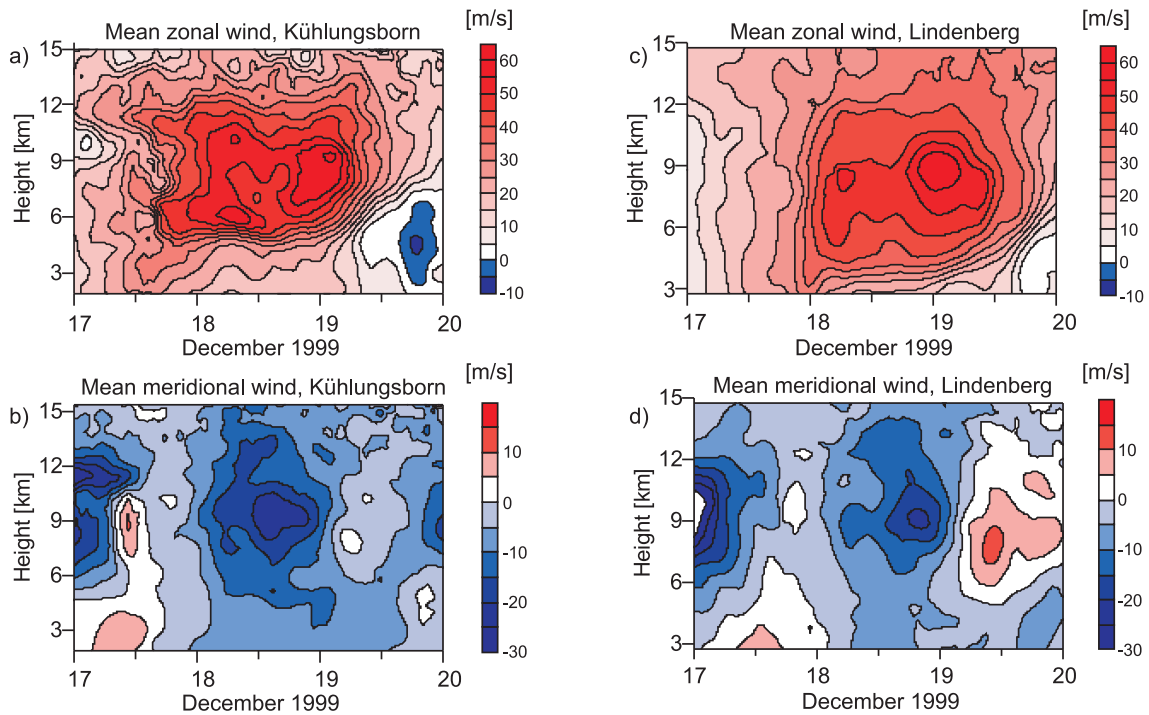


Figure 7.3: Mean zonal and meridional winds measured at Kühlungsborn (a,b) and Lindenberg (c,d) from 17 - 19 December 1999. The data are smoothed using a low-pass filter with cut off frequencies corresponding to 4h in time and 600m in altitude (After *Serafimovich et al.* [2005]).

of the meridional winds to northward directed winds on 19 December seems to be slightly stronger at Lindenberg. Detailed comparisons with the radiosondes [Peters *et al.*, 2003] and the 6 hourly - ECMWF analyses winds (Figure 4.4) result in good qualitative agreements but the radar measurements resolve a higher variability due to the better time resolution.

7.1.2 Inertia-gravity wave parameters estimation

Gravity waves detection

To examine the distribution of wind perturbations over the whole period and the investigated heights, we estimated a summarized scaled-averaged wavelet power of zonal and meridional winds at Kühlungsborn for periods 4–40 h and different height ranges (Figure 7.4). The scaled-averaged wavelet power [Torrence and Compo, 1998] corresponds to an averaged variance in a certain band versus time and height. Figure 7.4 shows the strongest amplitudes of the summarized variances of zonal and meridional winds at heights between 6–8 km and 9–12 km on 16 December and 17 December, respectively, and nearly no wave activity on 15 December and after 19 December 1999.

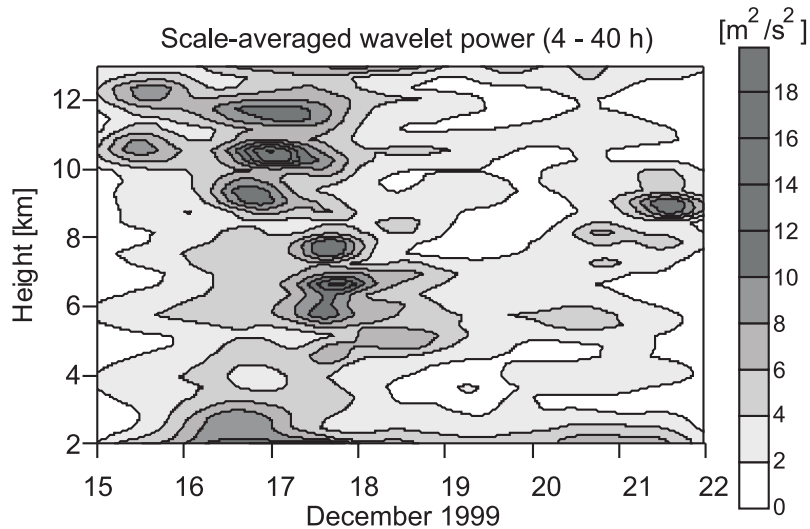


Figure 7.4: Sum of variances of zonal and meridional winds for periods from 4–40 h, derived from OSWIN VHF radar measurements at Kühlungsborn.

To localize the waves in height and time and to avoid arbitrary choices of inappropriate filter parameters, the wavelet transform (see Sect. 5.2) has been applied. The results of the wavelet analysis are presented by the sum of wavelet power spectra of the zonal and meridional wind components in Figure 7.5, measured at Kühlungsborn (a,b) and Lindenberg (c,d). The bold green line outlines the region with 95% significance level. The red shaded area indicates the zones where boundary effects appear, which are shown only for the wavelet transform of vertical profiles (Figure 7.5b,d). The analyzed time series are longer than presented (Figure 7.5a,c), therefore the regions of boundary effects are not shown.

From the wavelet transform of the wind time series, averaged in height from 5.45 km to 5.75 km at Kühlungsborn and from 5.25 km to 5.75 km at Lindenberg, shown in Figure 7.5(a and c), we detect suitable similarities at both locations with significant periods between 4–7 and 9–14 h including a dominant period of about 12 h and a less pronounced period of about 6 h on 17 December. We note, that in contrast to the observed dominant wave with a period

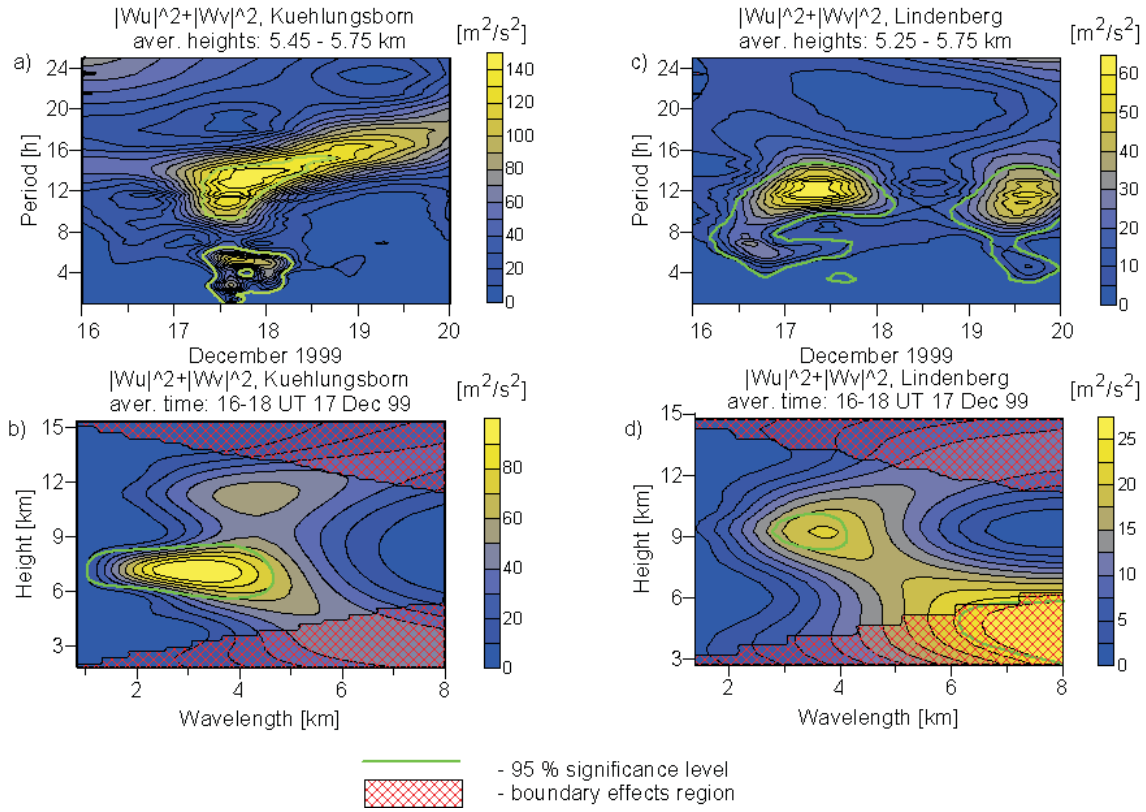


Figure 7.5: The sum of wavelet spectra applied to the zonal and meridional winds at Kuehlungsborn (a, b) and Lindenberg (c, d). The upper panel (a, c) shows the Morlet wavelet transform of the time series averaged over the altitude ranges (a) 5.45–5.75 km and (c) 5.25 – 5.75 km. The lower panel (b, d) shows the Paul wavelet transforms of vertical profiles of horizontal winds, averaged in time. (After *Serafimovich et al.* [2005]).

of 9–14 h, the shorter waves didn't show up in the two stations at the same time. Here we can only speculate that the sources of these 6 h-waves could be connected with frontal activities or deep convection in the boundary layer. Furthermore, we find significant vertical wavelengths on the order of 2–4 km near the tropopause region (7–9 km) from the wavelet transforms of vertical profiles of horizontal winds (b and d) averaged in time from 16:00 UT to 18:00 UT on 17 December, for Kuehlungsborn as well as for Lindenberg.

Evaluating this information from the wavelet transforms, we identified the existence of common waves at both places. The observed periods lie in the range of tidal waves. However, as will be shown in the following analysis, these waves have shorter vertical wavelengths and larger amplitudes than tidal waves, which practically play no role in the troposphere due to their small amplitudes in comparison to those of the gravity waves.

Based on the derived periods and vertical wavelengths of gravity waves, suitable filter parameters can be defined for different time and height ranges. We divided our analysis in two parts in order to investigate both frequency bands with periods of about 12 h and about 6 h, respectively. For the investigation of waves with dominant observed periods of about 12 h the filter was constructed (case A) with a bandwidth of 8 - 18 h in the time and 2 - 4.5 km in the height, whereas in case (B) a filter with a bandwidth of 2 - 8 h in the time and 2 - 4.5 km in the height has been applied to study waves with periods of about 6 h.

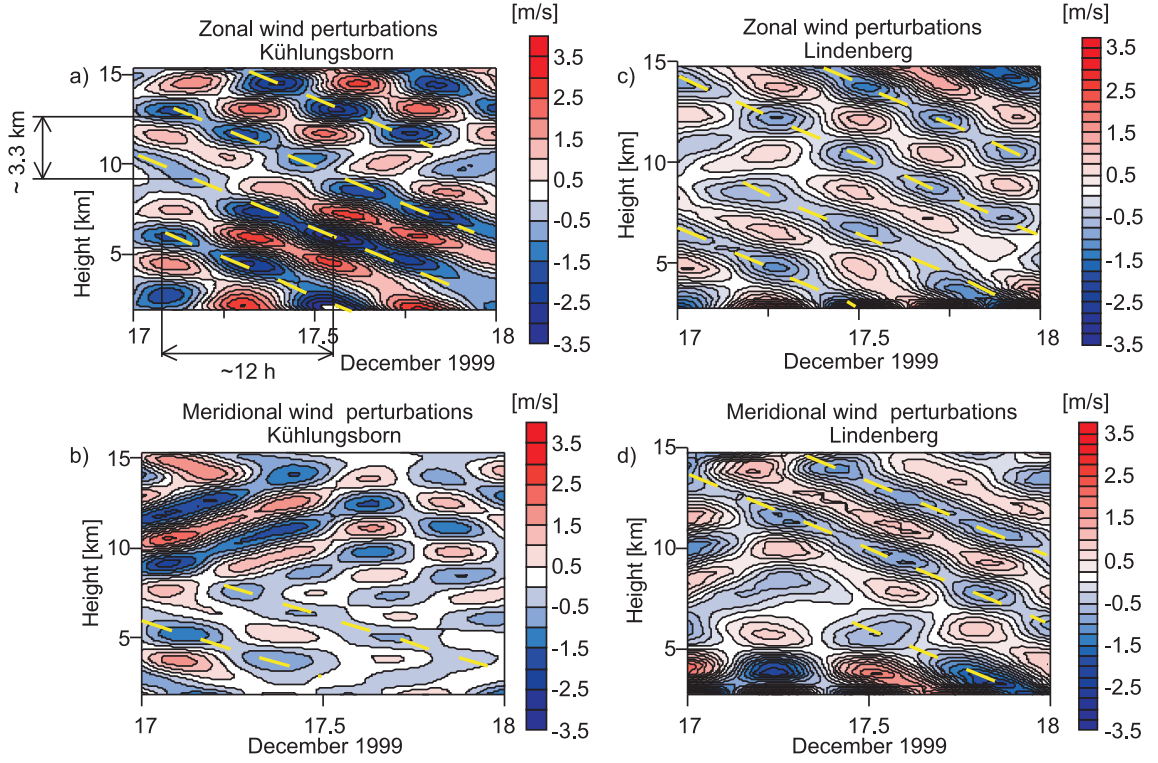


Figure 7.6: Zonal and meridional wind perturbations at Kühlungsborn (a) and Lindenberg (b) on 17 December 1999 after band pass filtering with bandwidths of 8-18 h in time and 2-4.5 km in height (After *Serafimovich et al.* [2005]).

For the first case (A), the resulting perturbations of the zonal and meridional winds at Kühlungsborn and at Lindenberg are shown in Figure 7.6. From Equation 2.1 at a fixed location x, y , the dashed lines indicate lines of constant phases of the dominant wind perturbations

$$mz - \omega_{ob}t = const \quad (7.1)$$

indicating preferred downward phase propagations with the clearest signatures in the perturbations of the zonal winds. The vertical and temporal distances between the phase lines correspond to vertical wavelengths of ~ 3.3 km and periods of ~ 12 h, respectively.

To investigate waves with periods of about 6 h in the second case (B), the results after the filter application on the zonal and meridional winds measured at Kühlungsborn and Lindenberg are shown in Figure 7.7 leading to dominating downward phase propagating perturbations with periods of about 6 h and vertical wavelengths of about 3 km.

The results confirm over an extended height-time-range the main findings from wavelet analyses applied to both wind components for selected time/height ranges at both locations, shown in Fig. 7.5. This is not obvious in every case, since the wind perturbations shown in Figs. 7.6 and 7.7 are characterized by superpositions of atmospheric waves with different frequencies in the selected frequency band and their height/time dependence. The presented wave signatures in Fig. 7.6 are much clearer than in Fig. 7.7 as expected after the wavelet analysis with the stronger amplitudes at periods of about 12 h.

The observed downward phase propagations for both waves indicate upward energy prop-

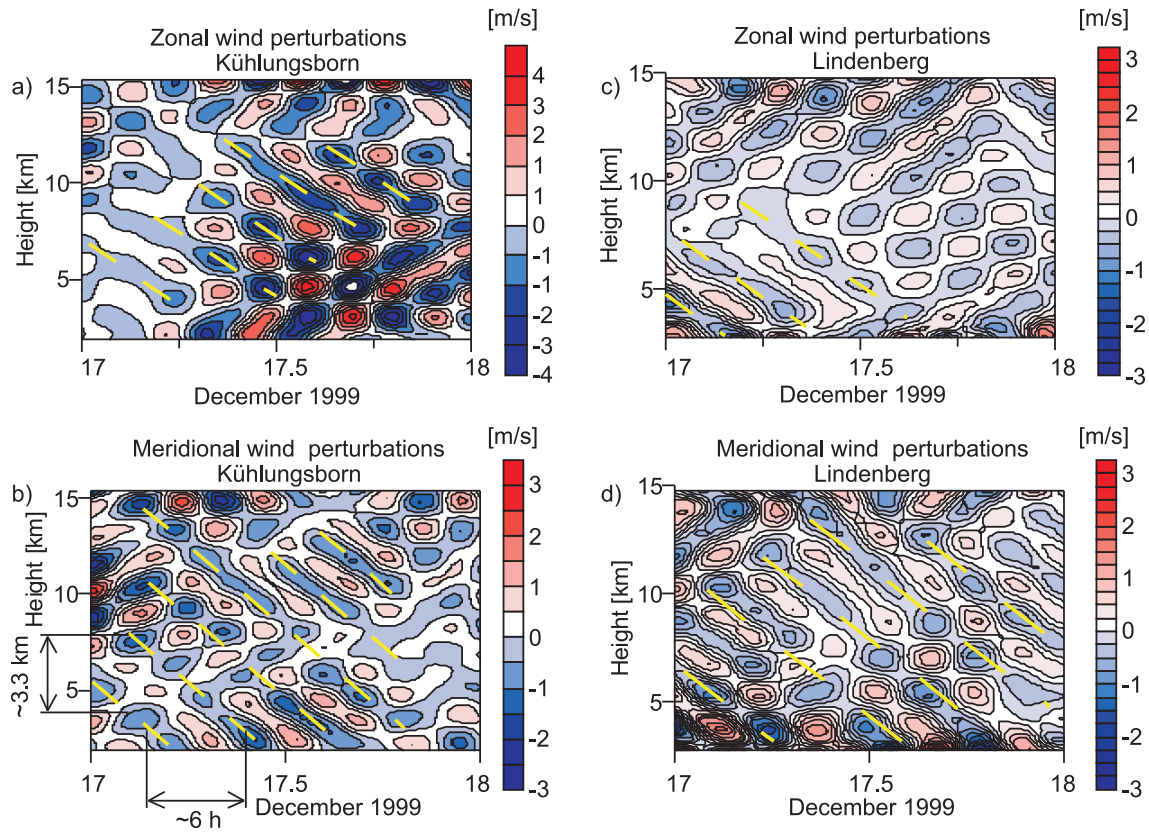


Figure 7.7: Zonal and meridional wind perturbations at Kühlungsborn (a) and Lindenberg (b) on 17 December 1999 after band pass filtering with bandwidths of 2-8 h in time and 2-4.5 km in height (After *Serafimovich et al.* [2005]).

agations, if both frequencies ω_{ob} and $\hat{\omega}$, connected by the Doppler relation (Equation 2.9), have the same signs. However, as shown later in agreement with previous investigations in *Peters et al.* [2003], the hodograph and rotary spectra analyses for the waves with observed periods of ~ 12 h lead to downward energy propagation, which is possible if the Doppler-shift is strong enough to turn the phase lines.

Normally such wind perturbations as shown in both Figures 7.6 and 7.7 are characterized by a superposition of atmospheric waves with different frequencies in the selected frequency band. The evaluation of the phase propagation derived for each wind component to estimate gravity wave characteristics is only possible if there exists only one dominant wave in a constant mean background wind. The analyses of all gravity wave parameters are based on the use of zonal as well as meridional winds derived from both filtered data sets.

Rotary spectra

As shown in Section 6.1, the presence of an inertia-gravity wave and its dominant vertical energy propagation are reflected by peaks in the rotary spectra. In case (A), the application of this method on wind perturbations filtered with a bandwidth of 8-18 hours in time and 2-4.5 km in height is presented in Figure 7.8 during the maximum of the wave activity (solid lines). The spectra show in their negative parts the weaker clockwise rotational power corresponding to an upward energy propagation and in their positive parts the larger

counterclockwise rotational power corresponding to a dominating downward directed energy propagation, respectively. The spectra are significant except at the maximum peak which shows more variability for averaged heights.

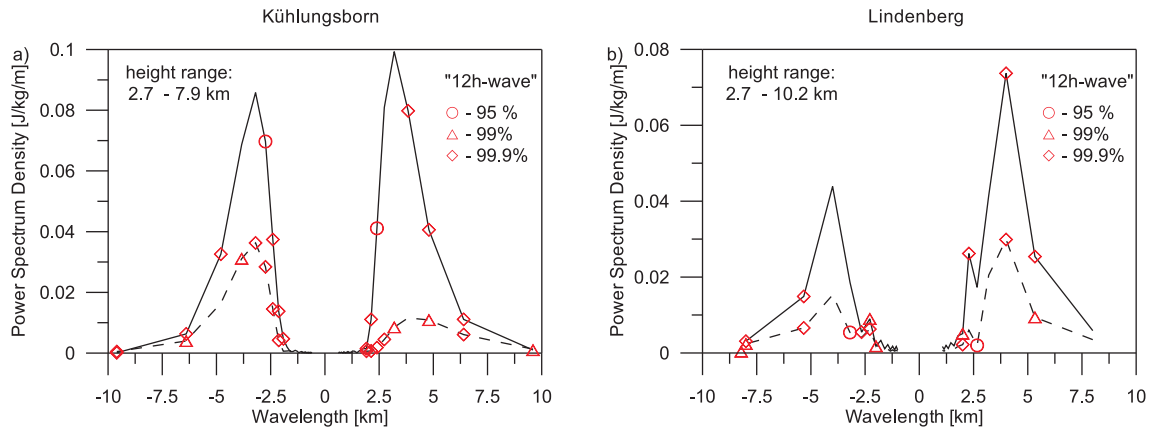


Figure 7.8: Results of the rotary spectra for Kühlungsborn(a) and Lindenberg(b) after band pass filtering with bandwidths of 8-18 h in time and 2-4.5 km in height. The solid lines show the spectra averaged for 5 hours on 17 December 1999 starting from 10:00 UT for Kühlungsborn(a, solid line) and 19:00 UT for Lindenberg(b, solid line). The dashed lines show the spectra averaged for 5 hours on 15 December 1999 starting from 00:00 UT for Kühlungsborn(a, dashed line) and 05:00 UT for Lindenberg(b, dashed line) (\circ , \triangle , \diamond correspond to 95%, 99%, 99.9% significance levels, respectively).

For comparisons we estimated the rotary spectra from measurements carried out on 15 December (Figure 7.8, dashed lines). During that time, the mean zonal and meridional winds are weaker and the variances of wind perturbations (Figure 7.4) are smaller. The rotary spectra have significant smaller amplitudes indicating smaller wave activity in absence of the strong jet (see also Figure 4.4).

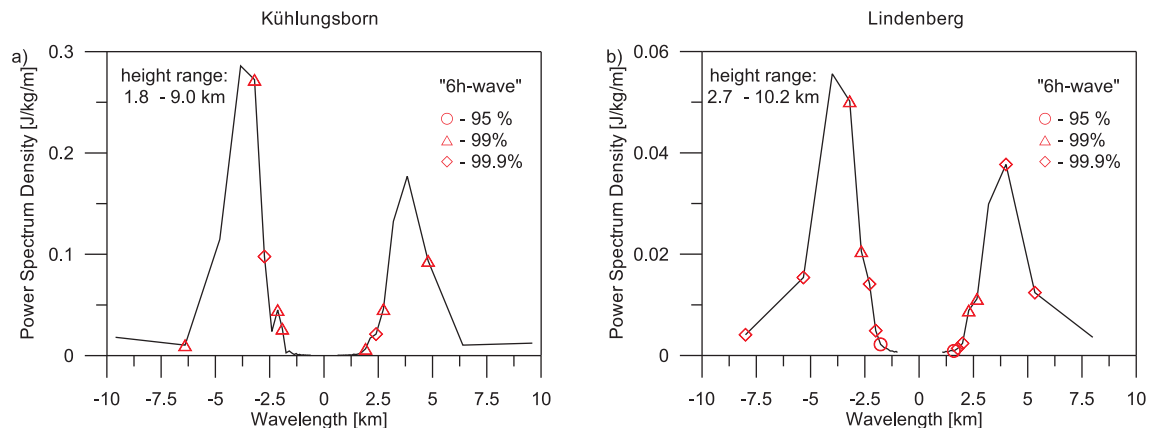


Figure 7.9: Results of the rotary spectra averaged for 5 hours on 17 December 1999 starting from 7:00 UT for Kühlungsborn(a) and 9:30 UT for Lindenberg(b) after band pass filtering with bandwidths of 2-8 h in time and 2-4.5 km in height (\circ , \triangle , \diamond correspond to 95%, 99%, 99.9% significance levels, respectively).

In case (B), the rotary spectra of the wind variations (Figure 7.9) filtered with bandwidths of 2 - 8 h and 2 - 4.5 km show a dominating upward energy propagation.

Hodograph- and Stokes-parameter analyses

The hodograph analysis (Section 6.2) applied to the wind perturbations on 17 December 1999 to investigate the gravity waves with the observed periods of about 12 h (case A) (Figure 7.10), shows a downward energy propagation in the troposphere from the anticlockwise rotational sense at Kühlungsborn and Lindenberg. We derived vertical wavelengths of about 3 km and intrinsic periods in the order of ~ 7 and ~ 12 hours from the ratios of the major to the minor axis of the ellipses at both locations, respectively. The differences between the hodographs for Kühlungsborn and Lindenberg can be caused by the spatial dependence of the wave characteristics. The variability of the background winds or interactions with other waves are possible reasons for such changes of the wave parameter at both stations.

For waves with observed periods of about 6 h (case B), the hodographs presented in Figure 7.11 show intrinsic frequencies with corresponding periods between 6 and 8 h and upward energy propagations at both locations in agreement with the rotary spectra in Figure 7.9. To demonstrate the stability of the wave propagation over a larger height range we have added in the right part (b) of the hodograph in Figure 7.11 the wind perturbations from 4.25 – 7.7 km and from 11. – 14.25 km, showing the same vertical sense corresponding to upward directed energy propagation with increasing amplitudes at larger heights.

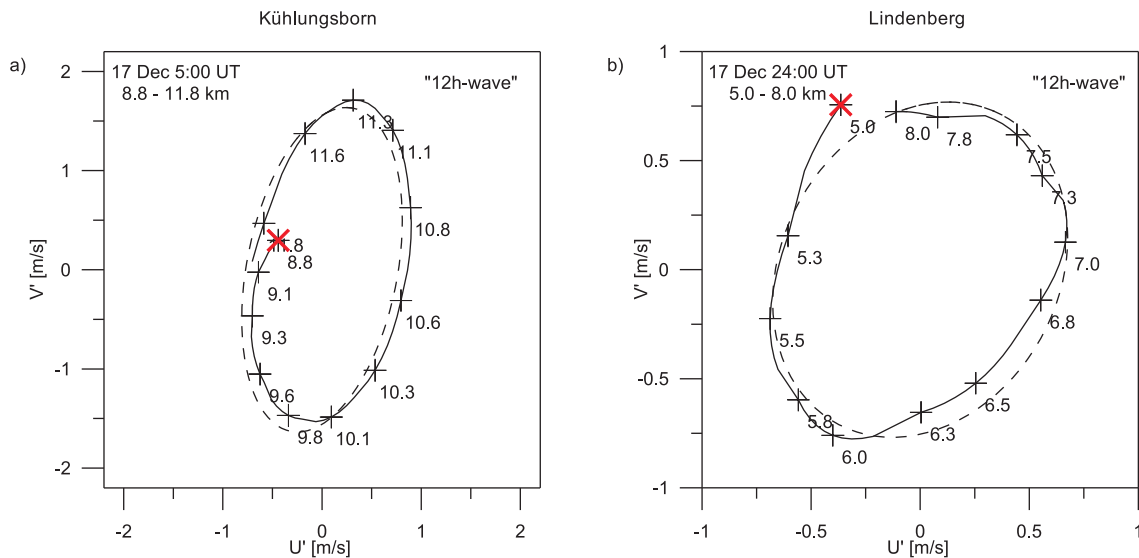


Figure 7.10: Results of hodograph analyses for the wind perturbations after band pass filtering with bandwidths of 8-18 h in time and 2-4.5 km in height (solid line - measured profiles, dashed line - fitted ellipse, **X** - starting point of the hodograph), applied to radar measurements at Kühlungsborn (a) and Lindenberg (b) (After *Serafimovich et al.* [2005]).

To receive a more statistical description of the gravity wave field, we applied the Stokes-parameter technique (Section 6.3). The Stokes parameters calculated for the data on 17 December 1999 are presented in Table 7.1 for both filtered data sets to investigate the gravity waves with periods of about 12 h and 6 h, respectively. As already mentioned in Sections 6.2 and 6.3, the horizontal wave propagation determined by the major axis orientation Θ is uncertain by 180° without additional information of temperatures or vertical winds. Comparing the mean results derived for intervals of 5 h, we obtained at both locations similar parameters as e.g. the wave propagation directions represented by Θ_{m_1, m_2} . Note that the averaging times have been selected by evaluating the time dependence of the total variances, described

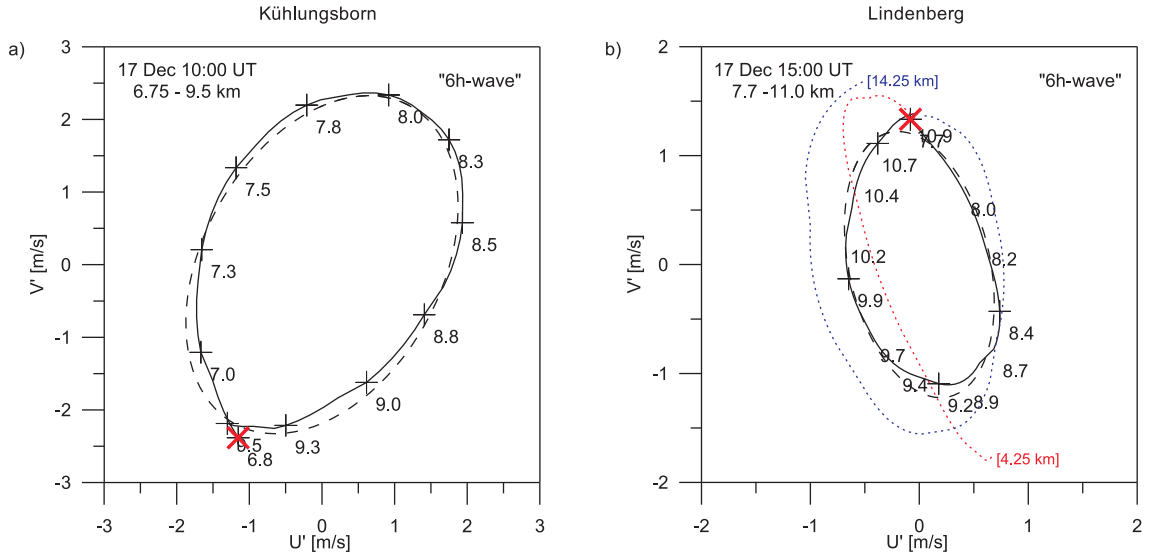


Figure 7.11: Results of the hodograph analysis applied to the wind perturbations after band pass filtering with bandwidths of 2–8 h in time and 2–4.5 km in height (solid line – measured profiles, dashed line – fitted ellipse, **X** – starting point of the hodograph), applied to radar measurements at Kühlungsborn (a) and Lindenberg (b). In (b), the hodograph has been extended from 4.25–7.7 km (red dashed line) and from 11.0–14.25 km (blue dashed line) (After *Serafimovich et al.* [2005]).

by the Stokes parameter I (Equation 6.2), which characterizes the mean kinetic energy for the investigated interval and vertical wavenumber band.

	case A "12h-wave"		case B "6h-wave"	
	Kühlungsborn	Lindenberg	Kühlungsborn	Lindenberg
Filter band (time; height)	8–18 h; 2–4.5 km		2–8 h; 2–4.5 km	
Averaged time (UT)	00:00-05:00	10:00-15:00	00:00-05:00	07:00-12:00
Stokes parameters				
Degree of polarization, d_{m_1, m_2}	0.88	0.79	0.55	0.62
Major axis orientation, Θ_{m_1, m_2}	50.5°	58.6°	77.8°	88.1°
Phase difference, δ_{m_1, m_2}	67.5°	63.4°	79.9°	93.9°
Ellipse axial ratio, R_{m_1, m_2}	0.66	0.58	0.66	0.40

Table 7.1: Stokes parameters derived from radar measurements at 17 December 1999 for Kühlungsborn.

Cross-spectral analysis

To identify common wave events over a distance of ~ 265 km, we will at first apply a simple cross-spectral analysis described in Section 6.6. After the detection of the appearance of dominating waves in both data sets with wavelet transform as shown in Figure 7.5, the cross

spectrum (Equation 6.21)

$$S_{U_1 U_2}(\nu) = \frac{\langle U_1(\nu) U_2^*(\nu) \rangle}{\langle |U_1(\nu)|^2 \rangle^{\frac{1}{2}} \langle |U_2(\nu)|^2 \rangle^{\frac{1}{2}}},$$

is calculated (Figure 7.12).

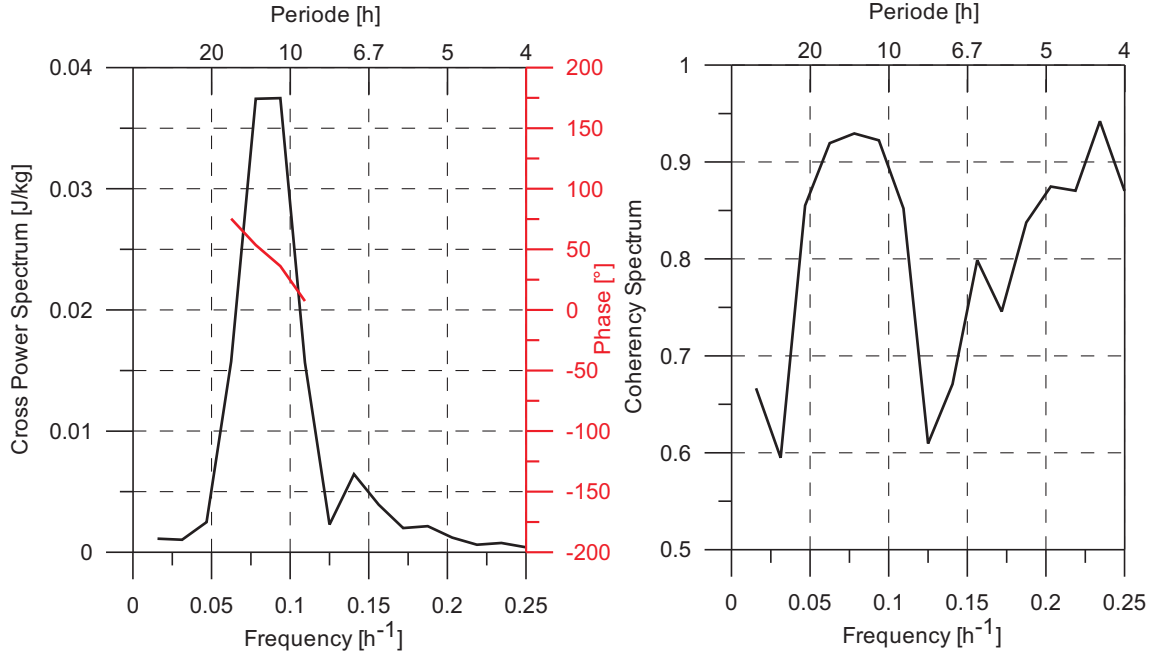


Figure 7.12: Cross-power spectrum of radar measurements at Kühlungsborn and Lindenberg for the time from 17 December 1999, 0:00 UT to 18 December 1999, 0:00 UT, averaged over the height range from 5.25 km to 7.75 km. Left part: Amplitude (black) and phase difference (red). Right part: Coherency spectrum (After *Serafimovich et al.* [2005]).

The cross power spectrum of the zonal winds measured at Kühlungsborn and Lindenberg, presented in the left part of Figure 7.12, has been averaged over the altitude range between 5.25 and 7.75 km. The amplitude of the cross spectrum shows a dominating common wave with an observed period of about 11.4 h which is in good agreement with the dominant period estimated by the wavelet transforms of the time series at both locations as shown in Figure 7.5(a, c). The significance of this wave is proved by the coherency spectrum shown in the right part of Figure 7.12. Due to the slopes of the phase lines in Figure 7.6 and the downward energy propagation with a vertical wavelength of about 3.3 km shown by the rotary spectra (Figure 7.8) and hodograph analysis (Figure 7.10), the observed frequency corresponding to the period of 11.4 h must be negative (Equation 5.10). With this information and following Equation 6.22

$$\tau = T_{ob} \frac{\Delta\phi}{360^\circ}$$

the phase difference (red line in Figure 7.12) of about 40° or -320° between the maxima of this wave at both locations corresponds to time delay τ of about -1.3 h or +10.1 h, respectively.

To estimate the horizontal wave number k_h and the ground based horizontal phase velocity v_{ph} directly from the cross-spectral analysis, we have applied Equations 6.27

$$L_h = \frac{|S|\cos\alpha}{\tau/T_{ob} - (z_2 - z_1)/L_z}$$

and Equation 6.28

$$v_{ph} = \frac{|S|\cos\alpha}{\tau - (z_2 - z_1)T_{ob}/L_z}$$

using the radar coordinates and the wave direction $\Theta \approx 54^\circ$, estimated by the Stokes-parameter analysis applied for the dominating waves with periods of about 12 h and filtered with band widths between 8 and 18 h (see Table 7.1). Note that in this case at both locations the directions of the wave propagation differ by only 8° , so that there are no ambiguities to estimate α and to apply the cross-spectral analysis.

A realistic height shift $z_2 - z_1$ of the wave, required in Equations 6.27 and 6.28, can be estimated with a mean vertical phase velocity of

$$\hat{v}_{pz} = \frac{\omega_{in}}{m} \approx 0.1 \text{ m/s} \quad (7.2)$$

where ω_{in} is derived from the polarization relation (Equation 2.24) using the mean ellipse ratio derived with the Stokes-parameter analysis (see Table 7.1), and yields to values $\tau v_{pz} \approx -500$ m for the time delay $\tau = -1.3$ h.

The results are shown in Table 7.2. Using the realistic height shift of -500 m, a horizontal wavelength of about -307 km and an observed horizontal phase speed of 7.3 m/s have been derived. To check the sensibility on the final results, we have added a 10% change to the realistic height shift, leading to variations of about 10% in the horizontal wavelength, and of about 5% in the observed horizontal phase speed, respectively. Furthermore, the other assumed height shifts lead to larger deviations. However, as we will see later in Figure 7.13, the derived observed phase velocity of about 7.3 m/s agrees very well with the results separately estimated for each radar location.

Vertical shift $\Delta z, \text{ km}$	Horizontal wavelength $2\pi/k, \text{ km}$	Observed horizontal phase speed $v_{ph}, \text{ m/s}$
0	-714	17.4
-0.5(-0.45;-0.55)	-307(-325;-290)	7.3(7.8;6.9)
-1.0	-195	4.8

Table 7.2: Horizontal wavelengths and ground-based phase speeds derived from the cross-spectral analysis as a function of the vertical height shift for the wave with observed period $2\pi/\omega_{ob}$ of -11.4 h, using a major axis orientation, $\Theta = 54^\circ$, distance $|S|$ between both radars of 265 km and time delay $\tau = -1.3$ h.

Gravity wave characteristics and discussion

We have used two ways to solve the Doppler relation (Equation 2.9), the polarization relation (Equation 2.24), and the dispersion relation (Equation 2.25). If the ellipse ratio R and ω_{ob}

are given, then the intrinsic frequency $\hat{\omega}$, the horizontal wavenumber k and the vertical wavenumber m can be estimated by solution of the three aforementioned equations. In the second way, the ellipse ratio R and the vertical wavenumber m are given by the evaluation of the spectra with respect to height. Then Equations 2.24 and 2.25 have to be solved to estimate the intrinsic frequency $\hat{\omega}$ and the horizontal wavenumber k .

To investigate the gravity waves with observed periods of about 12 hours, we follow the first way to solve the Equations 2.9, 2.24 and 2.25 using the Stokes parameter shown in Table 7.1 and the mean winds \bar{u} , \bar{v} estimated with Equation 2.28 from the dominating jet stream at the height of about 9 km (see e.g. Figure 7.3). To resolve the ambiguities in the polarization relation (Equation 2.24) and in the quadratic dispersion relation (Equation 2.25) and to determine the signs of the wavenumbers, we used in addition the slopes of the constant phase lines (Equation 5.10) in the wind perturbations (Figure 7.6) in comparison with the downward energy propagation as estimated by the rotary spectra (Figure 7.8).

	case A "12h-wave"		case B "6h-wave"	
	Kühlungsborn	Lindenberg	Kühlungsborn	Lindenberg
Filter band (time; height)	8–18 h; 2–4.5 km		2–8 h; 2–4.5 km	
IGW parameters				
Mean horizontal wind, \bar{U} , m/s (in the wave propagation direction)	17	18	2.9	−1.3
Wind shear component, $\partial\bar{V}/\partial z$, s^{-1}	$2.8 \cdot 10^{-3}$	$-0.5 \cdot 10^{-3}$	$-1.7 \cdot 10^{-3}$	$1.4 \cdot 10^{-3}$
Intrinsic period, $2\pi/\hat{\omega}$, h	7.7	8.3	8.3	6.0
Observed period, $2\pi/\omega_{ob}$, h	−11.4	−11.4	6.4	6.4
Horizontal wavelength, $2\pi/k_h$, km	−281	−313	225	158
Vertical wavelength, $2\pi/m$, km	3.3	3.6	−3.2	−3.2
Horizontal phase velocity, \hat{v}_{ph} , m/s	−10.1	−10.3	7.5	7.3
Vertical phase velocity, \hat{v}_{pz} , m/s	0.11	0.12	−0.1	−0.15
Horizontal group velocity, \hat{c}_{gh} , m/s	−6.6	−7.3	5.6	6.2
Vertical group velocity, \hat{c}_{gz} , m/s	−0.08	−0.08	0.08	0.12

Table 7.3: Gravity waves parameters at about 9 km and 6 km derived from the Stokes-parameter analysis as shown in Table 7.1 for the radar measurements at Kühlungsborn and Lindenberg.

The derived gravity wave characteristics are given in Table 7.3, resulting in consistent parameters at both locations like the horizontal wavelengths as well as the group and phase velocities. The dispersion relation leads to vertical wavelengths between 3.3 and 3.6 km, which are in the order of the results of the wavelet analyses (Figure 7.5) or the rotary spectra (Figure 7.8). Note, that the relation

$$\hat{v}_{ph} = \frac{\hat{\omega}}{k_h} = \frac{\omega_{ob}}{k_h} - \bar{u}_h \quad (7.3)$$

between the intrinsic and the ground-based horizontal phase speed is only fulfilled if the intrinsic phase speed \hat{v}_{ph} and hence the horizontal wavenumber k_h are negative. Figure 7.13

shows the horizontal wave vector \vec{k}_h , vectors of the intrinsic and phase velocities of this wave. The values in brackets are estimated by the analysis of radar measurements at Kühlungsborn separately and by the cross-spectral analysis of measurements at Kühlungsborn and Lindenberg.

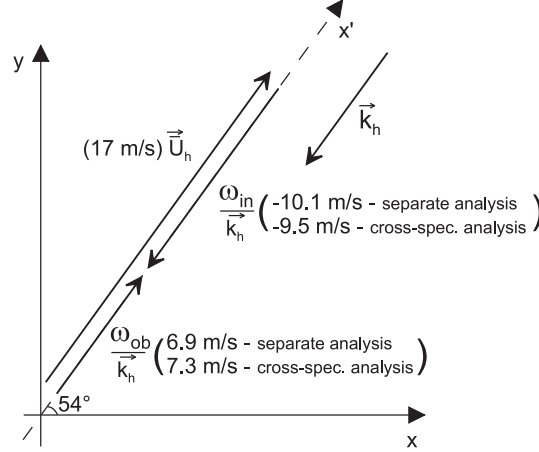


Figure 7.13: Horizontal wave vector, observed and intrinsic phase velocities of the inertia-gravity wave with an observed period ~ 12 h, detected at Kühlungsborn and Lindenberg on 17 December 1999.

The intrinsic phase velocities \hat{v}_{phc} estimated from the cross-spectral analysis, ($v_{ph}=7.3$ m/s, see Table 7.2) using the mean winds at both locations (Table 7.3) parallel to the wave direction

$$\hat{v}_{phc} = v_{ph} - \bar{u} \quad (7.4)$$

yields to values of -9.5 m/s and -10.5 m/s, which agree very well with the results v_{ph} separately estimated for Kühlungsborn (-10.1 m/s) and Lindenberg (-10.3 m/s, see Table 7.3), respectively.

Thus, the results estimated for each radar location and leading to negative wavenumbers k and horizontal wavelengths of about 300 km confirm the results derived directly from the cross-spectral analysis, using the mean wave directions estimated from the Stokes-parameter analysis and a realistic height shift of -500 m corresponding to a mean vertical phase velocity v_{pz} of about 0.1 m/s for the time delay of -1.3 h.

We have to note for the case investigated here, that the estimations of the horizontal wavelengths depend primarily on changes in the component of the mean background wind parallel to the wave direction as used in the Doppler relation (Equation 2.9), whereas the influence of the vertical wind shear effects used in Equations 2.24 and 2.25 leads to changes in the intrinsic period of 1.6 h and in the horizontal wavelength of about 40 km.

For the waves with periods of about 6 h, the sign of ω_{ob} must be positive due to the slopes of the phase lines in Figure 7.7 and the upward energy propagation (Figure 7.9) (see Equation 5.10). In this case we found solutions applying the second way based on a given ellipse ratio R and the vertical wavenumber m , estimated by the evaluation of the spectra with respect to height and using the Stokes parameters shown in Table 7.1. The solution of Equations 2.24 and 2.25 leads to the estimation of the intrinsic frequency $\hat{\omega}$ and the horizontal wavenumber k for a height of about 6 km as shown in Table 7.3. Note that in this case the sign of the wavenumber k must be positive to fulfill Equation 7.3. Therefore we conclude that these less pronounced waves with horizontal wavelengths of about 200 km are moving

with the wind. Due to their upward directed energy propagation (Figure 7.9) we can only speculate that a possible source for these waves is connected with frontal activity or deep convection in the boundary layer. This also could be the reason why these waves didn't show up in the two stations at the same time, as already shown by the wavelet analyses (Figure 7.5 a,c).

We summarize, that we found in this case study two wave classes with different energy propagation directions at both radar sites. Both wave classes show downward phase propagations. Connected with a jet stream in the upper troposphere and due to the shift in the frequency by the Doppler-effect, the dominating wave with a period -11.4 h shows a downward energy propagation in the troposphere. The analysis also shows that the direction of the wave propagation is upstream and the intrinsic period is ~ 8 h. Horizontal wavenumbers for this wave are negative and vertical wavenumbers are positive at both locations with corresponding wavelengths between -281 and -313 km as well as between 3.3 and 3.5 km, respectively. Additionally to this wave class, we detected another one with shorter horizontal wavelengths and a smaller observed period of 6.4 h, which has an upward directed energy propagation. The horizontal and vertical wavelengths of this wave are ~ 200 km and -3.2 km, respectively.

Gravity waves and vertical momentum fluxes

The vertical flux of horizontal momentum is important to describe transport of energy and momentum by gravity waves and to investigate the wave mean-flow interactions. *Vincent and Reid* [1983] developed a radar method to estimate momentum fluxes $\overline{u'w'}$ and $\overline{v'w'}$ from symmetric-beam Doppler measurements directly (Section 6.7).

To extend our investigation in the frame of LEWIZ campaign carried out in December 1999 and discussed in previous Section 7.1, we estimated the zonal and meridional momentum fluxes, as well as the flux densities and mean flow accelerations. The radar measurements of Doppler winds from 17-19 December 1999 were averaged in time for 4 hours and split into blocks with a duration of 12 hours. After that, the time averaged of $\overline{u'w'}$ (Figure 7.14 top panel) and $\overline{v'w'}$ (Figure 7.15 top panel) for each block were derived. In that way, we separated contributions to momentum fluxes only from waves with observed periods from 8 up to 12 hours [*Fritts and Vincent*, 1987] concentrating on the inertia-gravity wave with an observed period -11.4 hours which we detect in the previous analysis. Using the pressure values (after *U.S. Standard Atmosphere*, 1976), we derived the flux densities (Figures 7.14 and 7.15 middle panel) and mean flow accelerations (Figures 7.14 and 7.15 bottom panel).

From visual inspection of Figures 7.14 and 7.15, we concluded that the temporal development of horizontal fluxes and mean-flow accelerations shows consistent maxima on 17 December 1999. These maxima are indicating higher wave activity during that time in agreement with the maxima seen in the wavelet analyses (Figure 7.5) and the averaged variances of the winds (Figure 7.4).

The vertical flux of the zonal momentum for this day tends to be positive with an amplitude of 1.2 m^2/s^2 in the troposphere and then changes at a height of about 8 km to a negative sign with an amplitude of -0.6 m^2/s^2 . The vertical flux of the meridional momentum is close to zero in the troposphere and has a negative peak with amplitude of -1.5 m^2/s^2 at the height about 8 km. The amplitudes of the fluxes are in good agreement with typical values ~ 0.1 - 0.2 m^2/s^2 in a case study of flows under similar conditions [*Lilly and Kennedy*, 1973; *Nastrom and Fritts*, 1992].

The vertical divergences of the momentum fluxes or mean-flow accelerations show opposite peaks at this height and then tends to be zero indicating a zonal acceleration near the

tropopause. Such a behavior of the vertical fluxes is explained by the existence of a source for the generation of gravity waves and hence for the energy propagation from the jet region in different directions.

Note that these are first results, and further investigations including comparisons with modelling (see Section 7.2.2) are necessary, especially to improve the knowledge about wave mean-flow interactions.

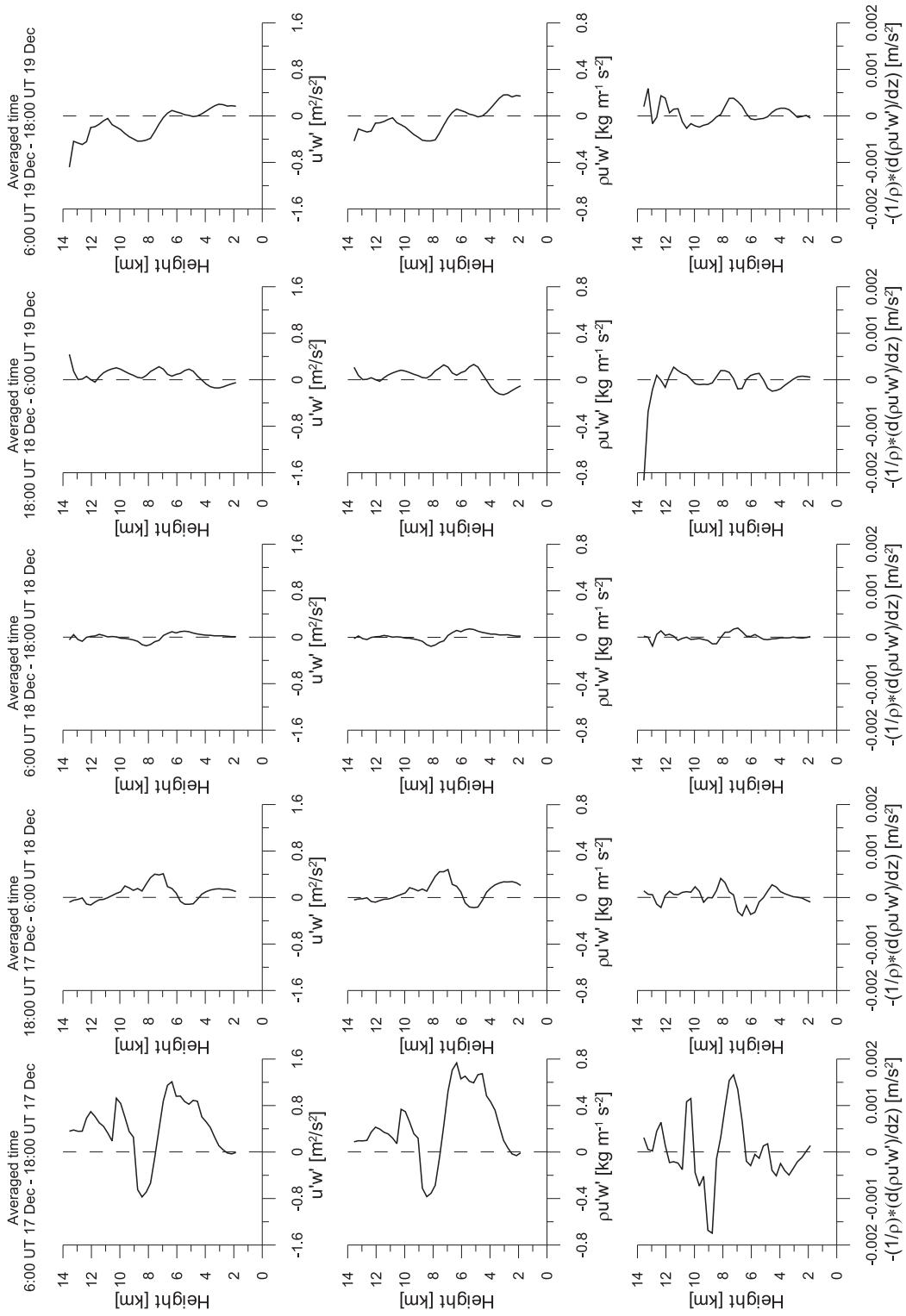


Figure 7.14: Vertical fluxes (upper panel), flux densities (middle) and mean-flow accelerations (lower panel) of the zonal momentum derived from the radar measurements at Kühlungsborn in December 99.

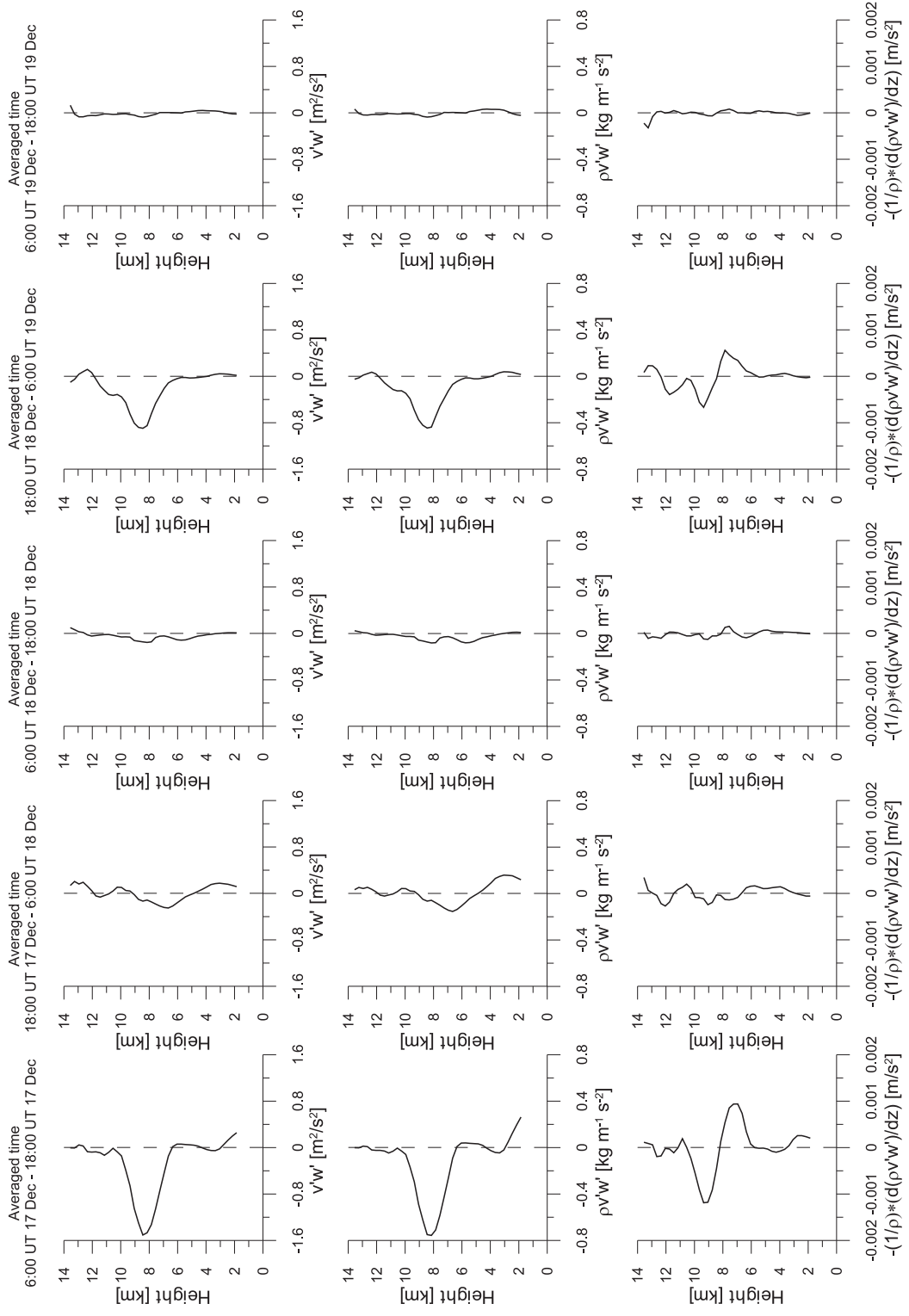


Figure 7.15: Vertical fluxes (upper panel), flux densities (middle) and mean-flow accelerations (lower panel) of the meridional momentum derived from the radar measurements at Kühlungsborn in December 99.

7.1.3 An example of nonlinear wave-wave interaction in February 2002

As already discussed, there are waves in the atmosphere with different frequencies and different sources, including such waves which are a product of nonlinear wave-wave interactions. Motivated by simultaneously occurring waves detected by the wavelet analysis (see Figure 7.17, right), in this section we apply the bispectral analysis (Section 5.5) to measurements from one of the LEWIZ campaigns carried out at Kühlungsborn in February 2002 to investigate possible nonlinear interactions between the waves. The mean zonal and meridional winds from 2 - 8 February are presented in Figure 7.16.

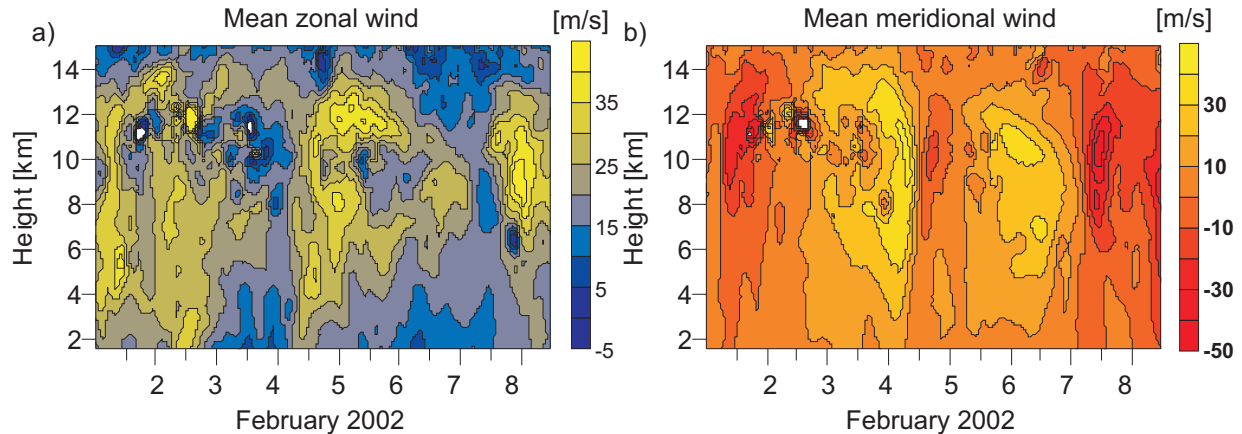


Figure 7.16: Mean zonal (a) and meridional (b) winds measured at Kühlungsborn from 2 - 8 February 2002. The data are smoothed using a low-pass filter with cut off frequencies corresponding to 4h in time and 800m in altitude.

The meridional wind shows clear oscillations with a period of about 3 days. The zonal wind shows the maximum peak of 40 m/s on 5 February, whereas the meridional wind reaches its minimum during that time.

The application of the wavelet transform to the wind measurements shows the appearance of the waves with different wavelengths and periods at the same time and same height (Figures 7.17-7.19). For example, from the wavelet transform of the meridional wind profile at 0:00 UT on 2 February 2002 (Figure 7.17) two waves with vertical wavelengths 1.8 km and 3.2 km are detected. The wavelet transforms of the time series show a peak with a period 10 h on 2 February 2002 at 12 km (Figure 7.18), and two peaks with periods of 18 h and 32 h during noon on 4 February at a height of 6 km (Figure 7.19).

To check the existence of waves which are the results of nonlinear wave-wave interactions, we applied the bispectral analysis. The results are shown on the left sides of Figures 7.17-7.19. The bold black lines on these figures connect the peaks, corresponding to the frequencies of the waves participating in the nonlinear wave-wave interactions. From the bispectrum of the meridional wind profile at 00:00 UT on 2 February 2002 (Figure 7.17), we can summarize that the waves with vertical wavelengths 4.8 km and 10 km interact with each other resulting in a specific wave with a vertical wavelength of 4.1 km. The waves with vertical wavelengths 1.9 km and 10 km interact with each other resulting in a wave with a vertical wavelength of 1.8 km. The waves with vertical wavelengths of 1.9 km and 4.1 km interact with each other resulting in a wave with a vertical wavelength of 1.4 km.

In the second case (Figure 7.18), the bispectrum of the time series at the height of 12 km shows peaks with periods of 8.1 h and 14.5 h corresponding to the waves participating in the

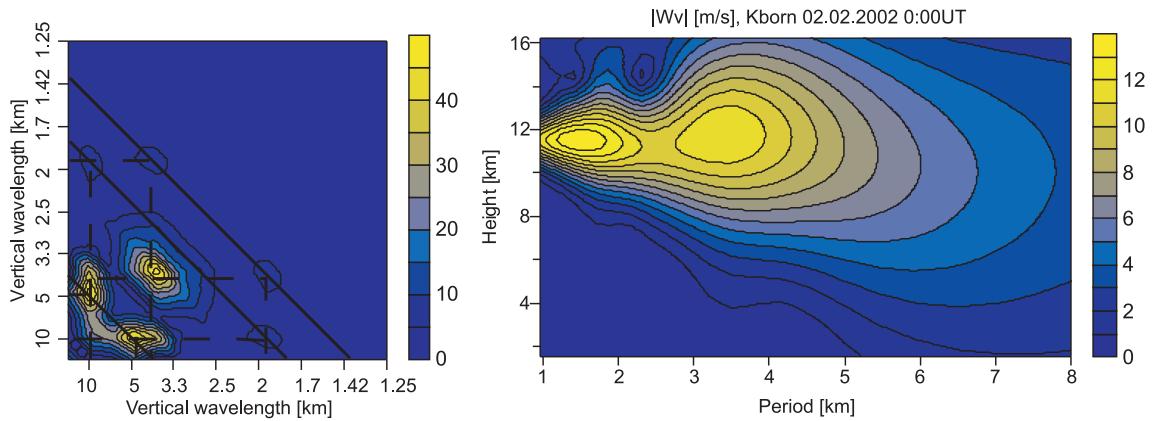


Figure 7.17: Bispectrum (left) and wavelet transform (right) of the meridional wind profile measured by OSWIN VHF radar at Kühlungsborn on 2 February 2002, 0:00 UT.

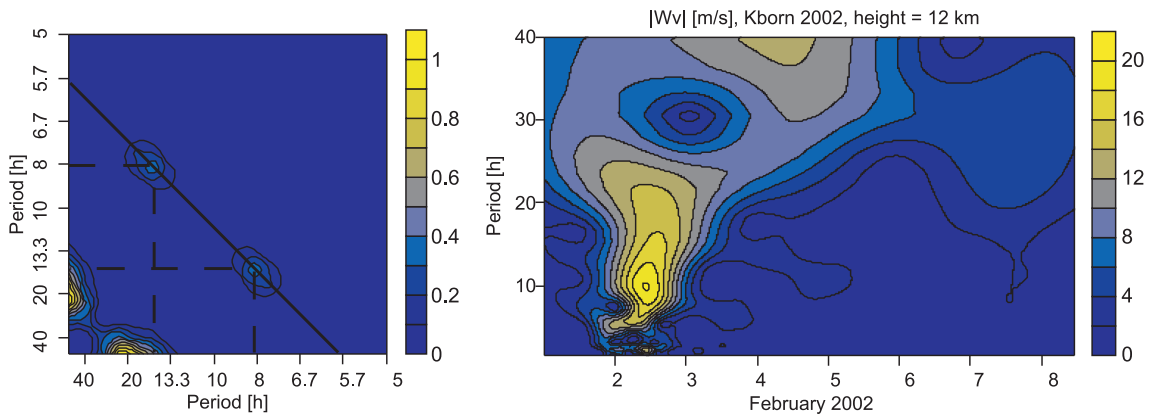


Figure 7.18: Bispectrum (left) and wavelet transform (right) of the meridional wind time series from 1-8 February 2002 measured at 12 km by OSWIN VHF radar at Kühlungsborn.

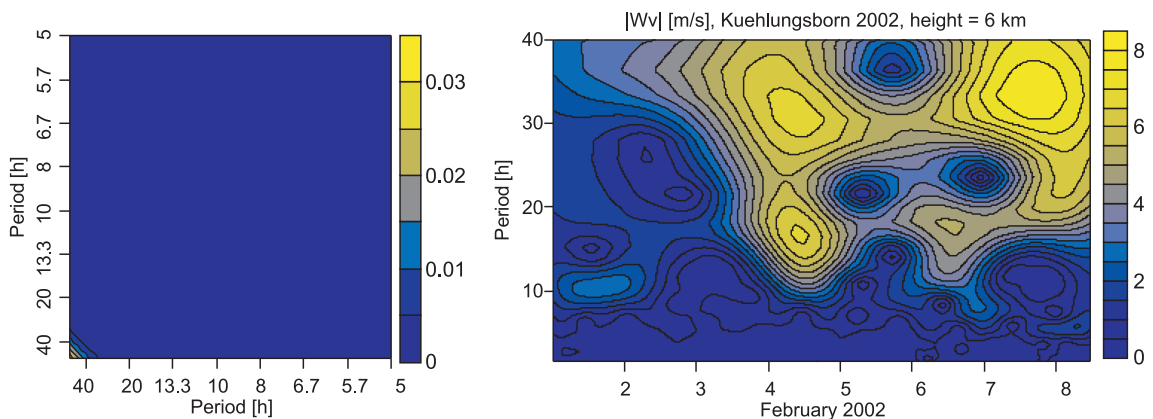


Figure 7.19: Bispectrum (left) and wavelet transform (right) of the meridional wind time series from 1-8 February 2002 measured at 6 km by OSWIN VHF radar at Kühlungsborn.

wave-wave interaction, and resulting in a wave with an observed period of 5.7 h which are also indicated by the wavelet analysis.

One example without any interactions between the waves is presented by the bispectrum

analysis of the meridional wind at a height of 6 km (Figure 7.19). Here, there are no peaks in the bispectrum, and all waves detected by the wavelet transform at this height have other sources and are not the results of nonlinear wave-wave interactions.

As shown here, the bispectrum is useful for the determination of those spectral components present in processes which are harmonically related and have quadratic phase coherence. The main result of the investigations presented above is that the waves with vertical wavelengths of ~ 1.4 km, ~ 1.8 km and ~ 4.1 km and observed period of 5.7 h, detected by the wavelet transforms, are results of the nonlinear wave-wave interactions.

7.2 Scandinavian mountain ridge: A case study

7.2.1 Inertia-gravity wave parameters estimation

To investigate inertia-gravity waves in a region with an additional orographical influence we are also reporting here on a case study using radar data from two sites at Andenes and Kiruna on the West- and East-sides of the Scandinavian mountain ridge, respectively. These investigations have been carried out in the frame of the MaCWAVE/MIDAS campaign to study the vertical propagation of the gravity waves up to the MLT region [Goldberg *et al.*, 2003], using radars and lidars at both sides of the Scandinavian mountain ridge, supplemented by meteorological rockets and radiosondes.

Between 23 - 26 January 2003, an eastward directed jet stream occurs towards the Scandinavian Mountains mostly south of the Andøya - Esrange region in Northern Scandinavia. Figure 7.20 describes the mean zonal wind derived from NCEP (National Center for Environmental Prediction) operational data sets for the 500 hPa level corresponding to a height of about 6 km.

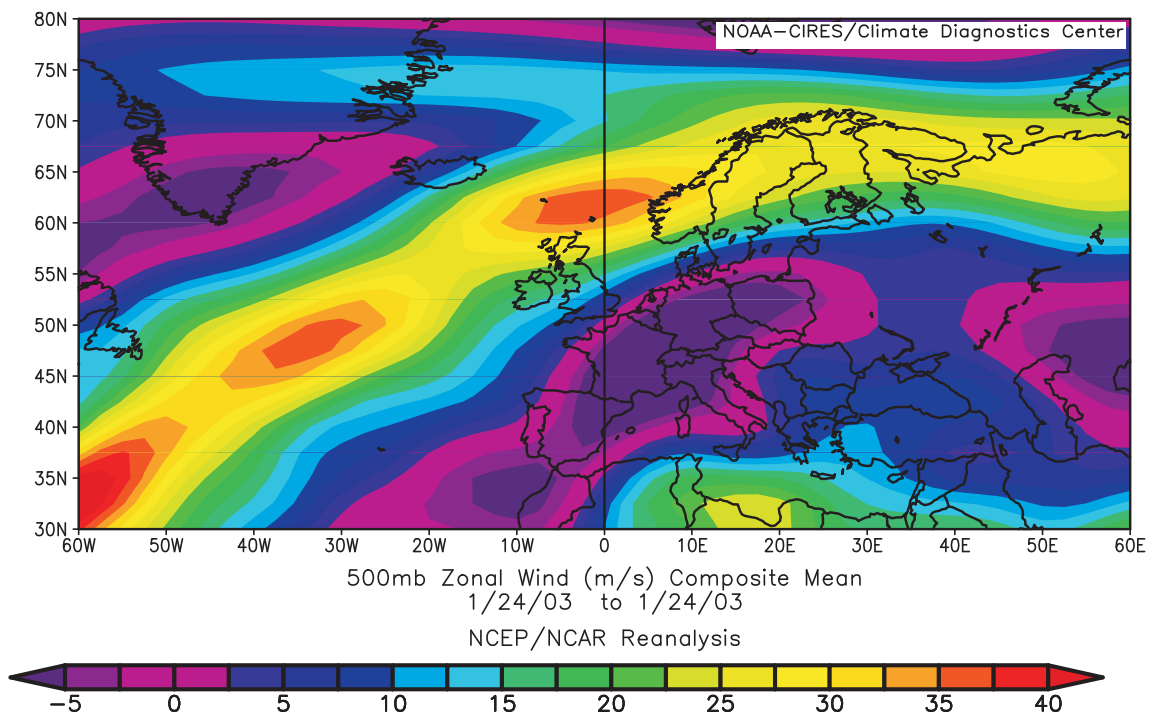


Figure 7.20: Mean zonal wind derived from NCEP/NCAR reanalyses on 24 January 2003 for the 500 hPa level.

In Figure 7.21 the mean winds derived for both radar locations before and behind the Scandinavian mountain ridge are presented. The temporal development of the zonal wind (Figure 7.21a) is characterized by a long periodic oscillation of more than 24 hours with maxima of the eastward directed wind on 24 January at both locations whereas the maxima in the meridional northward directed component (Figure 7.21b) occur approximately 12h later. Note that the amplitudes of the mean winds are slightly stronger at Kiruna (Figure 7.21c and d), as expected due to a possible amplification by mountain waves [Queney, 1948; Smith, 1979].

From the wavelet transform (Figure 7.22) we identified the time and height dependencies of the gravity wave at both locations and found similar significant peaks on 24 of January

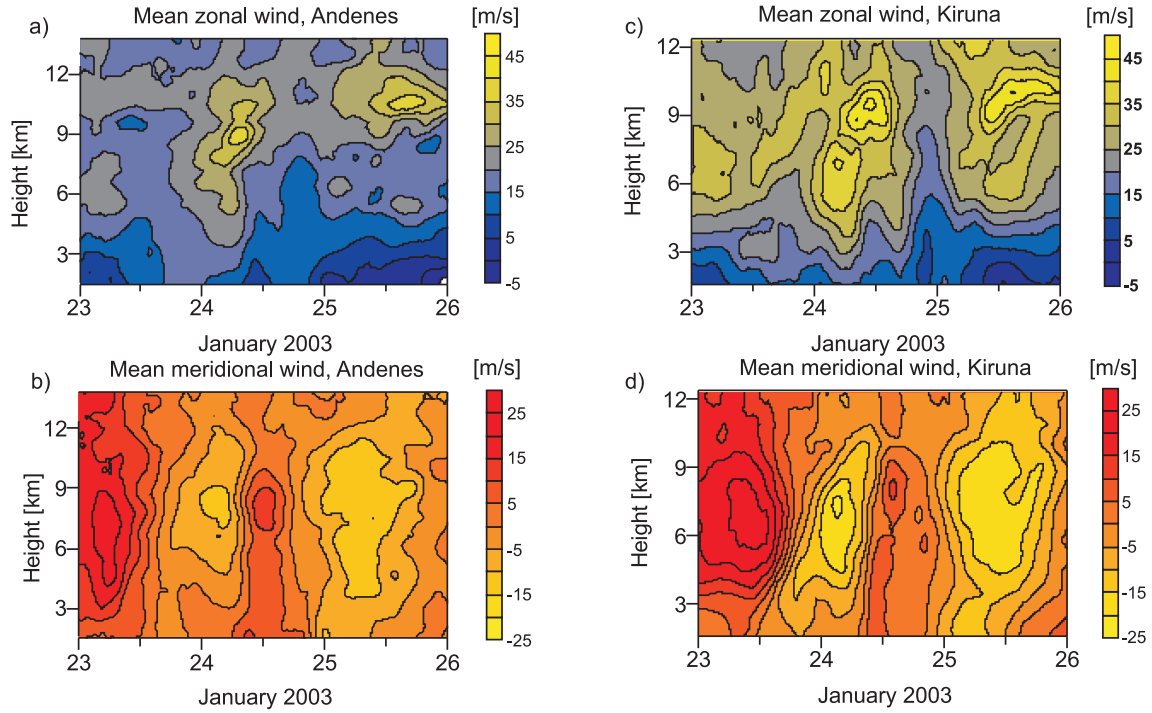


Figure 7.21: Mean zonal and meridional winds measured at Andenes (a,b) and Kiruna (c,d) from 23 - 25 January 2003. The data are smoothed using a low-pass filter with cut-off frequencies corresponding to 4h in time and 600m in altitude.

in the tropopause region with dominant period of about 12 hours and vertical wavelengths of ~ 3.5 km. Based on this information, we applied a band-pass filtering with bandwidths 8-18 hours and 2-6 km to estimate wind perturbations (Figure 7.23) from the mean winds.

The application of rotary spectra and hodograph analysis (Figure 7.24) shows a downward energy propagation in the troposphere and confirm the vertical wavelength of the gravity wave in the order of 3-4 km estimated by the wavelet analysis.

But as already discussed in Section 6.3, statistically better results are given by the Stokes-parameter analysis (Table 7.4). Applying this method, the data are averaged in time and over a wavenumber band corresponding to waves with vertical wavelengths between 1 km and 5 km.

Stokes parameters	Andenes	Kiruna
Degree of polarization, d_{m_1, m_2}	0.95	0.96
Major axis orientation, Θ_{m_1, m_2}	-12°	-22°
Phase difference, δ_{m_1, m_2}	-104.4°	124.8°
Ellipse axial ratio, R_{m_1, m_2}	0.54	0.42

Table 7.4: Stokes parameters derived from radar measurements on 25 January 2003 for 1 hour starting from 09:00 UT and averaged in wavelengths from 3.8 km to 6.4 km.

The solution of the Doppler relation (Equation 2.9), the polarization relation (Equation 2.24), and the dispersion relation (Equation 2.25) and using the Stokes parameters, shown in Ta-

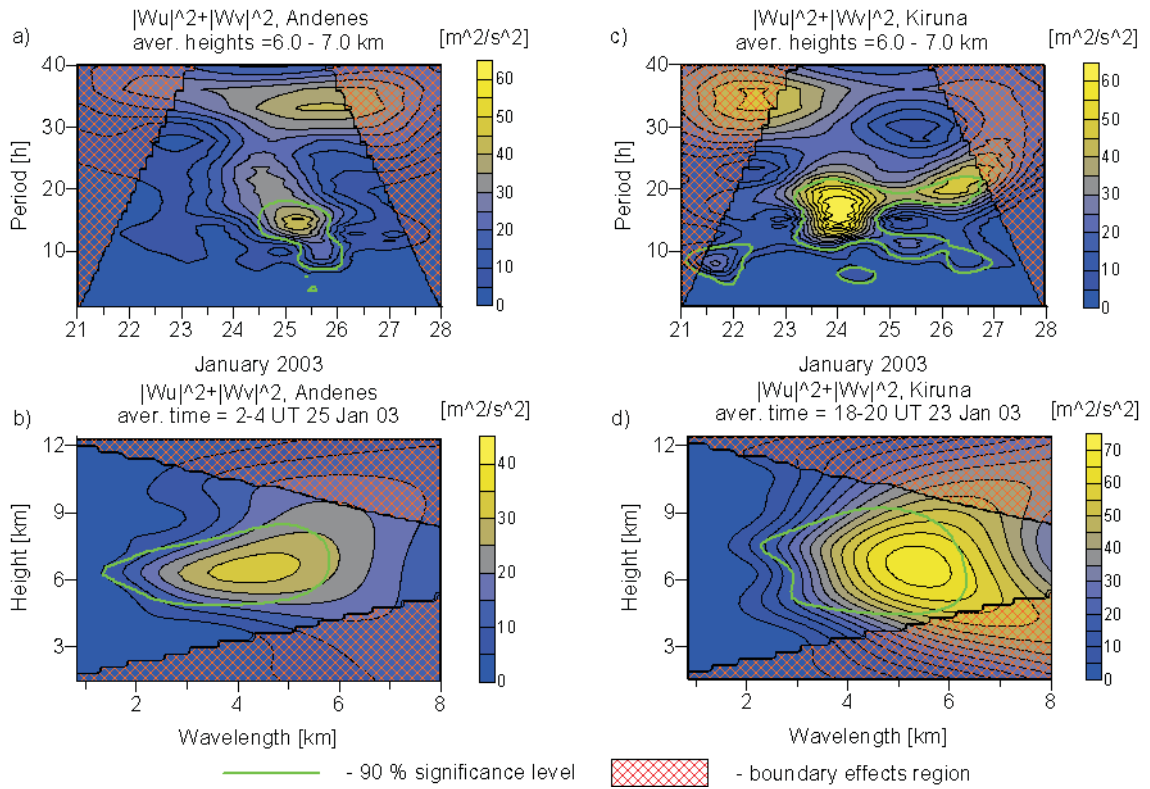


Figure 7.22: Sum of the wavelet spectra applied to the zonal and meridional winds. The upper panel (a, c) shows the Morlet wavelet transform of the time series averaged over the altitude ranges 6 – 7 km. The lower panel (b, d) shows the Paul wavelet transforms of vertical profiles of horizontal winds, averaged in time. Wind measurements at Andenes (a, b) and Kiruna (c, d) have been used.

ble 7.4, leads to the gravity parameters given in Table 7.5. Characteristic parameters like the horizontal wavelengths, the phase and group velocities as well as the orientation of the horizontal propagation show reasonable agreements for the wave events identified at both locations on the West- and East-sides of the Scandinavian mountain ridge.

Based on the wavelet transform of the radar measurements at Andenes and Kiruna (Figure 7.22a,c) we found a common wave at both locations on 24–25 of January with a period of about 12 hours. Furthermore, the direction of the wave propagation at Andenes is nearly the same as at Kiruna (Table 7.4). It gives us a good ability to apply the cross-spectral analysis (Figure 7.25) as described in Section 6.6.

The cross power spectrum of the zonal winds measured at Andenes and Kiruna (Figure 7.25, left panel) has been averaged over the altitude range between 4 and 8 km. For this case study, the amplitude of the cross spectrum shows a dominating common wave with an observed period of about 13.4 h. The significance of this wave is proved by the coherency spectrum (Figure 7.25, right panel). The phase difference (red line in Figure 7.25) of about 130° between the wave maxima at both locations, corresponding to time delay τ of about 4.8 h, leads to a horizontal wavelength of about -674 km and a horizontal phase velocity of the gravity wave of 33 m/s (Table 7.6).

The results derived by the analysis of radar measurements at Andenes and Kiruna separately (Table 7.4) and combined cross-spectral analysis (Table 7.6) are in qualitatively good agree-

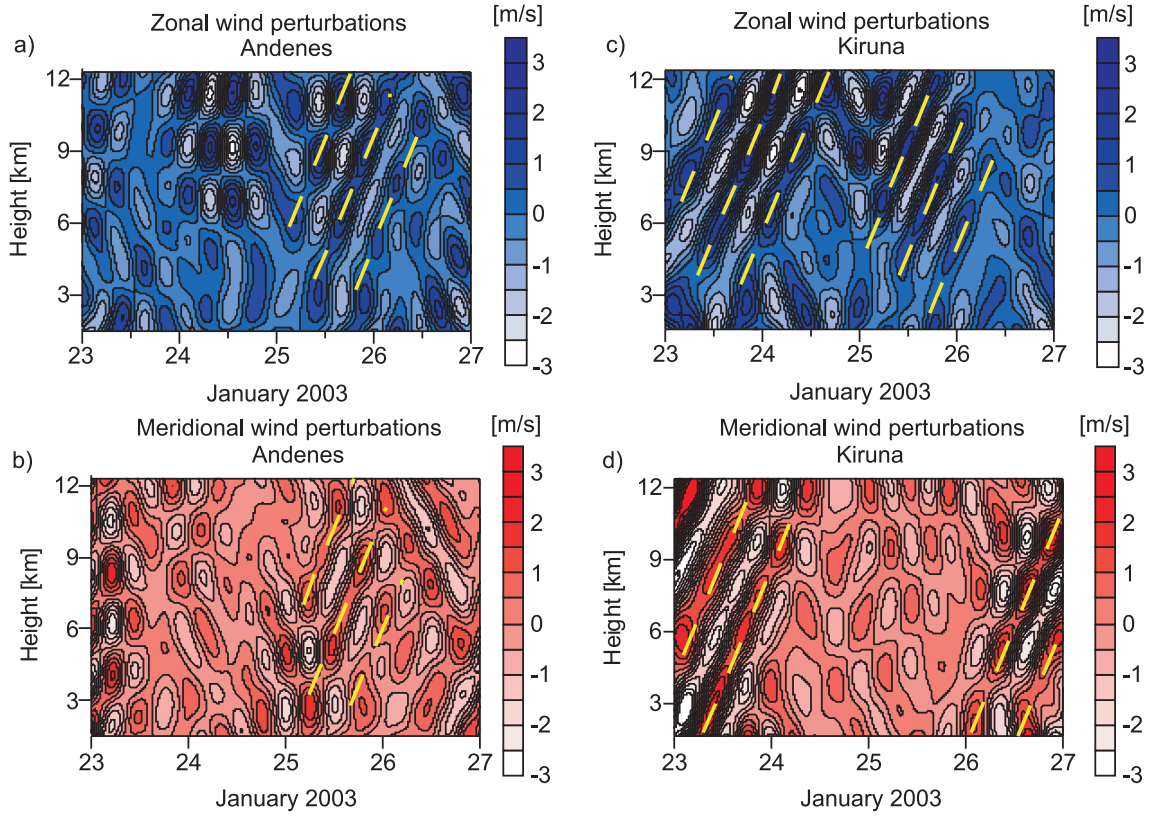


Figure 7.23: Zonal and meridional wind perturbations at Andenes (a,b) and Kiruna (c,d) for 23-26 January 2003 after band pass filtering with bandwidths of 8-18 h in time and 3-7 km in height.

IGW parameters	Andenes	Kiruna
Mean horizontal wind, \bar{u} , m/s	18.7	29.3
(in the wave propagation direction)		
Wind shear component, $\partial\bar{v}/\partial z$, s^{-1}	$-1.7 \cdot 10^{-3}$	$-1.2 \cdot 10^{-3}$
Intrinsic period, $2\pi/\hat{\omega}$, h	5.5	4.2
Observed period, $2\pi/\omega_{ob}$, h	13	14.5
Horizontal wavelength, $2\pi/k$, km	-663	-673
Vertical wavelength, $2\pi/m$, km	5.1	4.6
Horizontal phase velocity, \hat{v}_{ph} , m/s	-33	-44
Vertical phase velocity, \hat{v}_{pz} , m/s	0.2	0.3
Horizontal group velocity, \hat{c}_{gh} , m/s	-2.6	-2.0
Vertical group velocity, \hat{c}_{gz} , m/s	$-19 \cdot 10^{-3}$	$-15 \cdot 10^{-3}$

Table 7.5: Gravity waves parameters derived from the results of the Stokes-parameter analysis as shown in Table 7.4 for the radar measurements at Andenes and Kiruna.

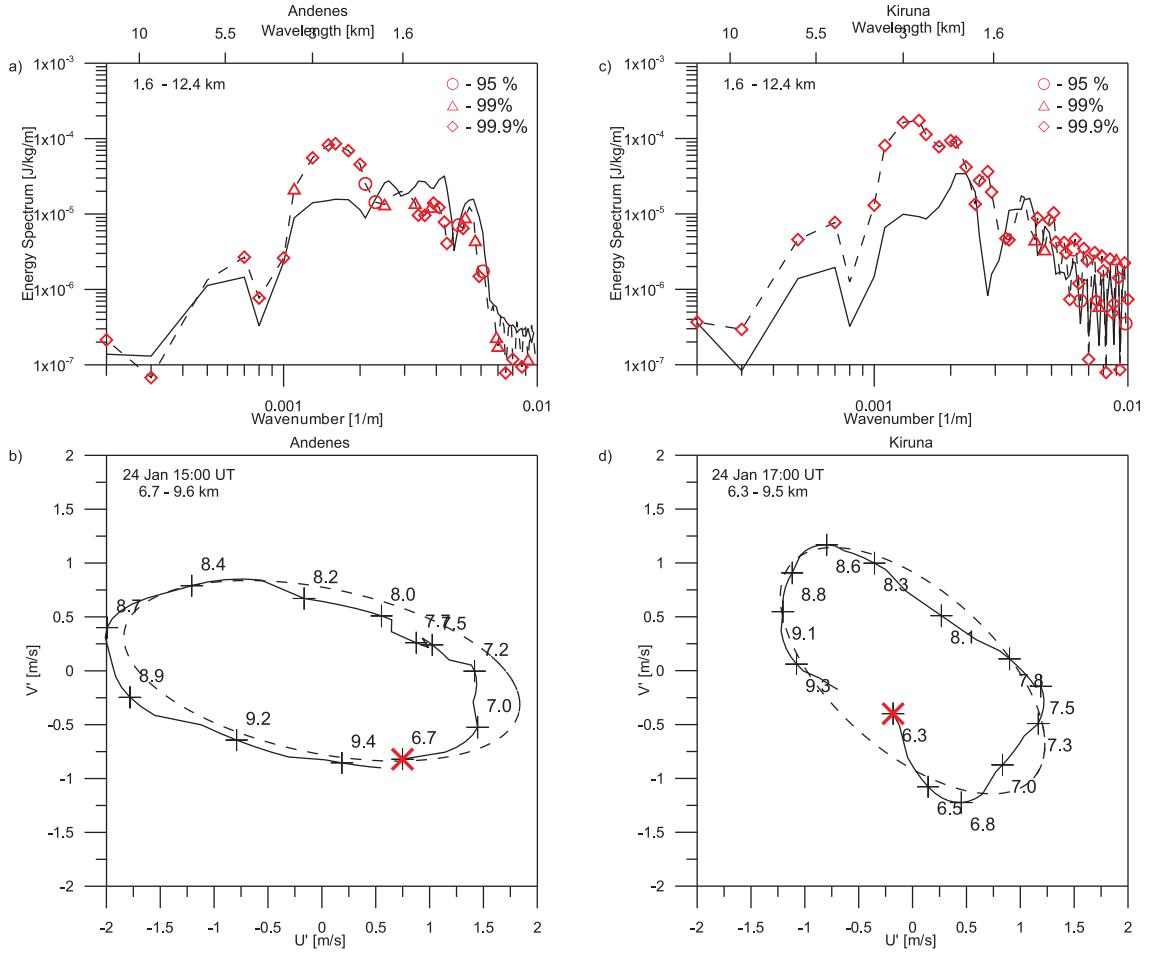


Figure 7.24: Results of rotary spectra averaged for 12 hours starting at 24.01.03 00:00 UT (solid line - positive part of the spectra, dashed - negative part, \circ , \triangle , \diamond - significance levels) and hodograph analysis (solid line - measured profiles, dashed line - fitted ellipse, \mathbf{X} - starting point of the hodograph). Both methods applied to radar measurements at Andenes (a,b) and Kiruna (c,d).

IGW parameters	
Observed period, $2\pi/\omega_{ob}$, h	13.4
Phase, $\Delta\phi$, $^\circ$	130
Distance, $ S $, km	≈ 260
Time delay, τ , h	≈ 4.8
Angle α (Figure 6.3), $^\circ$	-20.5
Horizontal wavelength, $2\pi/k$, km	-674
Horizontal phase velocity, \hat{v}_{ph} , m/s	-33

Table 7.6: Gravity waves parameters derived from cross-spectral analysis of radar measurements at Andenes and Kiruna.

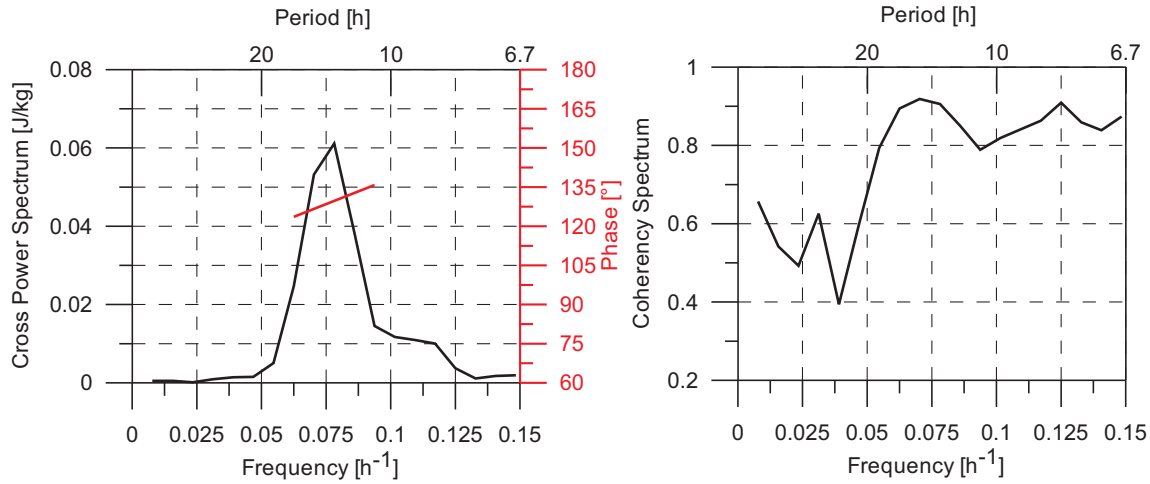


Figure 7.25: Cross-power spectrum between radar measurements at Andenes and Kiruna for the time from 24 January 2003, 0:00 UT to 26 January 2003, 24:00 UT, averaged over the height range from 4 km to 8 km. Left part: Amplitude (black) and phase difference (red). Right part: Coherency spectrum.

ment. In contrast to the characteristics of gravity waves detected in the frame of the LEWIZ campaign (Section 7.1), gravity wave analyzed in this section shows higher amplitudes especially on East-sides of the Scandinavian mountain ridge, as expected by the influence of mountains [Smith, 1979; Röttger, 2000]. The waves have longer horizontal and vertical wavelengths. Further analyses of pure standing mountain waves generated in that region and investigations of their possible interactions with jet induced inertia-gravity waves are necessary. Combined model analysis in connection with observations will contribute to understand such processes. First comparisons between observations and mesoscale MM5 model results are presented in the following section.

7.2.2 Comparison with the MM5 model

The PSU/NCAR mesoscale model is a limited-area, nonhydrostatic or hydrostatic, terrain-following sigma-coordinate model designed to simulate or predict mesoscale and regional-scale atmospheric circulation. It has been developed at Penn State and National Center for Atmospheric Research (NCAR) as a community mesoscale model and is continuously being improved by contributions from users at several universities and government laboratories. The Fifth-Generation NCAR / Penn State Mesoscale Model (MM5) is the latest in a series that developed from a mesoscale model. The MM5 model is well described by Dudhia [1993] and Grell *et al.* [1994], and successfully applied by Zülicke and Peters [2004] in the frame of the LEWIZ project.

For a first proof of the results derived from the radar measurements during the case study in January 2003, described in the previous Section 7.2.1, we will use here the MM5 model output simulated for the same time [Ch. Zülicke, *pers. comm.*, 2004].

Since MM5 is a regional model, it requires initial conditions as well as lateral boundary conditions to run. The ECMWF data were used to initialize the model and to simulate the zonal and meridional wind fields at the Andenes and Kiruna sides with time resolution of 1 h and vertical resolution of 50 m for the period from 24–26 January, 2003. The zonal and meridional wind fields measured by the ALWIN VHF radar at Andenes (Figure 7.26, left

panel) and realized by the MM5 model (Figure 7.26, right panel) show comparable features, like the wind maxima and minima in the same order.

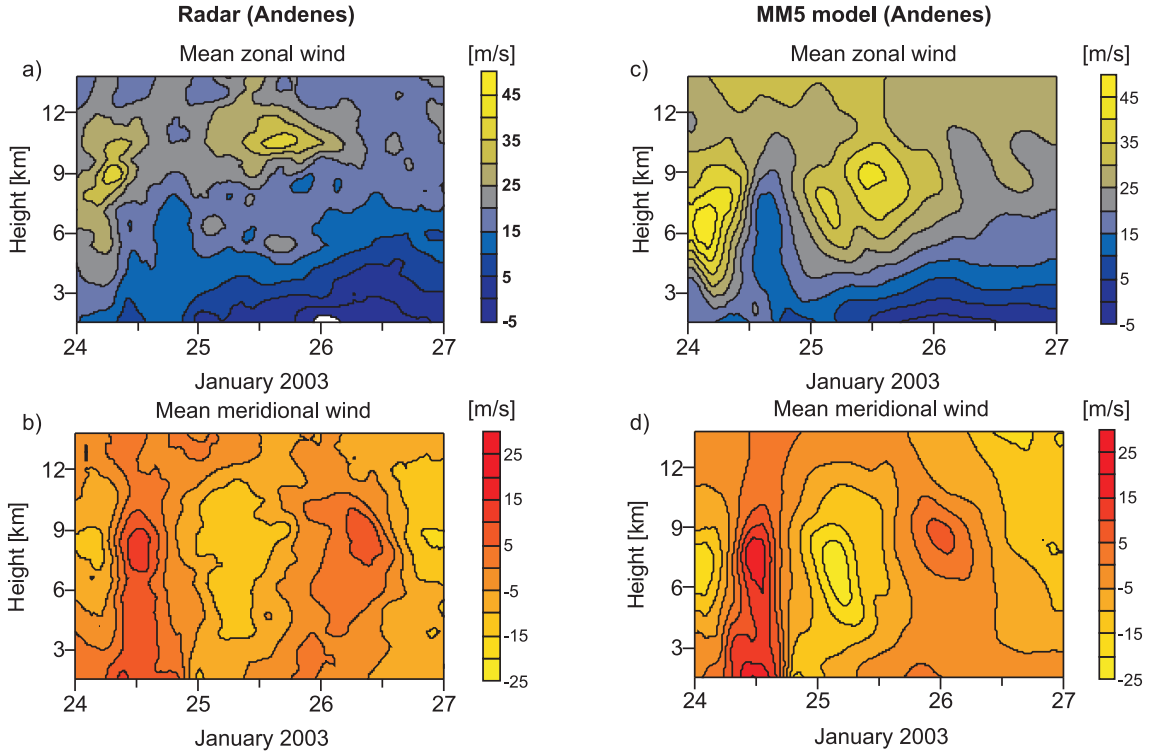


Figure 7.26: Mean zonal and meridional winds at Andenes measured by the radar (a,b) and derived from the MM5 model (c,d) from 24 - 26 January 2003.

The presence of unbalanced flow, either in numerical simulations or in atmospheric data, is typically inferred via various quantities that provide indirect measures of imbalance. One quantity to describe the imbalance is given by the horizontal divergence, which is a measure of the local spreading of a vector field in a horizontal plane. The horizontal divergence is here expressed by zonal and meridional wind fields in Cartesian coordinates

$$\nabla_H \cdot \mathbf{v} = \frac{\partial u}{\partial x} + \frac{\partial v}{\partial y}, \quad (7.5)$$

where u and v are the zonal and meridional components of the vector wind field \mathbf{v} along the horizontal axes x and y , respectively.

As shown in Figure 7.27, the horizontal divergence calculated for 04:00 UT 24 January, 2003 shows clear wave structures over the Scandinavian mountain ridge especially on the Kiruna side.

By application of the wavelet analysis on both, the radar and model data, we found dominant observed periods and vertical wavelengths in zonal and meridional winds. As shown in the wavelet transform of the radar data measured at Andenes (Figure 7.28, left), we derived a significant wave with an observed period of about 13 h (Figure 7.28a) and a vertical wavelength of 4-5 km. Similar structures can also be found in the averaged sum of the wavelet power spectra of the zonal and meridional winds simulated by the model (Figure 7.28c,d). The wavelet spectrum of time series averaged in height (Figure 7.28c) show a significant wave event during 0:00-12:00 UT on 25 January, 2003 with an observed period ~ 13 h, whereas in

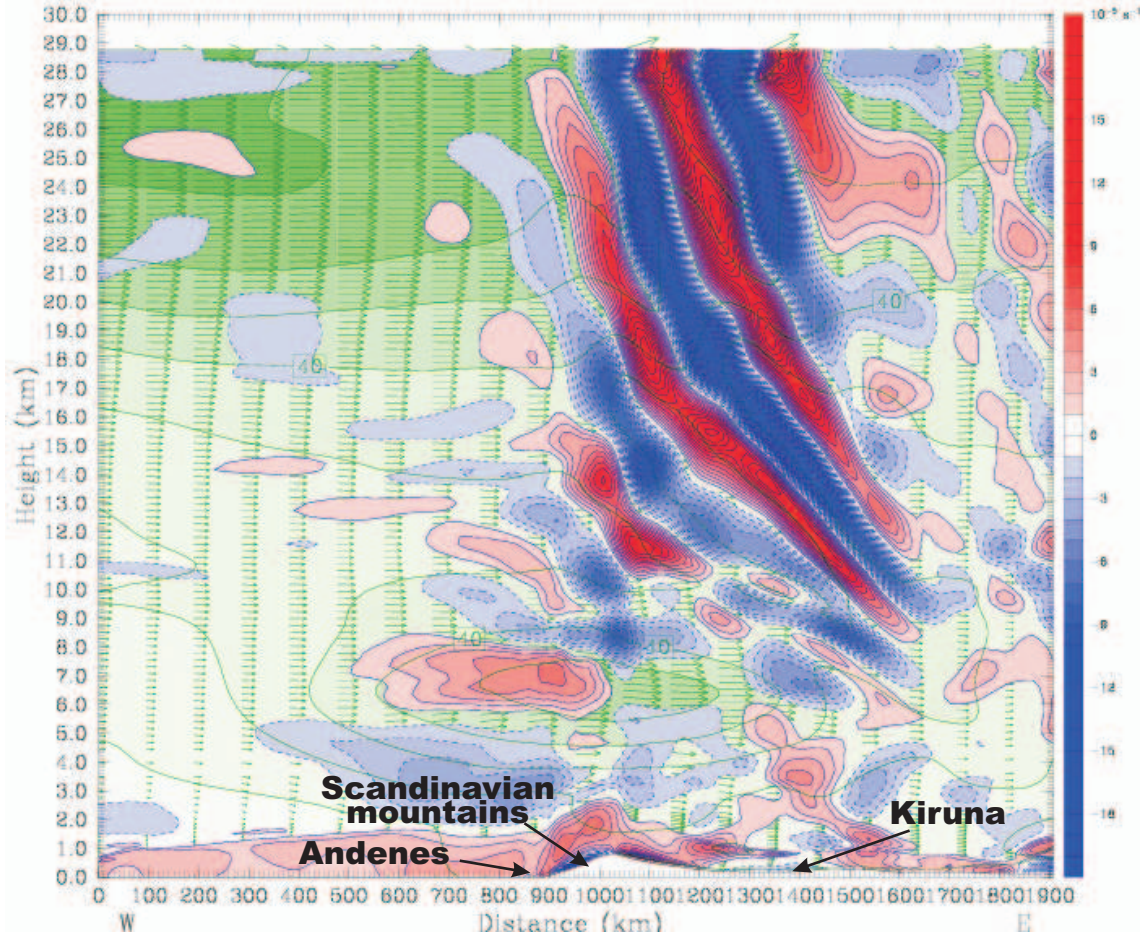


Figure 7.27: Height cross section of the horizontal divergence (red-blue) and mean zonal wind (green) along the line connecting Andenes and Kiruna. (Ch. Zülicke, pers. comm., 2004)

the wavelet spectrum of the vertical profiles of the horizontal winds (Figure 7.28d) averaged in the time, a significant vertical wavelength ~ 5 km has been detected.

Consequently, this information has been used to construct the filter for the estimation of wind perturbations and apply the Stokes parameter estimation for simulated data over the Andenes and Kiruna sides presented in the Table 7.7.

Stokes parameters	Andenes	Kiruna
Degree of polarization, d_{m_1, m_2}	0.77	0.83
Major axis orientation, Θ_{m_1, m_2}	-38°	-43°
Phase difference, δ_{m_1, m_2}	-126.7°	-118.8°
Ellipse axial ratio, R_{m_1, m_2}	0.49	0.59

Table 7.7: Stokes parameters derived from MM5 model output on 25 January 2003 for 1 hours starting from 15:00 UT and averaged in wavelengths from 3.2 km to 9.6 km.

In contrast to the results derived from the radar measurements, we found the maximum energy

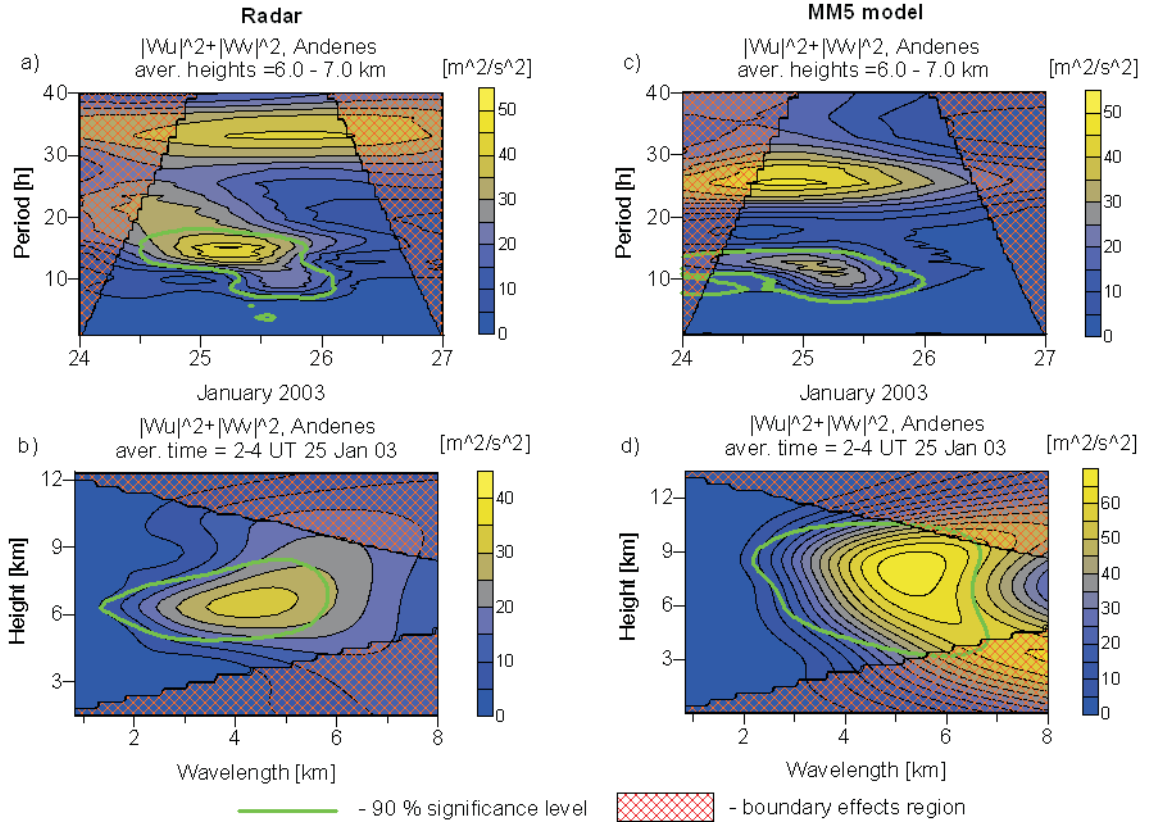


Figure 7.28: The sum of the wavelet spectra applied to the zonal and meridional winds. The upper panel (a, c) shows the Morlet wavelet transform of the time series averaged over the altitude ranges 6 – 7 km. The lower panel (b, d) shows the averaged in time Paul wavelet transforms of vertical profiles of horizontal winds. Radar measurements (a, b) and MM5 model output (c, d) have been used.

in the model data at 15:00-16 UT on 25 January, whereas the radar data showed the peak of the wave activity mostly at 9:00-10:00 UT on 25 January. Possible reasons are connected with internal processes in the model development or with a time resolution of 6 h in the ECMWF data. Also the obtained direction of the wave propagation differs by $\sim 25^\circ$. The final gravity waves parameters estimated by the solution of the Doppler equation (Equation 2.9), dispersion relationship (Equation 2.25) and polarization ellipse equation (Equation 2.10) are given in the Table 7.8.

The analysis of each location leads to a gravity wave with observed period T_{ob} of ~ 13 h and vertical wavelength of ~ 4.8 km. The horizontal wavelength L_h is -642 km and -744 km, and intrinsic period T_{in} is 4.1 h and 4.9 h at Andenes and Kiruna, respectively. The wave has negative vertical group velocity and propagates downward. Thus, it is supposed that this wave is connected to the jet stream in the upper troposphere during 25 January, shown in Figure 7.26.

As a conclusion of this first comparison, we can summarize, that the model analysis partially confirms the results obtained by single radar measurements, except the time, when the peak of the wave activity reaches the maximum. We found similar wave parameters derived from measurements and simulations, but with a time delay of 6 h between the energy maxima.

IGW parameters	Andenes	Kiruna
Mean horizontal wind, \bar{u} , m/s	29.5	25.9
(in the wave propagation direction)		
Wind shear component, $\partial\bar{v}/\partial z$, s^{-1}	$2.7 \cdot 10^{-3}$	$3.3 \cdot 10^{-3}$
Intrinsic period, $2\pi/\hat{\omega}$, h	4.1	4.9
Observed period, $2\pi/\omega_{ob}$, h	13	13
Horizontal wavelength, $2\pi/k$, km	-642	-744
Vertical wavelength, $2\pi/m$, km	4.8	4.8
Horizontal phase velocity, \hat{v}_{ph} , m/s	-43	-41
Vertical phase velocity, \hat{v}_{pz} , m/s	0.3	0.3
Horizontal group velocity, \hat{c}_{gh} , m/s	-3.0	-3.4
Vertical group velocity, \hat{c}_{gz} , m/s	$-22 \cdot 10^{-3}$	$-22 \cdot 10^{-3}$

Table 7.8: Gravity waves parameters derived for the MM5 model output at Andenes and Kiruna using the results of the Stokes-parameter analysis. For comparison with the observational results see Table 7.7 .

7.2.3 Gravity waves during the MaCWAVE/MIDAS campaign in July 2002

A first part of the international MaCWAVE/MIDAS campaign [Goldberg *et al.*, 2003] has been provided in July 2002 at the Andøya Rocket Range near Andenes in Northern Norway, as well as at Esrange facility at Kiruna in Sweden. This part of the project was focused on the gravity wave propagation, instability, and wave-wave and wave-mean flow interaction, especially contributing to the summer mesopause structure and variability [Goldberg *et al.*, 2004]. This campaign involved launches of sounding rockets, meteorological rockets (falling spheres), ground based VHF and MF radars, balloons, and Rayleigh and sodium resonance lidars. For a review on the results of the common investigations in the tropo- and stratosphere, we refer to Schöch *et al.* [2004], and here we will concentrate on the results derived from the radar measurements.

The ALWIN VHF radar in Andenes and ESRAD MST radar in Kiruna were used to investigate the dynamics in the troposphere and lower stratosphere. Wind data are available from the ALWIN radar for the whole period in July 2002, whereas ESRAD data are available from 3 July, 2002, 07:00 UT onward (Figure 7.29).

The radar data were averaged for 30 min intervals to reduce the noise and account for data gaps caused by the alternating mode of measurements in the troposphere and mesosphere. Analyses were then applied to estimate the zonal and meridional wind components from both radar sites. The maximum zonal jet stream reaches the value 25-30 m/s on 4 July, around 22:00 UT, whereas the meridional wind reaches his maximum a little bit later on 5 July at 12:00 UT. To determine the scales of the primary waves, the wavelet transform was used. The sum of wavelet power spectra of the zonal and meridional winds at Andenes are shown in Figure 7.30.

The wavelet transform of time series (Figure 7.30a) shows the presence of different waves during 5 – 6 July with observed periods of about 6 and 10 hours. From the analysis of the

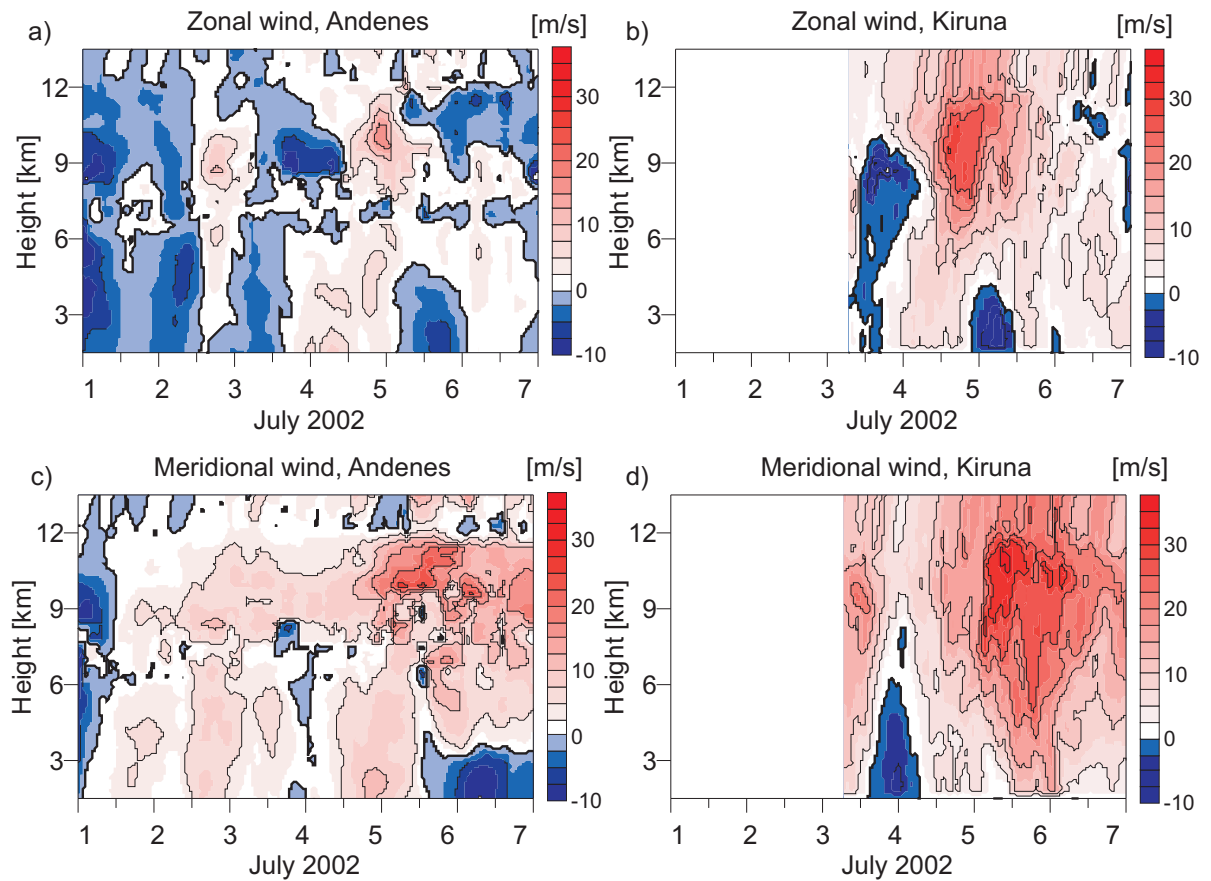


Figure 7.29: Mean zonal and meridional winds measured at Andenes (a,b) and Kiruna (c,d) from 1 - 7 July 2002. The data are smoothed using a low-pass filter with cut off frequencies corresponding to 4h in time and 800m in altitude.

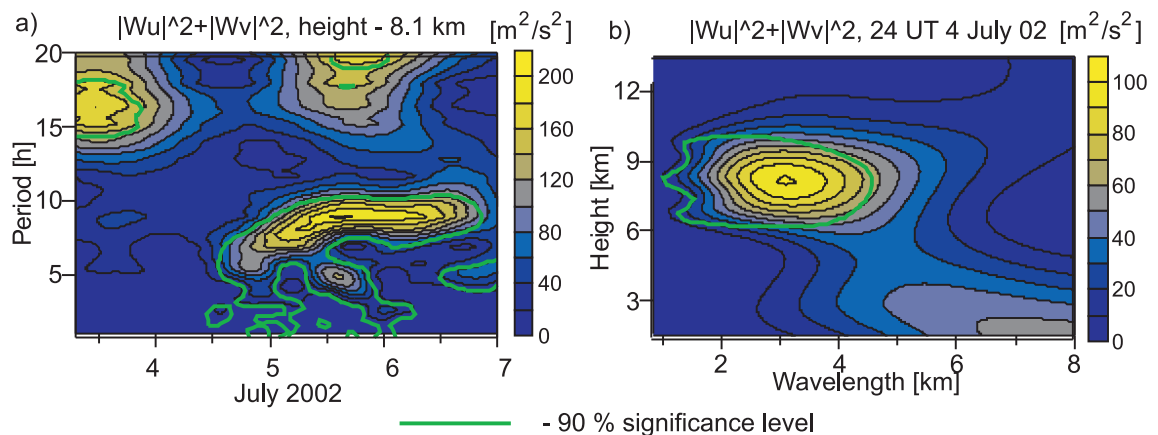


Figure 7.30: The sum of the wavelet spectra applied to the zonal and meridional winds measured at Andenes. The left panel (a) shows the Morlet wavelet transform of the time series. The right panel (b) shows the averaged in time Paul wavelet transforms of vertical profiles of horizontal winds.

vertical wind profiles (Figure 7.30b), we detected a vertical wavelength in the order of 3 km.

The launch schedule for the MaCWAVE/MIDAS campaign is described in detail by *Goldberg et al.* [2004]. The temporal development of the wave structure in the zonal and meridional winds for the first (1–2 July) and second salvo (4–5 July) are shown in Figure 7.31 and Figure 7.32, respectively. The filter bandwidths were selected for waves with periods from 1–12 hours in the time and with vertical wavelengths from 1–4 km.

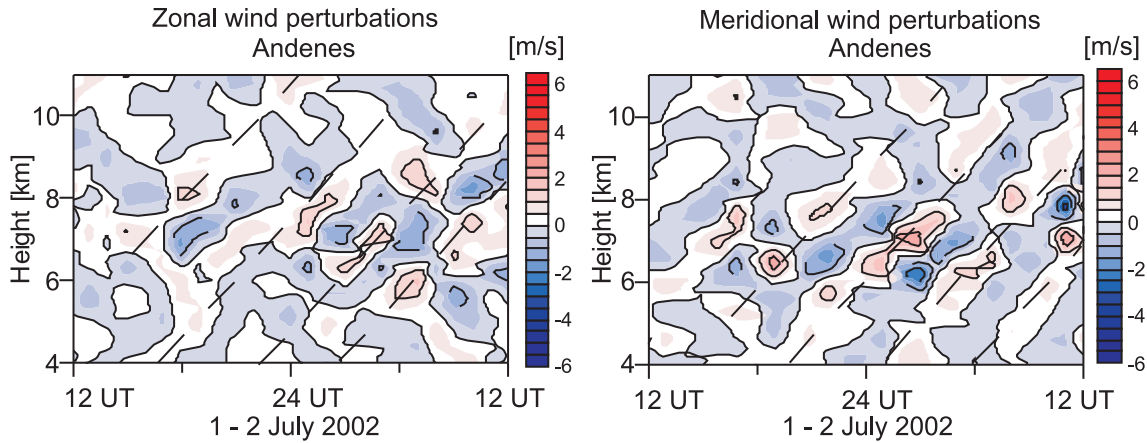


Figure 7.31: Zonal and meridional wind perturbations at Andenes for 1–2 July 2002 after band pass filtering with bandwidths of 1–12 h in time and 1–4 km in height.

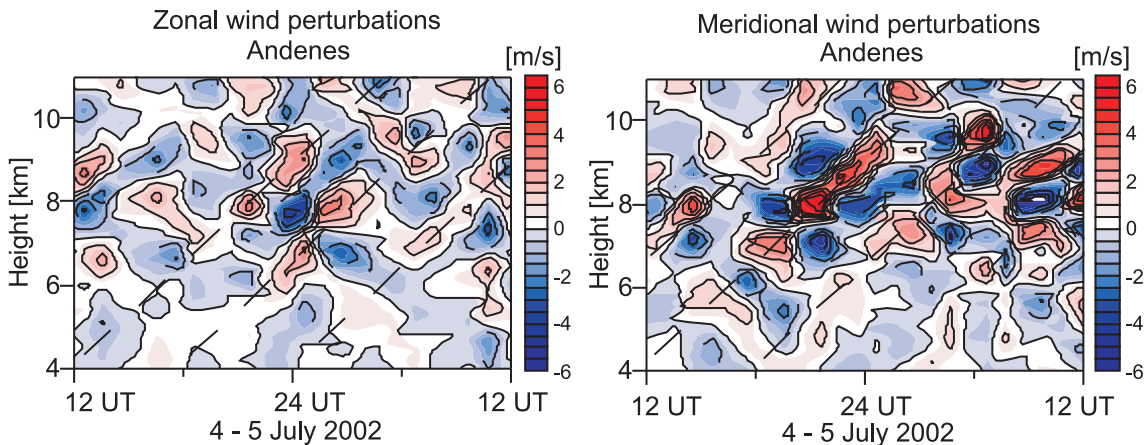


Figure 7.32: Zonal and meridional wind perturbations at Andenes for 4–5 July 2002 after band pass filtering with bandwidths of 1–12 h in time and 1–4 km in height.

During salvo 1, the wave patterns detected in both zonal and meridional wind components show amplitudes up to 2 m/s, whereas during salvo 2, the amplitudes reach values up to 6 m/s in agreement with the larger wave activity in the stratosphere, observed with the RMR lidar [*Schöch et al.*, 2004]. After identifying of similar wave propagation directions with a Stokes-parameter method, the complex cross-spectral analysis of common wave events was performed using the zonal wind perturbations at both radar sites. The cross-spectral analysis (Figure 7.33) shows common wave events at Andenes and Kiruna with coherent observed periods of about 6 hours and 10,6 hours.

From the observed phase differences, horizontal wavelengths of ~ 400 km and ~ 600 km with propagation directions of $\sim 32^\circ$ and $\sim 16^\circ$ have been estimated. The rotary spectra has been applied to the tropospheric height range (3–8.1 km) and averaged for 24 hours starting

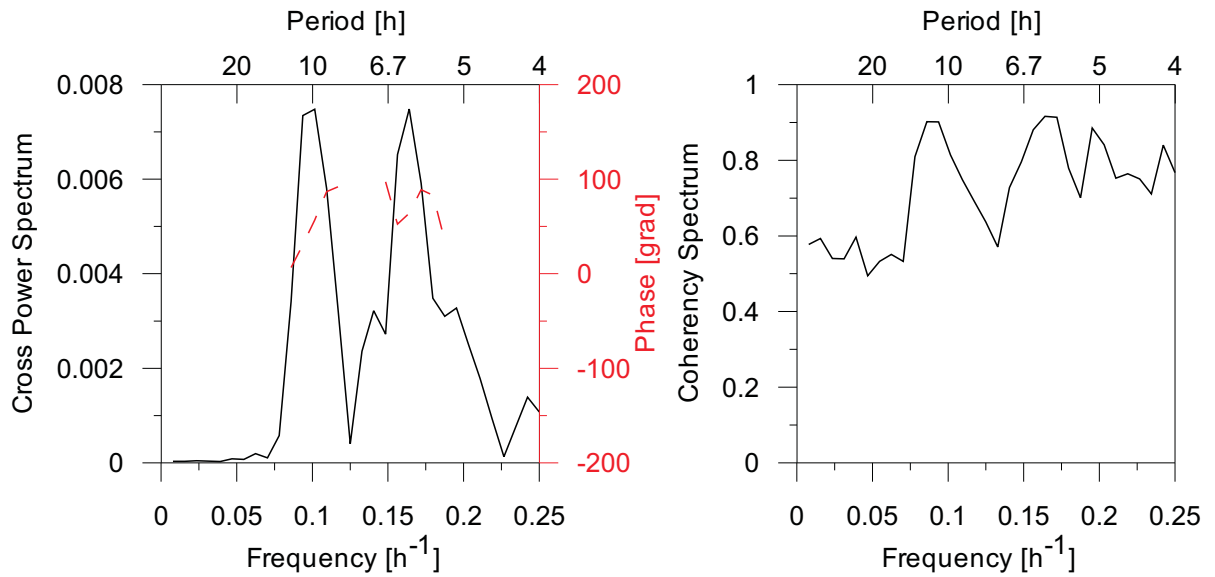


Figure 7.33: Cross-power spectrum between radar measurements at Andenes and Kiruna for the time from 4 July 2002, 0:00 UT to 5 July 2002, 24:00 UT, averaged over the height range from 6.0 km to 8.1 km. Left part: Amplitude (black) and phase difference (red). Right part: Coherency spectrum.

from 4th of July, 12:00 UT. Here we conclude from the Figure 7.34(a) that the shorter wave has a vertical wavelength of ~ 2.7 km and propagates downward while the longer wave has a vertical wavelength of ~ 3.2 km and propagates upward (Figure 7.34b).

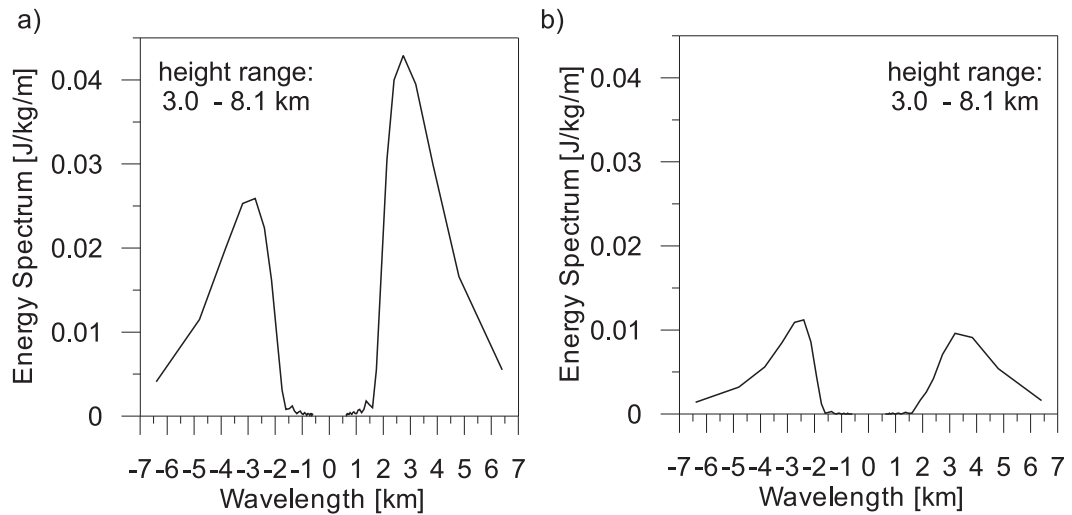


Figure 7.34: Results of the rotary spectra applied to the tropospheric height range 3-8.1 km and averaged for 24 hours starting from 4th of July, 12:00 UT after band pass filtering with bandwidths of 2-8 h in time and 2-4.5 km in height (left) and 8-15 h; 2-4.5 km (right).

Combining all measurements carried out during the summer MaCWAVE/MIDAS campaign [Schöch *et al.*, 2004], we conclude that the excitation level for the short period waves must have been in the troposphere or lower stratosphere region while the long period wave was excited in the troposphere or orographically.

Chapter 8

Long period gravity waves and PMSE

In spite of many experimental and theoretical investigations made during the last years concerning the influence of gravity waves upon the middle atmosphere, a lot of scientific topics and open questions remain. One of them is the connection between gravity waves and the structure of Polar Mesosphere Summer Echoes (PMSE). PMSE are known since their first detection with the Poker Flat radar at 50 MHz in 1979 [Ecklund and Balsley, 1981] as very strong radar echoes occurring at mesospheric heights at polar latitudes during summer conditions in the region of the lowest temperatures of the Earth's atmosphere. These phenomena have been observed at different stations, among others at Andenes (69°N, 16°E) [Bremer *et al.*, 2003], at Tromsø (69°N, 19°E) [Röttger *et al.*, 1988], at Kiruna (68°N, 21°E) [Kirkwood *et al.*, 1998], at Svalbard (78°N, 16°E) [Hall and Röttger, 2001], and also recently in the Southern hemisphere at Davies (69°S, 78°E) [Morris *et al.*, 2004]. One remarkable feature of all PMSE is the fact that the radar echoes often occur in the form of two or more distinct layers that can persist for periods of up to several hours. A typical PMSE with a double layer structure measured with the ALWIN Radar is shown in Figure 8.1. Until now, the layering mechanism leading to these multiple structures is not well understood.

Guided by recently published ideas [Rapp and Lübken, 2003] on the physical origin of PMSE and earlier observations of gravity wave – ice layer interactions [Rapp *et al.*, 2002], micro-physical model simulations [Rapp *et al.*, 2003] have been recently used to consider the impact of wave disturbances on the microphysics of ice particles and to demonstrate an enhanced formation of multiple PMSE layer structures under the influence of temperature and wind variations caused by a long period gravity wave. Model results for the ice charge number density (with temperatures overplotted), and the calculated PMSE-profile after ~ 11 hours simulation time are presented in Figure 8.2, leading to three distinct layers peaking at ~ 83.5 , ~ 88 , and ~ 89.5 km altitude (for details see Hoffmann *et al.* [2005]). Figure 8.2 further shows that the layering occurs because of subsequent nucleation cycles of ice particles in the uppermost (and coldest) gravity wave induced temperature minimum (see Figure 8.2A).

According to model calculations [Rapp *et al.*, 2002], this process should be particularly pronounced in the presence of long period gravity waves, i.e., waves that allow for the "correct" timing between nucleation, growth and sedimentation on the one hand and the phase propagation of the wave on the other.

Here we are testing this model approach with gravity wave characteristics derived from VHF radar wind measurements during PMSE observations carried out with the ALWIN VHF

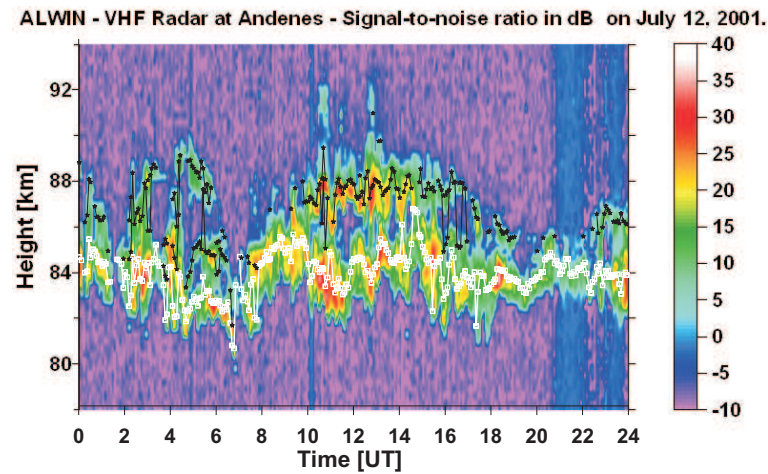


Figure 8.1: Height-time-intensity plot of the backscattered echo power, represented here by the signal-to-noise ratio in dB from measurements with the ALWIN VHF radar at Andenes with the vertically directed beam on July 12, 2001. Identified double layer structures are marked by white and black lines and symbols, respectively. (After *Hoffmann et al.* [2005]).

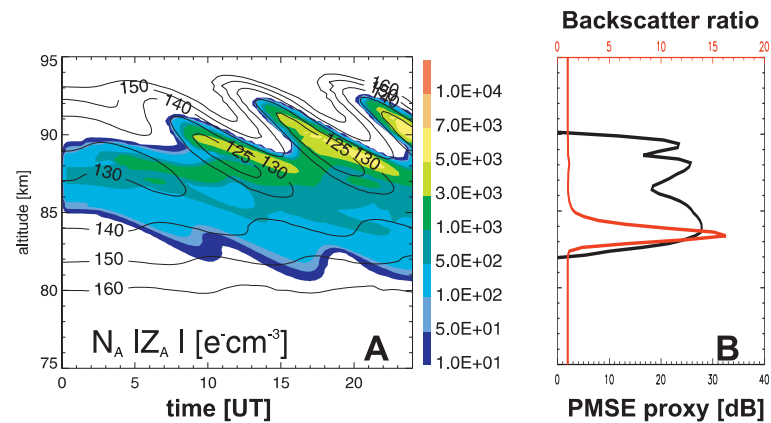


Figure 8.2: Microphysical model results under the influence of a gravity wave with a vertical wavelength of 6 km, a horizontal wavelength of 600 km and an intrinsic period of 470 min. (A) Time-altitude development of ice charge number densities (colored contours) and temperatures (black isolines). (B) Altitude profiles of the PMSE-proxy, estimated from a modelled radar reflectivity (black line), and the backscatter ratio at 532 nm wavelength (red line) after 11 hours of simulated time (Adopted from *Hoffmann et al.* [2005]).

radar [*Latteck et al.*, 1999] in a case study in summer 2001. For a climatologic test of this approach we will determine a daily measure of the kinetic energy of gravity waves estimated for different periods from continuous winds derived from continuous observations with the Andenes-MF-Radar for one PMSE season in order to correlate them with the daily occurrence rate of multiple PMSE layer structures for one PMSE season. Details of the MF Radar at Andenes can be found in *Singer et al.* [1997].

8.1 A case study of gravity waves during PMSE

To confirm this model approach during the PMSE season 2001 we investigate the VHF radar wind measurements during the PMSE observations with a double layer structure for the event already shown in Figure 8.1. The wind perturbations to describe the primary gravity waves and to consider their height and time dependence, were derived using a suitable band pass filter in height and time, whereas the filter parameters itself have been estimated by wavelet transforms (Figure 8.3) of the time series for constant heights and of the wind profiles for constant times, respectively.

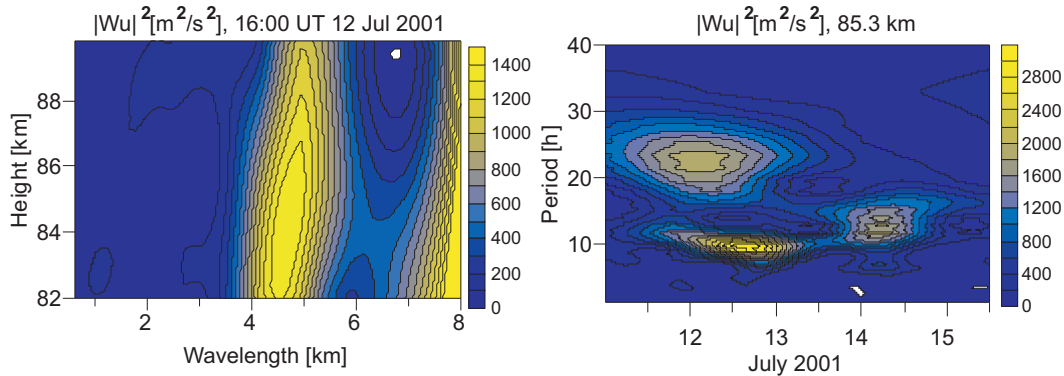


Figure 8.3: Wavelet transform of the zonal wind profiles versus height on 12 July at 16:00 UT (left panel) and wavelet transform of the time series of the zonal winds at the altitude 85.3 km (right panel) of ALWIN VHF radar measurements at Andenes during PMSE.

Based on the filtered data we have applied the hodograph technique (Figure 8.4) on the ALWIN VHF radar wind data on 12 July 2001, 16:00 UT to prove the existence of a gravity wave and to estimate the gravity wave parameters (Table 8.1).

From the ratio of the major to the minor axis of the ellipse, corresponding to the ratio between the intrinsic frequency of the gravity wave to the inertial frequency at $69^\circ N$, we estimate an intrinsic period of ~ 5.8 h. Using this information in the dispersion relation together with the vertical wavelength of 4 km, a horizontal wavelength of ~ 300 km has been estimated.

As shown by the analysis above we found the evidence for a long period gravity wave during the occurrence of a multiple PMSE layer. This confirms the model assumption that the observed multiple PMSE layer structures are mainly caused by the layering of particles in the cold phases of long period gravity waves. Note that we have checked a number of other cases generally leading to similar results as those described above.

IGW parameters	
Intrinsic period, $2\pi/\hat{\omega}$, h	5.8
Horizontal wavelength, $2\pi/k$, km	~ 300
Vertical wavelength, $2\pi/m$, km	4.0

Table 8.1: Gravity waves parameters derived from the from the filtered ALWIN VHF radar measurements.

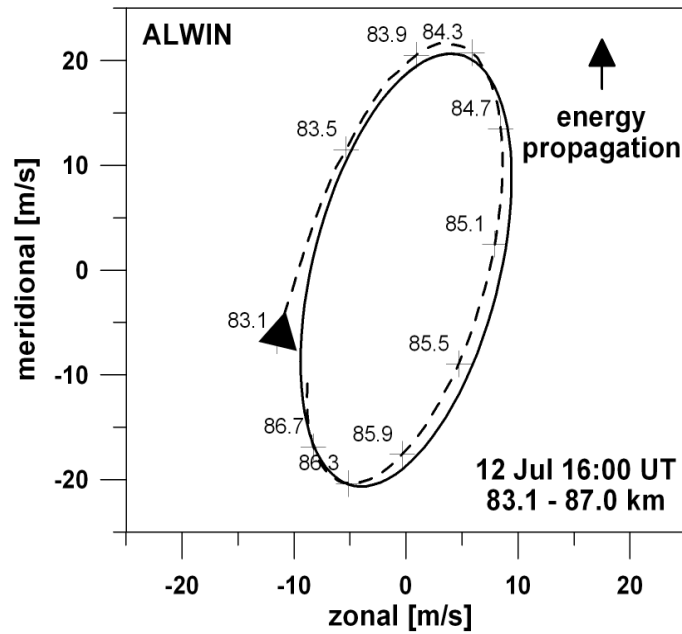


Figure 8.4: Hodograph of the wind perturbations derived from the filtered ALWIN VHF radar measurements between 83.1 and 87.0 km on 12 July 2001, at 16:00 UT. The solid line shows the fitted ellipse, the triangle marks the starting point (After *Hoffmann et al.* [2005]).

8.2 Climatology of gravity waves and multiple PMSE layers

To test the proposed mechanism for the formation of multiple PMSE layers and confirm the idea of the role of long period gravity waves on the formation of multiple PMSE layer structures for a whole summer season 2001, we have determined a mean climatology of gravity wave parameters based on continuous wind measurements with the Andenes-MF-Radar.

In Figure 8.5 we present wind variances estimated with bandwidths of 2 hours for periods from 2–4 h, 3–5 h, ..., 13–15 h, respectively. Here, we used a scale-averaged wavelet power determined by the weighted sum of the wavelet power spectrum over the selected scales [*Torrence and Compo*, 1998]. As expected, the variations at about 12 h, mainly caused by the mean semidiurnal tide, are dominant (Figure 8.5a). A secondary maximum occurs for periods around 6 h, which still persists if we remove the mean tides for the used two months (Figure 8.5b).

Next, we investigate for which period and for which height we receive the strongest correlation between daily values of the variances derived from MF radar winds with the daily occurrence rate of multiple PMSE layers. In Figure 8.6 the correlation coefficients between the daily occurrence rate of multiple PMSE layers and the variances of meridional MF radar winds at different heights are shown for periods from 2–4 h, 3–5 h, ..., 13–15 h, respectively.

The strongest correlation occurs with the variances of meridional winds at 86 km for periods between 5 and 7 h with a correlation coefficient of 0.42 which is significant with more than 99% with the used 61 daily values. This is also confirmed by the scatter-plot in Figure 8.7, where the occurrence of the multiple PMSE layers versus the variance of the meridional wind perturbations, derived for two months (01.06.-30.07.2001) at the height 86 km, is shown. Note, that the slightly weaker negative correlation for periods around 10–12 h in Figure 8.6 is probably caused by the general influence of semidiurnal tides on the variation of PMSE

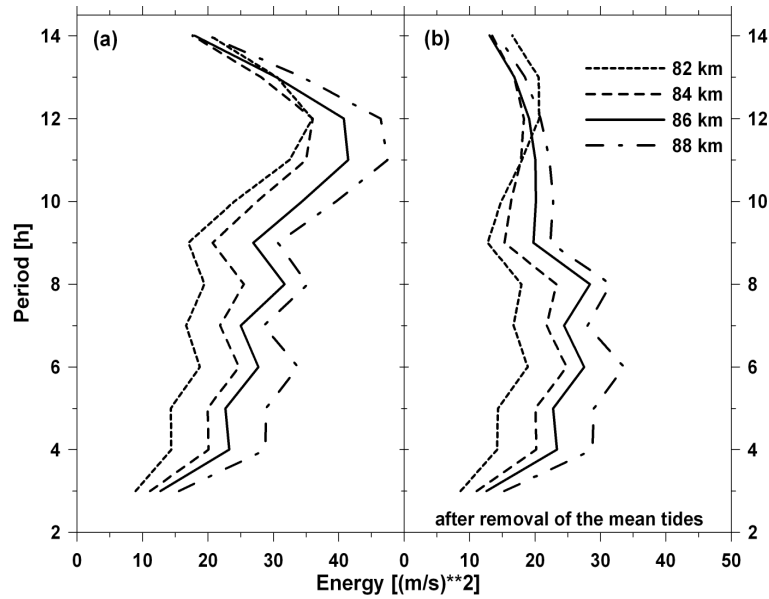


Figure 8.5: Left panel (a): Variances of zonal and meridional winds for periods from 2–4 h, 3–5 h, ..., 13–15 h, derived from MF Radar Andenes at different heights from 01 June – 30 July, 2001; right panel (b): as (a), but after removal of the mean tides estimated for the hole period (After *Hoffmann et al.* [2005]).

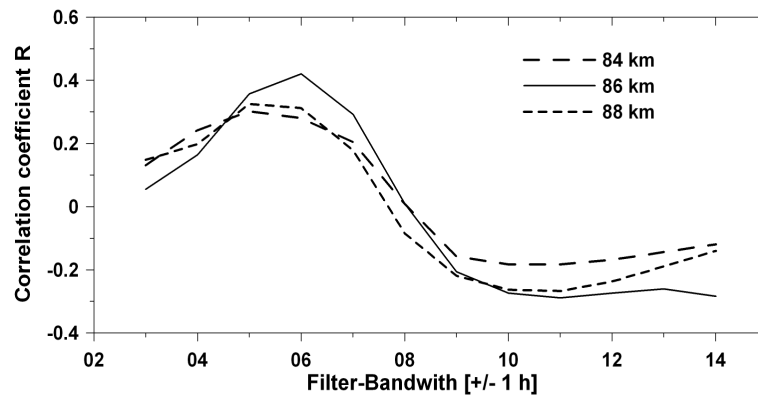


Figure 8.6: Correlation coefficient between daily values of variances of meridional MF radar winds at different heights for periods from 2–4 h, 3–5 h, ..., 13–15 h and the daily occurrence rate of multiple PMSE layers (01 June – 30 July, 2001) (After *Hoffmann et al.* [2005]).

[*Hoffmann et al.*, 1999]. To illustrate the derived connection, Figure 8.8 represents the time series of the daily occurrence rate of multiple PMSE layers during June and July 2001 in comparison with the daily variances of the meridional wind perturbations for periods between 5–7 hours, derived for two month (01.06.–30.07.2001) at the height 86 km.

Summarizing these results, experimental evidence was found to confirm microphysical assumptions that observed multiple PMSE layer structures are mainly caused by layering of ice particles in the cold phases of long period gravity waves, at first in a case study using VHF radar wind measurements during the PMSE observations. Additionally, a climatology

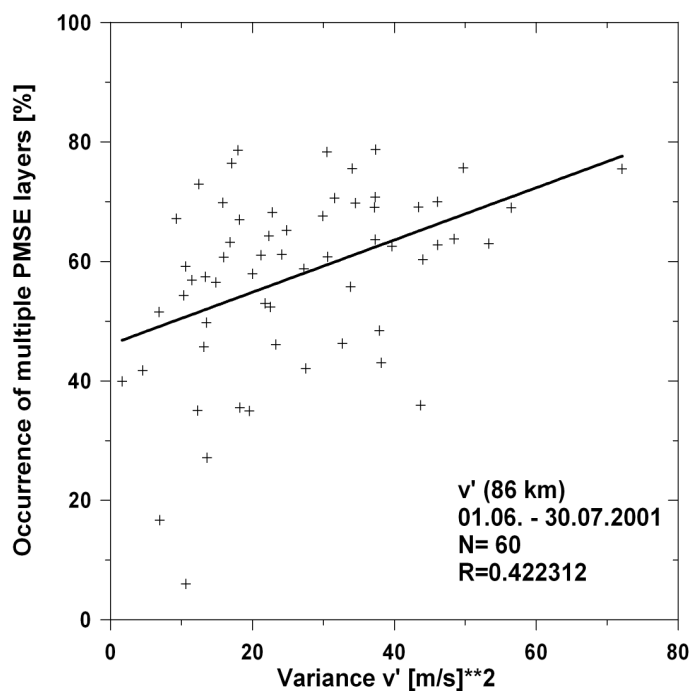


Figure 8.7: Scatter plot of the daily variance of the meridional winds for periods between 5 – 7 h, derived from MF radar measurements in Andenes at the height 86 km, and the daily occurrence rates of multiple PMSE layers during summer 2001.

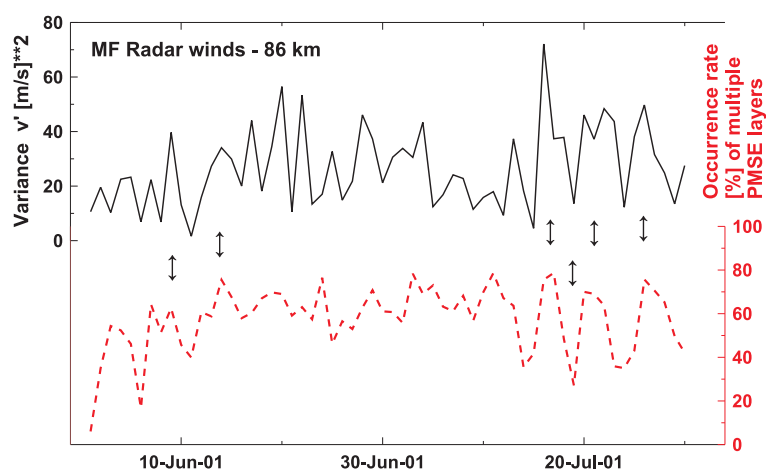


Figure 8.8: Occurrence of the multiple PMSE layers with signal-to-noise ratio > 5 dB (lower panel) and variance of meridional wind perturbations with observed periods 5-7 h (upper panel), derived from MF radar measurements in Andenes at the height 86 km.

of long period gravity waves based on continuous MF radar winds during one PMSE season has been investigated. Here, the strongest correlation between the daily occurrence rate of multiple PMSE layers and the variances estimated for different periods in the fluctuations of the MF radar winds have been found for variances of the meridional winds at an altitude of 86 km derived for periods between 5 – 7 h.

Chapter 9

Summary and Outlook

The knowledge on the generation, propagation and dissipation of gravity waves contributes essentially to the understanding of vertical coupling processes from the troposphere up to mesospheric/lower thermospheric heights due to their ability to transport energy and momentum from the sources to other parts of the atmosphere much faster than by the mean flow.

VHF radars are very useful tools for observations of gravity waves, since they are able to measure continuously 3D winds with height and time resolutions adapted to gravity wave parameters. To identify gravity waves, to consider their height and time dependencies, and to separate simultaneously existing waves, the wavelet analysis has been successfully applied here in combination with matched filter routines. Applying the rotary spectrum, hodograph, and Stokes-parameter spectrum, the main characteristics of gravity waves have been obtained.

All methods were applied in the frame of the two projects, the LEWIZ project in Northern Germany and the MaCWAVE/MIDAS project in Northern Scandinavia. At both places, measurements with two collocated radars separated by about 250 km have been used as a simple case of a radar network to investigate the spatial propagation of gravity waves. In addition to the analyses applicable to single radar data, a cross-spectral analysis has been introduced and applied to identify common waves and to investigate their temporal/spatial differences. With this method, the horizontal wavelength and phase velocity of the propagating waves are directly estimated using only the geometry, the phase differences of coherent waves at both locations, and the mean direction of the wave propagation vector, without additional knowledge on background winds and their changes.

The main objective of the LEWIZ project was to investigate the appearance of strong inertia-gravity waves, their generation and properties in connection with Rossby wave breaking events in a region without orography (Northern Germany). Additionally to the continuous measurements with the OSWIN VHF radar at Kühlungsborn during a first LEWIZ campaign carried out in December 1999, data from a UHF wind profiler at Lindenberg have been used. Based on estimated vertical wavelengths near the tropopause region and the detected dominant observed periods derived from the wavelet transform of the wind measurements at both locations, two types of simultaneously occurring gravity waves have been detected. The first one with an observed period of 11.4 hours shows a downward energy propagation in the troposphere as estimated by rotary spectra as well as hodographs and moves against the background jet stream in the upper troposphere with a characteristic horizontal wavelength of 300 km. Note that this period lies in the range of semidiurnal tidal waves, which practically play no role in the troposphere due to their small amplitudes in comparison to those of the

gravity waves. Further, a secondary less pronounced wave with a horizontal wavelength in the order of about 200 km moving with the wind. These waves show upward directed energy propagations and could be generated by frontal activity or deep convection in the boundary layer of the atmosphere.

In addition, a third possibility to excite secondary gravity waves in the atmosphere by non-linear wave-wave interactions has been proved by the bispectral analysis applied to a case study carried out in February 2002 during another LEWIZ campaign in Kühlungsborn. Here it was found that two waves with different observed periods or vertical wavenumbers were responsible for the appearance of the third gravity wave with a quite different period and vertical wavelength.

In all cases, possible influences of vertical wind shear effects on the dispersion and polarization relation have been considered to estimate all gravity wave characteristics as the intrinsic periods, polarization coefficients, directions of propagation, phase and group velocities.

The cross-spectral analysis between the data of both radars have been used to estimate directly the horizontal wavelengths for waves moving against the jet stream as well as the corresponding phase velocities, which are in good agreement with the results estimated separately at each location.

In the frame of two MaCWAVE/MIDAS-campaigns, in summer 2002 and winter 2003, the generation and propagation of inertia-gravity waves additionally influenced by orographically excited mountain waves over North Scandinavia were investigated with different instruments at the Andøya Rocket Range near Andenes, as well as at the Esrange facilities at Kiruna. Here the continuous measurements of ALWIN VHF Radar at Andenes and Esrange MST radar at Kiruna have been used.

During the summer campaign in July 2002 the wave patterns are detected in both zonal and meridional wind components in the upper troposphere/lower stratosphere (2-15 km). The presence of gravity waves in the stratosphere (20-70 km) during that time is confirmed by a large wave activity observed by measurements with the RMR lidar. After identification of similar wave propagation direction with a Stokes-parameter method, the complex cross-spectral analysis shows that the spectra were similar above Andenes and Kiruna and that the coherence was largest for waves with observed periods of about 6 hours and 10.6 hours.

Combining the measurements from two radars, we found that the excitation level for the short-periodic waves must be in the troposphere or lower stratosphere region while the long-periodic wave was excited in the troposphere or at the boundary layer.

The analyses of the winter campaign in January 2003 applied to the radar measurements at Andenes and Kiruna independently, show the presence of a long horizontal gravity wave with an intrinsic period of 5 h, horizontal and vertical wavelengths in the order of ~650 km and 5 km, respectively. Furthermore, the wave is propagating nearly in the same direction at both locations with a velocity of ~ 40 m/s, and the wave activity is higher on the East-side of the Scandinavian mountain ridge at Kiruna. It has been shown that this gravity wave is originating in the tropopause region in connection with a jet maximum. Additionally, the cross-spectral analysis has been performed confirming the results from independent analyses.

First estimations of the zonal and meridional momentum fluxes confirm the existence of a source for the generation of gravity waves in the jet region in the troposphere. The derived energy propagation is downward in the troposphere and upward in the lower stratosphere. The temporal development of horizontal fluxes and mean-flow accelerations show consistent maxima in agreement with maxima of the wave activity derived with wavelet analyses.

Detailed gravity wave analyses based on mesoscale MM5 model data for the winter MaCWAVE/MIDAS campaign have been used for first comparisons with experimentally obtained results and confirm them partially.

Gravity waves in the mesospheric region play an important role for the explanation of multiple-layered structures of PMSE. A case study carried out with VHF wind radar at Andenes, shows the evidence for a long period gravity wave during the occurrence of multiple PMSE layers. This confirms microphysical model assumptions that the observed multiple PMSE layer structures are mainly caused by the layering of ice particles in the cold phases of long period gravity waves. For a further evidence of this idea, a gravity wave climatology has been investigated based on continuous MF radar winds during one PMSE season. The strongest correlation between the daily occurrence rate of multiple PMSE layers and the variances of the MF radar winds, estimated for different periods, have been found for variances of the meridional winds at an altitude of 86 km derived for periods between 5 – 7 h.

Further investigations should be done in the following directions:

- to understand general structure and dynamics of the atmosphere and its variability it is important to investigate gravity waves from their sources in the troposphere to the lower thermosphere. Due to the experimental methods used often only limited height intervals are analyzed. Using and combining new radar and lidar methods, more continuous observation should be possible;
- to get more reliable results, simultaneous observations and analyses of gravity waves detected by different methods (wind from radar, temperature from lidar, temperature and wind from radiosondes) have to be used. In the past often only one parameter (wind or temperature) has been analyzed;
- to separate pure standing mountain waves by analysis of vertical winds and to investigate their possible interactions with jet induced inertia-gravity waves near the Scandinavian mountain ridge;
- more comparisons between mesoscale model and observations including the estimation of momentum fluxes and the nonlinear wave-wave interaction will improve the detailed analysis of the generation and three-dimensional propagation of gravity waves in the tropo- and lower stratosphere during individual events.

With this thesis we would like to encourage future investigations of gravity wave characteristics by a stronger usage of available networks of atmospheric radars or wind profilers for the investigation of gravity waves, their horizontal wavelengths and phase velocities, their mesoscale behavior, and to improve the statistical reliability of the results.

Appendix A

Linear gravity wave theory

Almost all of theoretical studies of gravity waves are using the linear theory to get a better understanding of the main processes. The simplifications are based on a separation into slowly varying stationary background parts and small first-order perturbations. The background flows often can satisfy these conditions, but in the atmosphere, where many different waves can exist, these constraints may not be strictly applicable and wave-wave interactions may be important (Section 5.5). But the linear theory still can be used for better understanding and to make first-order analysis of observations. The accuracy and practical limitations of the linear theory were examined by *Dörnbrack and Nappo [1997]*.

The derivation of the dispersion relation to describe the connection between the main gravity wave characteristics is based on the solution of the fluid-dynamical equations of motion in an inviscid atmosphere [*Gossard and Hooke, 1975; Holton, 1992; Zink, 2000*]:

$$\begin{aligned}\frac{Du}{Dt} - f_c v &= -\frac{1}{\rho} \frac{\partial p}{\partial x} \\ \frac{Dv}{Dt} + f_c u &= -\frac{1}{\rho} \frac{\partial p}{\partial y} \\ \frac{Dw}{Dt} &= -\frac{1}{\rho} \frac{\partial p}{\partial z} - g,\end{aligned}\tag{A.1}$$

where $\mathbf{v} = \begin{pmatrix} u \\ v \\ w \end{pmatrix}$ is the fluid velocity,

$f_c = 2\Omega \sin \varphi$ is the Coriolis parameter,
with Ω the Earth's angular rotation rate
and φ the latitude of observation,

ρ is the density,

g is the acceleration due to the gravity, and

$\frac{D}{Dt}$ represents differentiation following the motion, i.e. $\frac{D}{Dt} = \frac{\partial}{\partial t} + \mathbf{v}\nabla$.

Equations A.1 are the expressions for momentum in x-,y- and z-directions. The mass continuity equation is

$$\frac{1}{\rho} \frac{\partial \rho}{\partial t} + \frac{\partial u}{\partial x} + \frac{\partial v}{\partial y} + \frac{\partial w}{\partial z} = 0.\tag{A.2}$$

If the advection process is fast enough and does not allow any heat exchange of the advected parcel with its environment, we can use the adiabatic ideal gas equation to close the system of equations

$$\frac{Dp}{D\rho} = \gamma RT, \quad (\text{A.3})$$

where $\gamma = c_p/c_V$ is the ratio of specific heat for constant pressure and constant volume, and R is universal gas constant.

Equation A.3 can be expressed in terms of the potential temperature

$$\Theta = T \left(\frac{p_r}{p} \right)^k, \quad (\text{A.4})$$

where $k = \frac{\gamma-1}{\gamma}$ and p_r is a reference pressure often chosen as 1000 hPa. The potential temperature is the temperature that a parcel would acquire if moved adiabatically to a given reference pressure level p_r . The adiabatic ideal gas equation can be written as

$$\frac{D\Theta}{Dt} = 0. \quad (\text{A.5})$$

The above system of equations is highly nonlinear and very difficult to solve analytically. However, the equations can be linearized and an analytical solution is much easier to achieve, according to

$$\begin{aligned} u &= u_0 + \epsilon u' + \epsilon^2 u'' + \dots \\ v &= v_0 + \epsilon v' + \epsilon^2 v'' + \dots \\ w &= w_0 + \epsilon w' + \epsilon^2 w'' + \dots \\ p &= p_0 + \epsilon p' + \epsilon^2 p'' + \dots \\ \rho &= \rho_0 + \epsilon \rho' + \epsilon^2 \rho'' + \dots, \end{aligned} \quad (\text{A.6})$$

where ϵ is a small ordering parameter. Substituting Equations A.6 into Equations A.1 and A.3

and assuming a background atmosphere with $\mathbf{u}(z) = \begin{pmatrix} u_0 \\ v_0 \\ 0 \end{pmatrix}$ yields the following perturbation equations to first order in ϵ :

$$\frac{Du'}{Dt} + w' \frac{\partial \bar{u}}{\partial z} - f_c v' = -\frac{1}{\rho_0} \frac{\partial p'}{\partial x} \quad (\text{A.7})$$

$$\frac{Dv'}{Dt} + w' \frac{\partial \bar{v}}{\partial z} + f_c u' = -\frac{1}{\rho_0} \frac{\partial p'}{\partial y} \quad (\text{A.8})$$

$$\frac{Dw'}{Dt} = -\frac{1}{\rho_0} \frac{\partial p'}{\partial z} - \frac{\rho'}{\rho_0} g \quad (\text{A.9})$$

$$\frac{D\rho'}{Dt} + w' \frac{\partial \rho_0}{\partial z} + \rho_0 \text{div} \mathbf{u}' = 0 \quad (\text{A.10})$$

$$\frac{Dp'}{Dt} + w' \frac{\partial p_0}{\partial z} - \gamma RT_0 \left(\frac{D\rho'}{Dt} + w' \frac{\partial \rho_0}{\partial z} \right) = 0. \quad (\text{A.11})$$

Substituting wave-like solutions of the form

$$\begin{pmatrix} u' \\ v' \\ w' \end{pmatrix} = \rho_0^{-1/2} \begin{pmatrix} \hat{u} \\ \hat{v} \\ \hat{w} \end{pmatrix} \exp i(kx + ly + mz - \omega t) \quad (\text{A.12})$$

$$\begin{pmatrix} p' \\ \rho' \end{pmatrix} = \rho_0^{1/2} \begin{pmatrix} \hat{p} \\ \hat{\rho} \end{pmatrix} \exp i(kx + ly + mz - \omega t) \quad (\text{A.13})$$

we obtain

$$\begin{aligned} - i\hat{\omega}u' - f_c v' + ikp' &= 0 \\ - i\hat{\omega}v' + f_c u' + ilp' &= 0 \\ - i\hat{\omega}w' + gp' + i \left(m - \frac{i}{2H_p} \right) p' &= 0 \\ - i\hat{\omega} + i \left(m - \frac{i}{2H_p} \right) w' + iku' + ilv' &= 0 \\ - i\hat{\omega} \frac{p'}{c_s^2} + i\hat{\omega}\rho' + \frac{N^2}{g} w' &= 0, \end{aligned} \quad (\text{A.14})$$

where

$$\hat{\omega} = \omega - k\bar{u} - l\bar{v} \quad (\text{A.15})$$

is the intrinsic frequency, i.e. the frequency in a coordinate system moving with the fluid.

$$N^2 = -\frac{g}{\rho_0} \frac{\partial \rho_0}{\partial z} - \frac{g^2}{c_s^2} = \frac{g}{\Theta_0} \frac{\partial \Theta_0}{\partial z} \quad (\text{A.16})$$

is the Brunt-Väisälä frequency,

$$H_p = \frac{1}{\rho_0} \frac{\partial \rho_0}{\partial z} \quad (\text{A.17})$$

the density scale height and

$$c_s = \sqrt{\gamma RT_0} \quad (\text{A.18})$$

the speed of sound. We neglect now the background shear terms in Equations A.7 and A.8 by assuming \bar{u} , \bar{v} , c_s , N , and H_p vary only slowly over a wave cycle in the vertical [Gill, 1982]. Now the dispersion relation can be obtained by setting the determinant of system A.14 to zero:

$$m^2 = \frac{N^2 - \hat{\omega}^2}{\hat{\omega}^2 - f_c^2} (k^2 + l^2) - \frac{1}{4H_p^2} + \frac{\hat{\omega}^2}{c_s^2} \quad (\text{A.19})$$

This equation supports both acoustic and gravity waves. By letting the sound speed $c_s \gg \hat{\omega}$ we can exclude acoustic waves:

$$m^2 = \frac{N^2 - \hat{\omega}^2}{\hat{\omega}^2 - f_c^2} (k^2 + l^2) - \frac{1}{4H_p^2} \quad (\text{A.20})$$

or alternatively for the intrinsic frequency

$$\hat{\omega}^2 = \frac{N^2 (k^2 + l^2) + f_c^2 \left(m^2 + \frac{1}{4H_p^2} \right)}{k^2 + l^2 + m^2 + \frac{1}{4H_p^2}} \quad (\text{A.21})$$

Having obtained the dispersion relation (Equation A.20) by setting the determinant of system A.14 to zero and neglecting the term $\frac{i}{2H_p}$ in the third and fourth equations of A.14 we can now solve the system for the perturbation quantities. The Equations A.22 are the so-called polarization equations, which are relating the perturbation quantities to each other.

$$\begin{aligned} v' &= \frac{l\hat{\omega} - ikf_c}{k\hat{\omega} + ilf_c} u' \\ w' &= -\frac{\hat{\omega}m}{\hat{\omega}k + if_cl} \frac{\hat{\omega}^2 - f_c^2}{N^2 - \hat{\omega}^2} u' \\ \hat{T}' &= \frac{T'}{T_0} = -i \frac{N^2}{g\hat{\omega}w'} = i \frac{N^2 (k^2 + l^2)}{mg} \frac{1}{\hat{\omega}k + if_cl} u'. \end{aligned} \quad (\text{A.22})$$

Appendix B

Structure of the developed software

For the analysis of gravity waves presented in this thesis a software package was developed. The package includes different programs written in IDL (Interactive Data Language, Research Systems Inc.) programming language. The programs realize low-pass filtering, wavelet transform, band-pass filtering of winds measured by radars, as well as estimation of bispectra and vertical fluxes. Using this package different kinds of spectral analysis with a final estimation of gravity wave characteristics are available. The structure of the developed software is shown on the following block-scheme in Figures B.1 and B.2. After each step there is a possibility to save the results in ASCII files or to plot the figures in Postscript files.

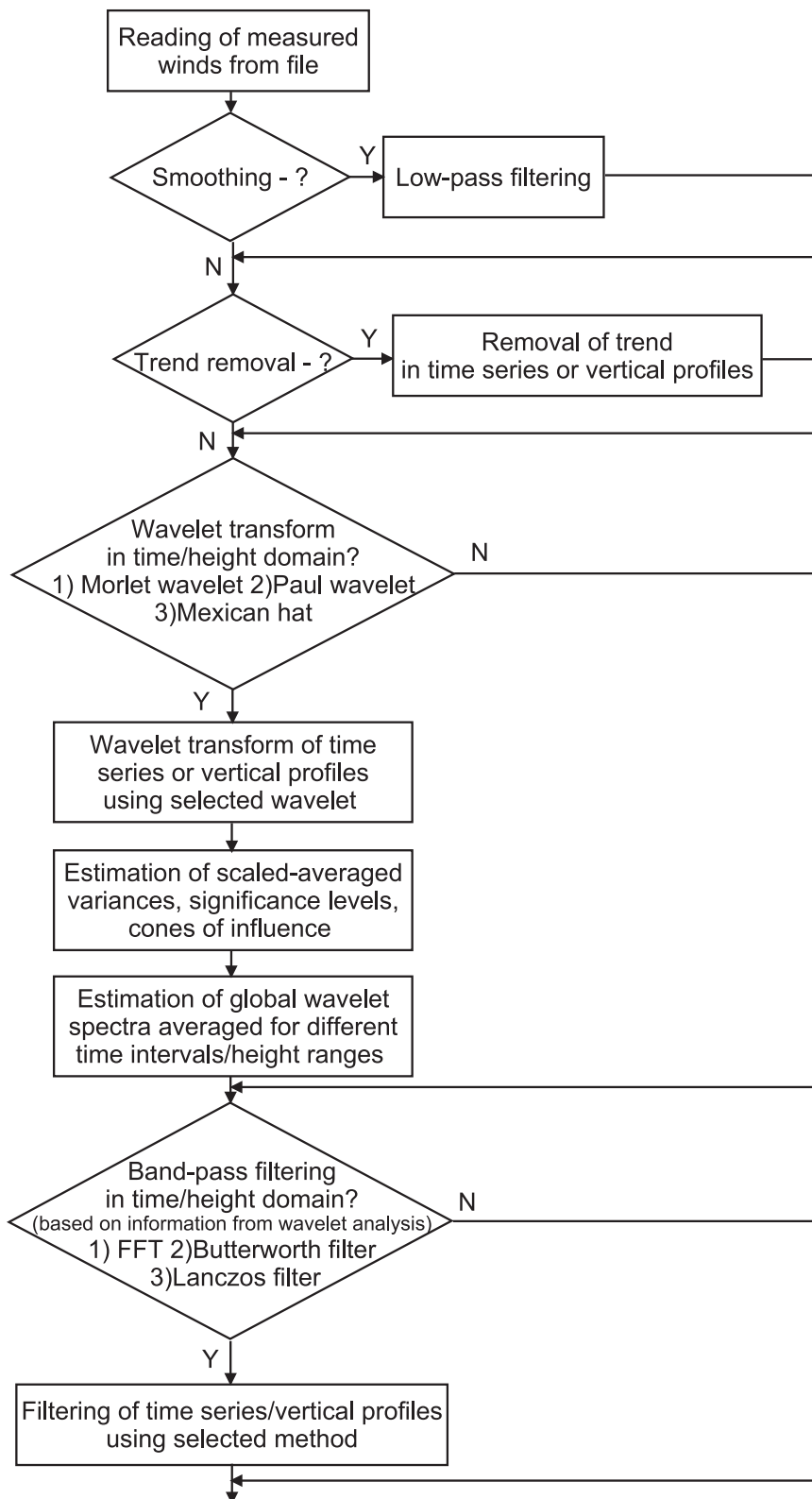


Figure B.1: Block-scheme of the developed software package for gravity waves investigation (Part 1).

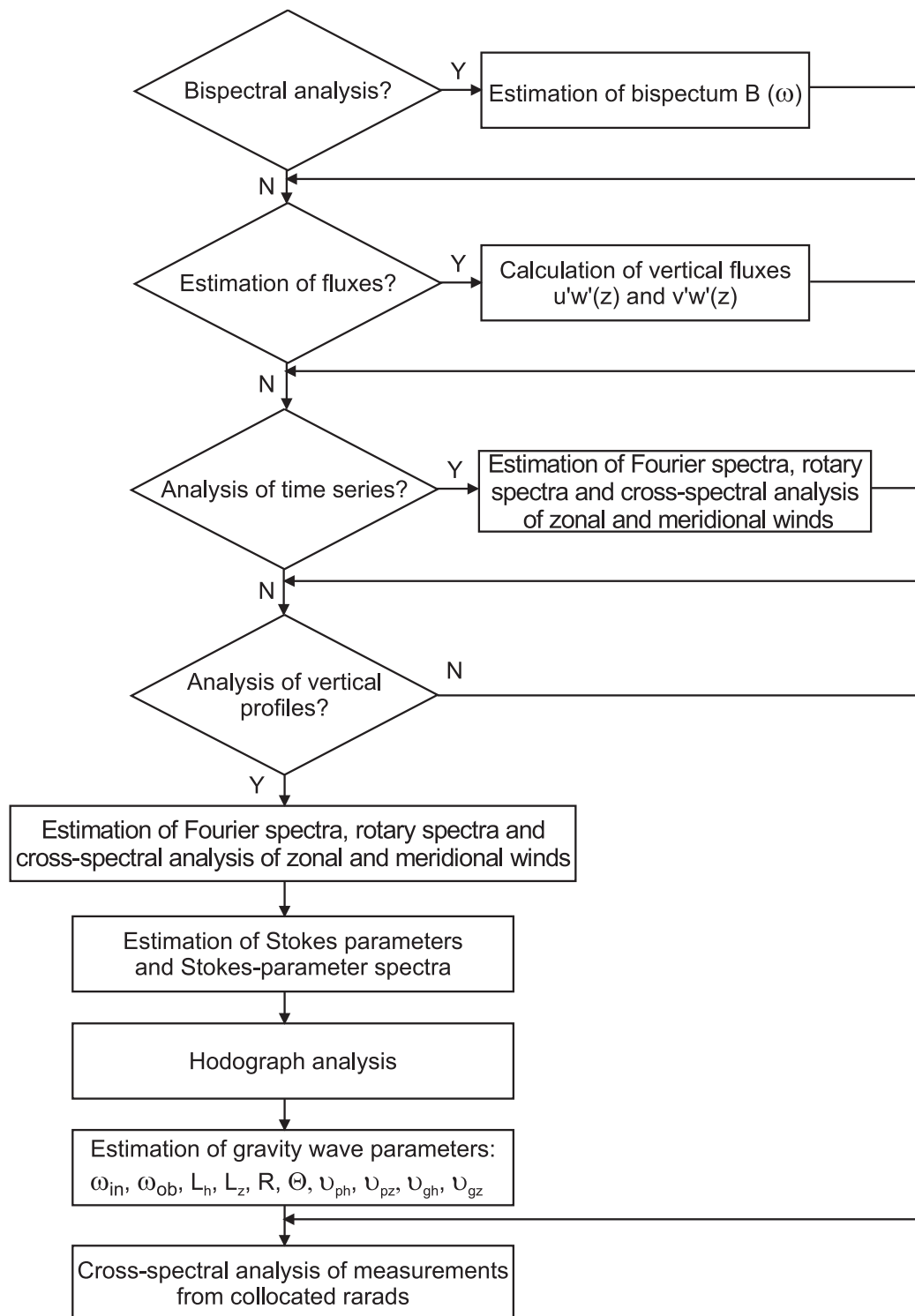


Figure B.2: Block-scheme of the developed software package for gravity waves investigation (Part 2).

Appendix C

Partial list of symbols and abbreviations

α	Angle between radar distance vector and wave propagation vector
β	Angle between the direction of the flux and wave propagation
γ	Ratio of specific heat for constant pressure and constant volume
(ξ, η)	Separation between two signal pattern points on the ground
Θ	Direction of the wave propagation
ρ	Atmospheric density
τ	Time delay
v	Radial velocity
v_d	Line-of-sight component of velocity vector of the target relative to the radar
v_p	Phase velocity
v_{ph}	Observed horizontal phase velocity in direction of wave propagation
\hat{v}_{ph}	Intrinsic horizontal phase velocity in direction of wave propagation
\hat{v}_{pz}	Vertical intrinsic phase velocity
v_{px}	Phase velocity along x -axis
v_{py}	Phase velocity along y -axis
v_{pz}	Phase velocity along z -axis
ϕ	Phase of wave oscillation
φ	Geographical latitude
Ω	Earth's angular rotation rate
ω	Angular wave frequency
ω_{ob}	Observed angular wave frequency
$\hat{\omega}$	Intrinsic wave frequency
a_0	amplitude of wave oscillation

B	Bispectrum
b	Wavelet dilation
c	Speed of light
c_s	Speed of sound
c_g	Group velocity
\hat{c}_{gh}	Intrinsic horizontal group velocity in direction of wave propagation
\hat{c}_{gz}	Vertical intrinsic group velocity
c_{gh}	Horizontal group velocity in direction of wave propagation
c_{gx}	Group velocity for x -direction
c_{gy}	Group velocity for y -direction
c_{gz}	Group velocity for z -direction
d	Degree of wave polarization
E	Total energy
\vec{F}	Eliassen-Palm flux
f	Frequency
f_c	Coriolis parameter
f_d	Doppler frequency shift of echoes from a moving target relative to the radar
G_{morlet}, G_{paul}	Fourier representation of the Morlet and Paul wavelets
g	Acceleration of gravity
g_{morlet}, g_{paul}	Time representation of the Morlet and Paul wavelets
H	Heaviside step function
H_p	Density scale height
I, D, P, Q	Stokes parameters: total variance, axial anisotropy, "in phase" covariance, "in quadrature" covariance
i	Complex unit value, $i = \sqrt{-1}$
\vec{k}	Total wave vector
k	Zonal wavenumber
k_h	Horizontal wavenumber, $k_h = \sqrt{k^2 + l^2}$
L	Wavelength
L_h	Horizontal wavelength
L_x	Projection of L in x direction
L_y	Projection of L in y direction
L_z	Projection of L in z direction
l	Meridional wavenumber

m	Vertical wavenumber
N	Brunt-Väisälä frequency
p	Pressure
p'	Pressure perturbations
\hat{p}	Amplitude of pressure perturbations
p_0	Mean pressure
p_r	Reference pressure often chosen as 1000 hPa
R	Polarization ellipse ratio
\vec{r}	Distance vector, $\vec{r} = \vec{x} + \vec{y} + \vec{z}$
\vec{S}	Distance vector between both radars
s	Wavelet scale
T	Absolute temperature
T'	Temperature perturbations
\hat{T}'	Normalized temperature perturbations, $\hat{T}' = \frac{T'}{T_0}$
T_{in}	Intrinsic period
T_{ob}	Observed period
t	Time
U	Fourier transform of zonal wind
U_R	Real part of spectra of zonal wind
U_I	Imaginary part of spectra of zonal wind
u	zonal wind
\mathbf{u}	Total mean wind, $\mathbf{u} = (u, v, w)$
u_h	Horizontal wind in direction of wave propagation
u_0	Mean zonal wind
\bar{u}	Mean horizontal wind component parallel to wave propagation
u'	Zonal wind perturbations
\hat{u}	Amplitude of zonal wind perturbations
V	Fourier transform of meridional wind
V_R	Real part of spectra of meridional wind
V_I	Imaginary part of spectra of meridional wind
v	Meridional wind
$\mathbf{v} = (v_x, v_y, v_z)$	Wind velocity vector at a given height
v_0	Mean meridional wind
\bar{v}	Mean horizontal wind component perpendicular to wave propagation

v'	Meridional wind perturbations
\hat{v}	Amplitude of meridional wind perturbations
W	Wavelet transform
w	Vertical wind
w_0	Mean vertical wind
w'	Vertical wind perturbations
\hat{w}	Amplitude of vertical wind perturbations

ALWIN	ALOMAR wind radar
ATRAD	Atmospheric Radar Systems Pty. Ltd, Thebarton, S.A., Australia
CIRA	COSPAR International Reference Atmosphere
DBS	Doppler Beam Swinging method
DWD	Deutscher Wetterdienst (German)
ECMWF	European Center for Medium-range Weather Forecasts
ESRAD	Esrangle MST radar
FCA	Full Correlation Analysis
FFT	Fast Fourier Transform
GPS	Global Positioning System
GCM	General Circulation Model
HF	High Frequency
IGW	Inertia-Gravity Waves
KE	Kinetic energy
LEWIZ	Letzter Winter im Zwanzigsten Jahrhundert (German)
Lidar	LIght Detection And Ranging
MaCWAVE	Mountain and Convective Waves Ascending Vertically
MIDAS	Middle Atmosphere Dynamics and Structure
MF	Medium Frequency
MLT	Mesosphere/Lower Thermosphere
MM5	Fifth-Generation NCAR / Penn State Mesoscale Model
MST	Mesosphere Stratosphere Troposphere
NCEP	National Center for Environmental Prediction
NLC	Noctilucent Clouds

NCAR	National Center for Atmospheric Research
OSWIN	Ostsee Wind radar
PE	Potential energy
PMSE	Polar Mesosphere Summer Echoes
QPC	Quadratic Phase Coupling
RASS	Radio Acoustic Sounding System
TEM	Transformed Eulerian Mean
UHF	Ultra High Frequency
UT	Universal Time
VHF	Very High Frequency

Bibliography

- Alexander, M. J., and J. R. Holton, On the spectrum of vertically propagating gravity waves generated by a transient heat source, *Atmos. Chem. Phys. Discuss.*, *4*, 923–932, 2004.
- Allen, S. J., and R. A. Vincent, Gravity wave activity in the lower atmosphere: Seasonal and latitudinal variations, *J. Geophys. Res.*, *100*, 1327–1350, 1995.
- Alpers, M., R. Eixmann, C. Fricke-Begemann, M. Gerding, and J. Höffner, Temperature lidar measurements from 1 to 105 km altitude using resonance, Rayleigh, and Rotational Raman scattering, *Atmos. Chem. Phys.*, *4*, 793–800, 2004.
- Andrews, D. G., and M. E. McIntyre, Planetary waves in horizontal and vertical shear: The generalized Eliassen-Palm relation and the mean zonal acceleration, *J. Atmos. Sci.*, *33*, 2031–2048, 1976.
- Andrews, D. G., and M. E. McIntyre, Generalized Eliassen-Palm and Charney-Drazin theorems for waves on axisymmetric mean flows in compressible atmospheres, *J. Atmos. Sci.*, *35*, 175–185, 1978.
- Atlas, D. (Ed.), *Radar in meteorology: Battan Memorial and 40th anniversary radar meteorology conference*, American Meteorological Society, Boston, 1990.
- Balsley, B. B., and K. S. Gage, The MST radar technique: Potential for middle atmospheric studies, *Pure Appl. Geophys.*, *118*, 452–493, 1980.
- Battan, L. J., *Radar observation of the atmosphere*, The University of Chicago Press, Chicago, 1973.
- Beard, A. G., N. J. Mitchell, P. J. S. Williams, and M. Kunitake, Non-linear interactions between tides and planetary waves resulting in periodic tidal variability, *J. Atmos. Solar Terr. Phys.*, *61*, 363–376, 1999.
- Böhme, T., T. Hauf, and V. Lehmann, Investigation of short-period gravity waves with the Lindenberg 482 MHz tropospheric wind profiler, *Quart. J. R. Met. Soc.*, *130*, 2933–2952, 2004.
- Bremer, J., P. Hoffmann, R. Latteck, and W. Singer, Seasonal and long-term variations of PMSE from VHF radar observations at Andenes, Norway, *J. Geophys. Res.*, *108(D8)*, 8438, doi:10.1029/2002JD002369, 2003.
- Briggs, B. H., The analysis of spaced sensor records by correlation techniques, in *Handbook for MAP*, vol. 13, edited by R. A. Vincent, pp. 166–186, SCOSTEP Secretariat, University of Illinois, 1984.

- Briggs, B. H., Observations of atmospheric dynamics using radar techniques, *AUJP*, 46, 127–147, 1993.
- Briggs, B. H., G. J. Phillips, and D. H. Shinn, The analysis of observations on spaced receivers of the fading of radio signals, *PPSL*, B63(2), 106–121, 1950.
- Buss, S., A. Herzog, C. Hostettler, T. P. Bui, D. Lüthi, and H. Wernli, Analysis of a jet stream induced gravity wave associated with an observed stratospheric ice cloud over Greenland, *Atmos. Chem. Phys.*, 4, 1183–1200, 2004.
- Carter, D. A., B. B. Balsley, W. L. Ecklund, K. S. Gage, A. C. Riddle, R. Garelo, and M. Crochet, Investigation of internal gravity waves using three vertically directed closely spaced wind profiler, *J. Geophys. Res.*, 94, 8633–8642, 1989.
- Chilson, P. C., S. Kirkwood, and A. Nilsson, The Esrange MST radar: A brief introduction and procedure for range validation using balloons, *Radio Sci.*, 34(2), 427–436, 1999.
- Chimonas, G., The stability of a coupled wave-turbulence system in a parallel shear flow, *Boundary-Layer Meteorol.*, 2, 444–452, 1972.
- Chimonas, G., and C. J. Nappo, A thunderstorm bow wave, *J. Atmos. Sci.*, 44, 533–541, 1987.
- Chimonas, G., and C. J. Nappo, Wave drag in the planetary boundary layer over complex terrain, *Boundary-Layer Meteorol.*, 47, 217–232, 1989.
- Cho, J., Inertio-gravity wave parameter estimation from cross-spectral analysis, *J. Geophys. Res.*, 100, 18,727–18,737, 1995.
- Clark, R. R., and J. S. Bergin, Bispectral analysis of mesosphere winds, *J. Atmos. Solar Terr. Phys.*, 59, 629–639, 1997.
- Clark, T. E., and T. H. J. Kuettner, Convectively forced internal gravity waves: Results from a two-dimensional numerical experiments, *Quart. J. R. Met. Soc.*, 112, 899–925, 1986.
- Clark, T. L., and W. R. Peltier, On the evolution and stability of finite amplitude mountain waves, *J. Atmos. Sci.*, 34, 1715–1730, 1977.
- Cot, C., and J. Barat, Wave-turbulence interaction in the stratosphere: A case study, *J. Geophys. Res.*, 91, 2749–2756, 1986.
- Dörnbrack, A., and C. J. Nappo, A note on the application of linear wave theory at a critical level, *Boundary-Layer Meteorol.*, 82, 399–416, 1997.
- Dörnbrack, A., T. Birner, A. Fix, H. Flentje, A. Meister, H. Schmid, E. Browell, and M. Mahoney, Evidence for inertia gravity waves forming polar stratospheric clouds over Scandinavia, *J. Geophys. Res.*, 197(D20), 8287, doi:10.1029/2001JD000452, 2002.
- Doviak, R. J., and D. S. Zrnic, *Doppler radar and weather observations*, Academic Press, New York, 1984.
- Dudhia, J., A nonhydrostatic version of the Penn State-NCAR mesoscale model: Validation tests and simulation of an atlantic cyclone and cold front, *Mon. Weather Rev.*, 121, 1493–1513, 1993.

- Dunkerton, T. J., On the mean meridional mass motions in the stratosphere and mesosphere, *J. Atmos. Sci.*, *35*, 2325–2333, 1978.
- Eckermann, S., Hodographic analysis of gravity waves: Relationships among Stokes parameters, rotary spectra and cross-spectral methods, *J. Geophys. Res.*, *101*, 19,169–19,174, 1996.
- Eckermann, S., and R. Vincent, Falling sphere observations gravity waves motions in the upper stratosphere over Australia, *Pure Appl. Geophys.*, *130*, 509–532, 1989.
- Eckermann, S. D., I. Hirota, and W. K. Hocking, Gravity wave and equatorial wave morphology of the stratosphere derived from long-term rocket soundings, *Quart. J. R. Met. Soc.*, *121*, 149–186, 1995.
- Ecklund, W. L., and B. B. Balsley, Long-term observations of the Arctic mesosphere with the MST radar at Poker Flat, Alaska, *J. Geophys. Res.*, *86*, 7775–7780, 1981.
- Ecklund, W. L., B. B. Balsley, D. A. Carter, A. C. Riddle, M. Crochet, and R. Garello, Observations of vertical motions in the troposphere and lower stratosphere using three closely spaced ST radars, *Radio Sci.*, *20*, 1196–1206, 1985.
- Einaudi, F., and J. J. Finnigan, The interaction between an internal gravity wave and the planetary boundary layer. Part I: The linear analysis, *Quart. J. R. Met. Soc.*, *107*, 793–806, 1981.
- Eliassen, A., and E. Palm, On the transfer of energy in stationary mountain waves, *Geofysiske Publikasjoner*, *22(3)*, 1–23, 1961.
- Farge, M., Wavelet transforms and their applications to turbulence, *Annu. Rev. Fluid Mech.*, *24*, 395–457, 1992.
- Finke, U., Wechselwirkung zwischen hochreichender Konvektion und kurzperiodischen Schwerkwellen, Ph.D. thesis, Universität München, Germany, 1995.
- Fritts, D. C., Gravity wave saturation in the middle atmosphere: A review of theory and observations, *Rev. Geophys. Space Phys.*, *22*, 275–308, 1984.
- Fritts, D. C., A review of gravity wave saturation processes, effects, and variability in the middle atmosphere, *Pure Appl. Geophys.*, *130*, 343–317, 1989.
- Fritts, D. C., and M. J. Alexander, Gravity wave dynamics and effects in the middle atmosphere, *Rev. Geophys.*, *41(1)*, 1003, doi:10.1029/2001RG000106, 2003.
- Fritts, D. C., and T. E. VanZandt, Spectral estimates of gravity wave energy and momentum fluxes. Part I: Energy dissipation, acceleration and constraints, *J. Atmos. Sci.*, *50*, 3685–3694, 1993.
- Fritts, D. C., and R. A. Vincent, Mesospheric momentum flux studies at Adelaide, Australia: Observations and a gravity wave-tidal interaction model, *J. Atmos. Sci.*, *44(3)*, 605–619, 1987.
- Fritts, D. C., U.-P. Hoppe, and B. Inhester, A study of the vertical motion field near the high-latitude mesopause during MAC-SINE, *J. Atmos. Terr. Phys.*, *52*, 927–938, 1990.

- Fua, D., G. Chimonas, F. Einaudi, and O. Zeman, An analysis of wave-turbulence interaction, *J. Atmos. Sci.*, *39*, 2450–2463, 1982.
- Gage, K. S., and B. B. Balsley, On the scattering and reflection mechanisms contributing to clear air radar echoes from the troposphere, stratosphere, and mesosphere, *Radio Sci.*, *15*, 243–257, 1980.
- Gage, K. S., B. B. Balsley, and J. L. Green, Fresnel scattering model for the specular echoes observed by VHF radar, *Radio Sci.*, *16*, 1447–1453, 1981.
- Geller, M. A., Dynamics of the middle atmosphere, *Space Sci. Rev.*, *34*, 359–375, 1983.
- Gill, A. E., *Atmosphere-Ocean Dynamics*, Academic Press, New York, 1982.
- Goldberg, R., et al., The MaCWAVE program to study gravity wave forcing of the polar mesosphere during summer and winter, in *Proceedings of the 16th ESA Symposium on European Rocket and Balloon Programmes and Related Research, St. Gallen, Switzerland (ESA SP-530)*, edited by B. Warmbein, pp. 345–350, ESA Publications Division, 2003.
- Goldberg, R., et al., The MaCWAVE/MIDAS rocket and ground-based measurements of polar summer dynamics: Overview and mean state structure, *Geophys. Res. Lett.*, *31*, L24S02, doi:10.1029/2004GL019411, 2004.
- Goody, R. M., and Y. L. Yung, *Atmospheric radiation; theoretical basis*, 2 ed., Oxford University Press, 1989.
- Gossard, E. E., and W. H. Hooke, *Waves in the atmosphere*, Elsevier, New York, 1975.
- Gossard, E. E., and W. Munk, On gravity waves in the atmosphere, *J. Meteorol.*, *11*, 259–269, 1954.
- Grell, G., J. Dudhia, and D. R. Stauffer, *A description of the fifth-generation Penn-State/NCAR mesoscale model (MM5)*, Technical Report TN-398+IA, NCAR, 1994.
- Guest, F. M., M. J. Reeder, C. J. Marks, and D. J. Karoly, Inertia-gravity waves observed in the lower stratosphere over Macquarie Island, *J. Atmos. Sci.*, *57*, 737–752, 2000.
- Gurvich, A., A. Kon, and V. Tatarskii, Scattering of electromagnetic waves on sound in connection with problems of atmospheric sounding (review), *Radiophys. Quant. Electron.*, *30*, 347–366, 1987.
- Hall, C. M., and J. Röttger, Initial observations of Polar Mesospheric Summer Echoes using the EISCAT Svalbard radar, *Geophys. Res. Lett.*, *28*, 131–134, 2001.
- Hauf, T., U. Finke, J. Neisser, G. Bull, and J.-G. Stangenberg, A ground-based network for atmospheric pressure fluctuations, *J. Atmos. Ocean. Techn.*, *13*, 1001–1023, 1996.
- Hertzog, A., C. Souprayen, and A. Hauchecorne, Observation and backward trajectory of an inertio-gravity wave in the lower stratosphere, *Ann. Geophysicae*, *19*, 1141–1155, 2001.
- Hines, C. O., Internal atmospheric gravity waves at ionospheric heights, *Can. J. Phys.*, *38*, 1441–1481, 1960.
- Hines, C. O., *The Upper Atmosphere in Motion*, AGU, Washington, D.C., 1974.

- Hines, C. O., A modeling of atmospheric gravity waves and wave drag generated by isotropic and anisotropic terrain, *J. Atmos. Sci.*, *45*, 309–322, 1988.
- Hines, C. O., Tropopausal mountain waves over Arecibo: A case study, *J. Atmos. Sci.*, *46*, 476–488, 1989.
- Hines, C. O., Doppler-spread parameterization of gravity-wave momentum deposition in the middle atmosphere. Part I: Basic formulation, *J. Atmos. Solar Terr. Phys.*, *59*, 371–386, 1997.
- Hinich, M. J., and C. S. Clay, The application of the discrete fourier transform in the estimation of power spectra, coherence and bispectra of geophysical data, *Rev. Geophys.*, *6*, 347–363, 1968.
- Hocking, W. K., S. Fukao, T. Tsuda, M. Yamamoto, T. Sato, and S. Kato, Aspect sensitivity of stratospheric VHF radio wave scatters, particularly above 15-km altitude, *Radio Sci.*, *25*, 613–627, 1990.
- Hoffmann, P., W. Singer, and J. Bremer, Mean seasonal and diurnal variations of PMSE and winds from 4 years of radar observations at ALOMAR, *Geophys. Res. Lett.*, *26*, 1525–1528, 1999.
- Hoffmann, P., M. Rapp, A. Serafimovich, and R. Latteck, On the occurrence and formation of multiple layers of polar mesosphere summer echoes, *Geophys. Res. Lett.*, *32*, L05812, doi:10.1029/2004GL021409, 2005.
- Hogg, D., et al., An automatic profiler of the temperature, wind and humidity in the troposphere, *J. Clim. Appl. Meteorol.*, *22*, 807–831, 1983.
- Holton, J., and W. Wehrbein, A numerical model of the zonal mean circulation of the middle atmosphere, *Pageoph.*, *118*, 284–306, 1980.
- Holton, J. R., The role of gravity wave induced drag and diffusion in the momentum budget of the mesosphere, *J. Atmos. Sci.*, *39*, 791–799, 1982.
- Holton, J. R., *An introduction to dynamic meteorology*, Academic Press, New York, 1992.
- Holton, J. R., and M. J. Alexander, The role of waves in the transport circulation of the middle atmosphere, in *Atmospheric Science Across the Stratosphere*, edited by D. E. Siskind, S. D. Eckermann, and M. E. Summers, pp. 21–35, AGU, Washington, D.C., 2000.
- Houghton, J. T., The stratosphere and mesosphere, *Quart. J. R. Met. Soc.*, *104*, 1–29, 1978.
- Jiang, J. H., D. L. Wu, and S. D. Eckermann, Upper Atmosphere Research Satellite (UARS) MLS observation of mountain waves over the Andes, *J. Geophys. Res.*, *107*(D20), 8273, doi:10.1029/2002JD002091, 2002.
- Jiang, J. H., B. Wang, K. Goya, K. Hocke, S. D. Eckermann, J. Ma, D. L. Wu, and W. G. Read, Geographical distribution and interseasonal variability of tropical deep convection: UARS MLS observations and analyses, *J. Geophys. Res.*, *109*, D03111, doi:10.1029/2003JD003756, 2004.
- Khattatov, B. M., et al., Dynamics of the mesosphere and lower thermosphere as seen by MF radars and by HRDI/UARS, *J. Geophys. Res.*, *101*, 10,393–10,404, 1996.

- Kim, Y. C., and E. J. Powers, Digital bispectral analysis of self-excited fluctuation spectra, *Phys. Fluids*, *21*, 1452–1453, 1978.
- Kirkwood, S., V. Barabash, P. Chilson, A. Rechou, and K. Stebel, The 1999 PMSE season - its relation to wind, temperature, and water vapour, *Geophys. Res. Lett.*, *25*, 1867–1870, 1998.
- Kraus, J., *Radioastronomy*, McGraw-Hill, New York, 1966.
- Kumar, P., and E. Foufoula-Georgiou, Wavelet analysis for geophysical applications, *Rev. Geophys.*, *35*, 385–412, 1997.
- Kuo, F. S., J. Röttger, and H. Y. Lue, Propagation of gravity wave packets in the lower atmosphere observed by the SOUSY-Svalbard radar, *Chin. J. Phys.*, *41*(4), 309–325, 2003.
- Lafaysse, C. (Ed.), *Utilization of UHF/VHF radar wind profiler networks for improving weather forecasting in Europe*, European Commission, Luxembourg, 1994.
- Latteck, R., W. Singer, and H. Bardey, The Alwin MST radar - technical design and performance, in *Proceedings of the 14th ESA Symposium on European Rocket and Balloon Programmes and Related Research, Potsdam, Germany (ESA SP-437)*, edited by B. Kaldeich-Schürmann, pp. 179–184, ESA Publications Division, 1999.
- Lehmann, V., J. Dibbern, U. Görzdorf, J. Neuschaefer, and H. Steinhagen, The new operational UHF Wind Profiler Radars of the Deutscher Wetterdienst, in *Proceedings of the Sixth International Symposium on Tropospheric Profiling: Needs and Technologies, Leipzig, Germany*, edited by U. Wandinger, R. Engelmann, and K. Schmieder, pp. 489–491, Institute for Tropospheric Research, 2003.
- Leovy, C. B., Simple models of thermally driven mesospheric circulation, *J. Atmos. Sci.*, *21*, 327–341, 1964.
- Lilly, D. K., and P. J. Kennedy, Observations of a stationary mountain wave and its associated momentum flux and energy dissipation, *J. Atmos. Sci.*, *30*, 1135–1152, 1973.
- Lindzen, R. S., Turbulence and stress owing to gravity wave and tidal breakdown, *J. Geophys. Res.*, *86*, 9707–9714, 1981.
- Lübken, F.-J., Thermal structure of the Arctic summer mesosphere, *J. Geophys. Res.*, *104*, 9135–9149, 1999.
- McLandress, C., On the importance of gravity waves in the middle atmosphere and their parametrization in general circulation models, *J. Atmos. Solar Terr. Phys.*, *60*, 1357–1383, 1998.
- Merritt, D. A., A statistical averaging method for wind profiler doppler spectra, *J. Atmos. Ocean. Techn.*, *12*(5), 985–995, 1995.
- Morris, R. J., D. J. Murphy, I. M. Reid, D. A. Holdsworth, and R. A. Vincent, First polar mesosphere summer echoes observed at Davis, Antarctica, (68.2°S), *Geophys. Res. Lett.*, *31*, L16111, doi: 10.1029/2004GL020352, 2004.
- Müllemann, A., Temperaturen, Winde und Turbulenz in der polaren Sommermesosphäre, Ph.D. thesis, Universität Rostock, Germany, 2003.

- Nappo, C. J., *An introduction to atmospheric gravity waves*, Academic Press, New York, 2002.
- Nappo, C. J., and G. Chimonas, Wave exchange between the ground surface and a boundary-layer critical layer, *J. Atmos. Sci.*, *49*, 1075–1091, 1992.
- Nastrom, G. D., and D. C. Fritts, Sources of mesoscale variability of gravity waves. I: Topographic excitation, *J. Atmos. Sci.*, *49*, 101–110, 1992.
- Nastrom, G. D., M. R. Peterson, J. L. Green, K. S. Gage, and T. E. van Zandt, Sources of gravity wave activity seen in the vertical velocities observed by the Flatland VHF radar, *J. Appl. Meteorol.*, *29*, 783–792, 1990.
- Nikias, C. L., and A. P. Petropulu, *Higher-Order Spectra Analysis: A Nonlinear Signal Processing Framework*, Prentice-Hall, 1993.
- O’Sullivan, D., and T. J. Dunkerton, Generation of inertia-gravity waves in a simulated life cycle of baroclinic instability, *J. Atmos. Sci.*, *52*, 3695–3716, 1995.
- Pavelin, E., and J. Whiteway, Gravity wave interactions around the jet stream, *Geophys. Res. Lett.*, *29*(21), 2024, doi:10.1029/2002GL015783, 2002.
- Peters, D., and D. W. Waugh, Influence of barotropic shear on the poleward advection of upper-tropospheric air, *JAS*, *53*, 3013–3031, 1996.
- Peters, D., P. Hoffmann, and M. Alpers, On the appearance of inertia gravity waves on the north-easterly side of an anticyclone, *Meteor. Z.*, *12*(1), 25–35, 2003.
- Peters, D., C. Zülicke, P. Hoffmann, and A. Serafimovich, Inertia-gravity waves and their connection to breaking Rossby waves (LEWIZ), *AFO2000 - Newsletter*, *8*, 15–18, 2004.
- Plougonven, R., and H. Teitelbaum, Morphology of gravity-wave energy as observed from 4 years (1998–2001) of high vertical resolution U.S. radiosonde data, *Geophys. Res. Lett.*, *30*(18), 1954, doi:10.1029/2003GL017716, 2003.
- Plougonven, R., H. Teitelbaum, and V. Zeitlin, Inertia gravity wave generation by the tropospheric midlatitude jet as given by the Fronts and Atlantic Storm-Track Experiment, *J. Geophys. Res.*, *108*(D21), 4686, doi:10.1029/2003JD003535, 2003.
- Preusse, P., S. D. Eckermann, and D. Offermann, Comparisons of global distributions of zonal-mean gravity wave variance inferred from different satellite instruments, *Geophys. Res. Lett.*, *27*, 3877–3880, 2000.
- Queney, P., The problem of air flow over mountains: A summary of theoretical studies, *Bull. Amer. Meteor. Soc.*, *29*, 16–26, 1948.
- Rapp, M., and F.-J. Lübken, On the nature of PMSE: Electron diffusion in the vicinity of charged particles revisited, *J. Geophys. Res.*, *108*(D8), 8437, doi:10.1029/2002JD002857, 2003.
- Rapp, M., F.-J. Lübken, A. Müllemann, G. E. Thomas, and E. J. Jensen, Small scale temperature variations in the vicinity of NLC: Experimental and model results, *J. Geophys. Res.*, *107*(D19), 4392, doi:10.1029/2001JD001241, 2002.

- Rapp, M., F.-J. Lübken, P. Hoffmann, R. Latteck, G. Baumgarten, and T. Blix, PMSE dependence on aerosol charge number density and aerosol size, *J. Geophys. Res.*, *108*(D8), 8441, doi:10.1029/2002JD002650, 2003.
- Ratnam, M. V., G. Tetzlaff, and C. Jacobi, Global and seasonal variations of stratospheric gravity wave activity deduced from the CHAMP/GPS satellite, *J. Atmos. Sci.*, *61*, 1610–1620, 2004.
- Rauthe, M., U. Berger, M. Gerding, C. Fricke-Begemann, J. Höffner, and F.-J. Lübken, Lidar measurements and simulation of temperature gravity waves over Kühlungsborn (54°N) from the troposphere up to the lower thermosphere, *J. Geophys. Res.*, *submitted*, doi:10.10129/2005JD006220, 2005.
- Reid, I. M., R. Rüster, P. Czechowsky, and G. Schmidt, VHF radar measurements of momentum flux in the summer polar mesosphere over Andenes (69°N, 16°E), Norway, *Geophys. Res. Lett.*, *15*, 1263–1266, 1988.
- Röttger, J., Reflection and scattering of VHF radar signals from atmospheric refractivity structures, *Radio Sci.*, *15*, 259–276, 1980.
- Röttger, J., The instrumental principles of MST radars and incoherent scatter radars and the configuration of radar system hardware, in *Middle Atmosphere Program, Handbook for MAP*, vol. 30, edited by S. Fukao, pp. 54–113, SCOSTEP Secretariat, University of Illinois, 1989.
- Röttger, J., ST radar observations of atmospheric waves over mountainous areas: A review, *Ann. Geophysicae*, *18*, 750–765, 2000.
- Röttger, J., and M. F. Larsen, UHF/VHF radar techniques for atmospheric research and wind profiler applications, in *Radar in meteorology*, edited by D. Atlas, pp. 253–281, American Meteorological Society, Boston, 1990.
- Röttger, J., C. LaHoz, M. C. Kelley, U.-P. Hoppe, and C. Hall, The structure and dynamics of polar mesosphere summer echoes observed with the EISCAT 224 MHz radar, *Geophys. Res. Lett.*, *15*, 1353–1356, 1988.
- Rüster, R., VHF radar observations in the summer polar mesosphere indicating nonlinear interaction, *Adv. Space Res.*, *12*, 1085–1088, 1992.
- Rüster, R., Analysis and interpretation of VHF-radar data, *Ann. Geophys.*, *12*, 725–732, 1994a.
- Rüster, R., VHF radar observations of nonlinear interactions in the summer polar mesosphere, *J. Atmos. Terr. Phys.*, *56*, 1289–1299, 1994b.
- Sato, K., A statistical study of the structure, saturation and sources of inertia-gravity waves in the lower stratosphere observed with the MU radar, *J. Atmos. Terr. Phys.*, *56*, 755–774, 1994.
- Sato, K., D. J. O’Sullivan, and T. J. Dunkerton, Low-frequency inertia-gravity waves in the stratosphere revealed by three week continuous observation with the MU radar, *Geophys. Res. Lett.*, *24*, 1739–1742, 1997.
- Sawyer, J. S., The introduction of the effects of topography into methods of numerical forecasting, *Quart. J. R. Met. Soc.*, *85*, 31–43, 1959.

- Schmidlin, F. J., H. S. Lee, and W. Michel, Global and seasonal variations of stratospheric gravity wave activity deduced from the CHAMP/GPS satellite, *J. Geophys. Res.*, *96*, 22,673–22,682, 1991.
- Schöch, A., G. Baumgarten, D. C. Fritts, P. Hoffmann, A. Serafimovich, L. Wang, P. Dalin, A. Müllemann, and F. J. Schmidlin, Gravity waves in the troposphere and stratosphere during the MaC/MIDAS summer rocket program, *Geophys. Res. Lett.*, *31*, L24S04, doi:10.1029/2004GL019837, 2004.
- Schoeberl, M. R., and D. F. Strobel, The zonally averaged circulation of the middle atmosphere, *J. Atmos. Sci.*, *35*, 577–591, 1978.
- Schöllhammer, K., Klimatologie der Schwerewellenaktivität in den mittleren Breiten, Ph.D. thesis, Freie Universität Berlin, Germany, 2002.
- Scorer, R. S., Theory of waves in the lee of mountains, *Quart. J. R. Met. Soc.*, *75*, 41–56, 1949.
- Serafimovich, A., P. Hoffmann, D. Peters, and V. Lehmann, Investigation of inertia-gravity waves in the upper troposphere / lower stratosphere over Northern Germany observed with collocated VHF/UHF radars, *Atmos. Chem. Phys.*, *5*, 295–310, 2005.
- Singer, W., D. Keuer, and W. Eriksen, The ALOMAR MF radar: Technical design and first results, in *Proceedings of the 13th ESA Symposium on European Rocket and Balloon Programmes and Related Research, Oeland, Sweden (ESA SP-397)*, edited by B. Kaldeich-Schürmann, pp. 101–103, ESA Publications Division, 1997.
- Smith, R. B., The influence of mountains on the atmosphere, *Adv. Geophys.*, *21*, 87–230, 1979.
- Smith, R. B., Hydrostatic air flow over mountains, *Adv. Geophys.*, *31*, 1–38, 1989.
- Stobie, J. G., F. Einaudi, and L. W. Uccellini, A case study of gravity waves - convective storms interactions: 9 May 1997, *J. Atmos. Sci.*, *40*, 2804–2830, 1983.
- Swanson, K. L., P. J. Kushner, and I. M. Held, Dynamics of barotropic storm tracks, *J. Atmos. Sci.*, *54*, 791–810, 1997.
- Swenson, G. R., and P. J. Espy, Observations of two-dimensional airglow structure and Na density from the ALOHA, October 9, 1993, "Storm Flight", *Geophys. Res. Lett.*, *22*, 2845–2848, 1995.
- Tatarskii, V. I., *Wave propagation in a turbulent medium*, McGraw-Hill, New York, 1961.
- Taylor, M. J., and F. J. Garcia, A two-dimensional spectral analysis of short period gravity waves imaged in the OI(557.7 nm) and near infrared OH nightglow emissions over Arecibo, Puerto Rico, *Geophys. Res. Lett.*, *22*, 2473–2476, 1995.
- Teitelbaum, H., and F. Vial, On tidal variability induced by nonlinear interaction with planetary waves, *J. Geophys. Res.*, *96*, 14,169–14,178, 1991.
- Teitelbaum, H., F. Vial, A. H. Manson, R. Giraldez, and M. Masebeuf, Non-linear interactions between the diurnal and semidiurnal tides: Terdiurnal and diurnal secondary waves, *J. Atmos. Terr. Phys.*, *51*, 627–634, 1989.

- Thomas, L., R. Worthington, and A. J. McDonald, Inertia-gravity waves in the troposphere and lower stratosphere, *Ann. Geophysicae*, 17, 115–121, 1999.
- Thompson, R. O. R. Y., Observation of inertial waves in the stratosphere, *Quart. J. R. Met. Soc.*, 104, 691–698, 1978.
- Torrence, C., and G. P. Compo, A practical guide to wavelet analysis, *Bull. Amer. Meteor. Soc.*, 79(1), 61–78, 1998.
- Trexler, C. M., and S. E. Koch, The life cycle of a mesoscale gravity wave as observed by a network of doppler wind profilers, *Mon. Weather Rev.*, 128, 2423–2446, 2000.
- Tsuda, T., M. Nishida, C. Rocken, and R. H. Ware, A global morphology of gravity wave activity in the stratosphere revealed by the GPS Occupation data (GPS/MET), *J. Geophys. Res.*, 105(D6), 7257–7274, 2000.
- Uccellini, L. W., A case study of apparent gravity wave initiation of severe convective storms, *Mon. Weather Rev.*, 103, 497–513, 1975.
- Uccellini, L. W., and S. E. Koch, The synoptic setting and possible energy sources for mesoscale wave disturbances, *Mon. Weather Rev.*, 115, 721–729, 1987.
- Vial, F., and J. M. Forbes, Recent progress in tidal modelling, *J. Atmos. Terr. Phys.*, 51, 663–671, 1989.
- Vincent, R., and D. Fritts, A climatology of gravity wave motions in the mesopause region at Adelaide, Australia, *J. Atmos. Sci.*, 44, 748–760, 1987.
- Vincent, R. A., and M. J. Alexander, Gravity waves in the tropical lower stratosphere: An observational study of seasonal and interannual variability, *J. Geophys. Res.*, 105, 17,971–17,982, 2000.
- Vincent, R. A., and I. M. Reid, HF Doppler measurements of mesospheric gravity wave momentum fluxes, *J. Atmos. Sci.*, 40, 1321–1333, 1983.
- Wang, L., and M. A. Geller, Morphology of gravity-wave energy as observed from 4 years (1998–2001) of high vertical resolution U.S. radiosonde data, *J. Geophys. Res.*, 108(D16), 4489, doi:10.1029/2002JD002786, 2003.
- Wang, L., M. A. Geller, and M. J. Alexander, Spatial and temporal variations of gravity wave parameters. Part i: Intrinsic frequency, wavelength, and vertical propagation direction, *J. Atmos. Sci.*, 62, 125–142, 2005.
- Warner, C. D., and M. E. McIntyre, Toward an ultra-simple spectral gravity wave parameterization for general circulation models, *Earth Plan. Space*, 51, 475–484, 1999.
- Wu, D. L., and J. W. Waters, Satellite observations of atmospheric variances: A possible indication of gravity waves, *Geophys. Res. Lett.*, 23(24), 3631–3634, 1996.
- Wu, Y.-F., J. Xu, H.-U. Widdel, and F.-J. Lübken, Mean characteristics of the spectrum of horizontal velocity in the polar summer mesosphere and lower thermosphere observed by foil chaff, *J. Atmos. Solar Terr. Phys.*, 63, 1831–1839, 2001.
- Zhang, F., S. Wang, and R. Plougonven, Uncertainties in using the hodograph method to retrieve gravity wave characteristics from individual soundings, *Geophys. Res. Lett.*, 31, L11110, doi:10.1029/2004GL019841, 2004.

- Zink, F., Gravity waves and turbulence in the lower atmosphere, Ph.D. thesis, University of Adelaide, Australia, 2000.
- Zink, F., and R. Vincent, Wavelet analysis of stratospheric gravity wave packets over Macquarie Island, *J. Geophys. Res.*, *106*, 10,275–10,288, 2001.
- Zülicke, C., and D. Peters, Inertia-gravity waves driven by a poleward breaking Rossby wave, *J. Atmos. Sci.*, *submitted*, 2004.

Acknowledgements

First of all I would like to thank Dr. Peter Hoffmann for his very helpful assistance in atmospheric physics and related fields, friendly support and encouragement during my candidature. He often had the right idea at the right time to proceed successfully. I also thank Prof. Franz-Josef Lübken, Prof. Jürgen Röttger, Prof. Thomas Hauf reviewing this thesis. Special thanks to Prof. Franz-Josef Lübken and Dr. Jürgen Bremer for very careful reading and insightful comments and suggestions to the thesis, which helped me in improving it more and more. For valuable discussions I thank Priv. Doz. Dr. habil. Dieter Peters, who initiated the LEWIZ project to investigate the connection between gravity waves and breaking Rossby wave events resulting in a fruitful collaboration between theoretical work and experimental studies. For their efforts to read and correct English grammar in the manuscript of this thesis I have to thank Maureen and Fridolin Kathan.

Helpful discussions with Dr. Christoph Zülicke, Priv. Doz. Dr. habil. Markus Rapp, Armin Schöch and Dr. Michael Gerding on gravity waves and PMSE are highly appreciated.

I am greatly indebted to all my friends and colleagues of the Radar soundings group specially to Dr. Norbert Engler, Olof Zeller for the extremely helpful and friendly working atmosphere, to Dr. Ralph Latteck, Dr. Marius Zecha, Dr. Werner Singer, Dieter Keuer, and Jens Wedrich. Special thanks to Ursula Scholze, Jutta Schacht, Thomas Barth, and Joerg Trautner, our "party-team", whose help in diversity of working atmosphere is invaluable.

I would also like to thank the staff of IAP and the Andoya rocket range for their management and permanent support to run the VHF and MF radar and to process the data.

I also thank Dr. Heiner Körnich and Boris Strelnikov for all his friendship and support to fix problems that came up during programming and manuscript preparations.

Thanks also to Thomas Linow and Martin Dueffer for excellent computer support. My appreciation goes to all wonderful people I met here, specially to Roswitha Mehl and Marion Lange, who helped in small but important ways.

I had the great opportunity to join Third International School on Atmospheric Radars (ISAR) in Trieste. The ISAR in 2002 was organized with the kind support of the Abdus Salam International Centre for Theoretical Physics. Thanks to everybody who contributed to this project. Specially, I would like to thank Prof. J. Röttger, Prof. W. Hocking, Prof. S. Radiella, Prof. R. Palmer, Dr. Ph. Chilson, Prof. N. Rao, Prof. Sh. Fukao for the interesting, practical and comprehensive lectures on radar technique.

Outside of Institute, I am indebted to my friends Zaruba Alexander, Ludmila and Sven Kuhlmann, Irina Strelnikova and Boris Strelnikov, Mykhaylo Grygalashvyly, Patricia and Peter Bendix. Only due to your friendship I enjoyed my stay in Germany as much as I did. I further greatly acknowledge the friendly support of Dr. Peter Hoffmann to solve all day-to-day personal problems which a foreigner have coming abroad.

I owe my warmest thanks to my parents, Galina Mihailovna and Valerii Ivanovich, my brother Alexander for their support and encouragement throughout my everlasting studies. Finally, my heartfelt gratitude is due to my loving wife Elena and to our little son Egor for the incredible amount of patience they have with me. Without your help finishing this thesis would have been a lot harder.

Summary

This work focuses on the investigation of inertia-gravity wave properties based on continuous radar measurements of zonal and meridional winds. Gravity wave parameters have been estimated at different locations separately and by a complex cross-spectral analysis of the data of collocated radars. The temporal-spatial behavior of gravity waves is examined by the wavelet analysis.

A case study carried out in a region with no large orography (Northern Germany) at Kühlungsborn (54.1°N , 11.8°E) and Lindenberg (52.2°N , 14.1°E) shows the appearance of strong inertia-gravity waves in connection with Rossby wave breaking events. For the campaign in December 1999, two kinds of gravity waves occurring simultaneously are detected with horizontal wavelengths in the order of about 200-300 kilometers. One wave is generated by a jet stream in the tropopause region, leading to a downward energy propagation in the troposphere and moving against the mean background wind, whereas the other, slightly weaker wave moves downwind and shows at both locations upward directed energy propagations, so that this wave is probably generated by a frontal activity or deep convection in the boundary layer. Additionally, the generation of a secondary wave by non-linear wave-wave interactions has been proved by the bispectral analysis applied on the data of a campaign in February 2002 at Kühlungsborn during another Rossby wave breaking event.

To investigate the generation and propagation of gravity waves up to the polar mesosphere and additionally influenced by orographically excited mountain waves over Northern Scandinavia, in the frame of the international MaCWAVE/MIDAS program, two campaigns including in-situ rocket and radiosonde measurements and ground-based lidar and radar observations were carried out at Andenes (69.2°N , 16.0°E) and Kiruna (67.9°N , 21.9°E) in summer 2002 and winter 2003. During the summer campaign, separate analyses and a complex cross-spectral analysis show the presence of short-periodic as well as long-periodic waves which are excited in the troposphere or lower stratosphere region and at the boundary layer, respectively. The analyses of the winter campaign in January 2003 show the presence of a long period horizontal gravity wave propagating nearly in the same direction at both locations with a higher wave activity on the East-side of the Scandinavian mountain ridge at Kiruna. It has been shown that this gravity wave is generated in the tropopause region in connection with a strong eastward directed jet. Detailed gravity wave analyses based on the mesoscale MM5 model data for the winter MaCWAVE/MIDAS campaign have been used for comparison with experimentally obtained result.

Experimental evidence was found to confirm microphysical assumptions that observed multiple PMSE layer structures in the mesosphere are mainly caused by layering of ice particles in the cold phases of long period gravity waves. Additionally, a gravity wave climatology based on continuous wind measurements with the MF-Radar in Andenes confirms the strongest correlation between the daily occurrence rate of multiple PMSE layers and the variances of the meridional winds for periods between 5 – 7 h at an altitude of 86 km in the center of the PMSE layers.

Zusammenfassung

Diese Arbeit beschäftigt sich mit der Untersuchung der Eigenschaften von Trägheitsschwerewellen auf der Basis kontinuierlicher Radarmessungen der zonalen und meridionalen Winde. Schwerewellenparameter werden für verschiedene Radar-Standorte separat bestimmt sowie zusätzlich durch Anwendung einer komplexen Kreuz-Spektral-Analyse der Daten benachbarter Radars. Zur Berücksichtigung der Raum-Zeit-Struktur der Schwerewellen wird die Wavelet-Analyse eingesetzt.

In einer Fallstudie in einem Gebiet ohne wesentliche Orography (Norddeutschland) in Kühlungsborn (54.1°N , 11.8°O) und Lindenberg (52.2°N , 14.1°O) wurden starke Trägheitsschwerewellen in Verbindung mit brechenden Rossbywellen nachgewiesen. In dem untersuchten Fall im Dezember 1999 treten gleichzeitig zwei Typen von Schwerewellen mit horizontalen Wellenlängen von ca. 200–300 Kilometer auf. Eine Welle wird durch den Strahlstrom in der Tropopausenregion erzeugt, sie bewegt sich gegen den Grundstrom und zeigt in der Troposphäre eine abwärtsgerichtete Energieausbreitung. Der andere, etwas schwächere Wellentyp bewegt sich in Windrichtung und zeigt an beiden Messorten eine aufwärts gerichtete Energieausbreitung, so dass die Quelle dieser Welle in der Grenzschicht (Frontensystem, Konvektion) liegen muss. Während einer weiteren Messkampagne im Februar 2002 in Kühlungsborn zur Untersuchung des Zusammenhanges von Schwerewellen mit brechenden Rossbywellen wurde die Anregung einer sekundären Schwerewelle durch nicht-lineare Welle-Welle-Wechselwirkung mit Hilfe einer Bispektralanalyse nachgewiesen.

Zur Untersuchung der Anregung und Ausbreitung von Schwerewellen bis in die polare Mesosphäre unter zusätzlichem Einfluss orografisch angeregter Gebirgswellen über Nordskandinavien im Rahmen des internationalen MaCWAVE/MIDAS Programms wurden zwei Kampagnen mit direkten Raketen- und Radiosondenmessungen und verschiedenen bodengebundenen Lidar- und Radarmessungen in Andenes (69.2°N , 16.0°O) und Kiruna (67.9°N , 21.9°O) im Sommer 2002 und Winter 2003 durchgeführt. Separate Analysen und eine komplexe Kreuz-Spektral-Analyse während der Sommermesskampagne zeigen sowohl kurzperiodische Wellen, die in der Troposphäre / unteren Stratosphäre angeregt werden, als auch lang-periodische Wellen, die in der unteren Troposphäre bzw. in der Grenzschicht ihren Ursprung haben müssen. Aus den Analysen der Winterkampagne im Januar 2003 wird eine lang-periodische Schwerewelle nachgewiesen, die an beiden Messorten nahezu die gleiche Ausbreitungsrichtung aufweist, und eine stärkere Wellenaktivität an der Ostseite des Skandinavischen Gebirgsrückens in Kiruna zeigt. Diese Schwerewelle wird in der Tropopausenregion in Verbindung mit einem starken Westwind angeregt. Detaillierte Schwerewellenanalysen, basierend auf den Daten mit dem mesoskaligen MM5-Modell für die MaCWAVE/MIDAS-Winterkampagne, werden zum Vergleich mit den experimentell erhaltenen Schwerewellenparameter genutzt.

Auf der Basis mesosphärischer VHF-Radar-Windmessungen wurde im Rahmen einer Fallstudie ein experimenteller Nachweis zur Bestätigung mikrophysikalischer Simulationen gegeben, nach der beobachtete PMSE-Mehrfachschichten in der Mesosphäre hauptsächlich durch die Schichtung von Eis-Partikel in den kalten Phasen lang-periodischer Schwerewellen verursacht werden. Zur klimatologischen Untersuchung dieses Zusammenhanges wurden die Varianzen der kontinuierlichen Winde aus den MF-Radar-Messungen in Andenes des Sommers 2001 untersucht. Dabei zeigte sich die stärkste Korrelation zwischen der täglichen Rate des Auftretens mehrfacher PMSE-Schichten mit der Varianz der meridionalen Winde für Perioden zwischen 5 – 7 h in 86 km Höhe, im Zentrum der PMSE-Schichten.

Selbstständigkeitserklärung

Hiermit versichere ich, dass ich die vorliegende Arbeit selbstständig angefertigt und ohne fremde Hilfe verfasst habe, keine außer den von mir angegebenen Hilfsmitteln und Quellen dazu verwendet habe und die den benutzten Werken inhaltlich oder wörtlich entnommenen Stellen als solche kenntlich gemacht habe.

Die Arbeit wurde bisher weder im Inland noch im Ausland in gleicher oder ähnlicher Form einer anderen Prüfungsbehörde vorgelegt. Weiterhin erkläre ich, dass ich ein Verfahren zur Erlangung des Doktorgrades an keiner anderen wissenschaftlichen Einrichtung beantragt habe.

Kühlungsborn, den 27. Mai 2005

Lebenslauf

Name	Andrei Serafimovich
Geburtsdatum	29.03.1976
Geburtsort	Borisov, Weißrussland
Familienstand	verheiratet
Staatsangehörigkeit	Weißrussland
Wohnsitz	Minsk, Weißrussland
Nebenwohnsitz	Kühlungsborn
1983-1991	Grundschule in Borisov
1991-1993	Gymnasium in Borisov
Juni 1993	Abitur am Gymnasium in Borisov
1993 – 1998	Studium an der Belarusian State University, Minsk, Weißrussland, Studiengang: Diplom Physik
1997 – 1998	Diplomarbeit in Physik am Institut für angewandte Physik, Akademie der Wissenschaften, Minsk, Weißrussland Diplomarbeitsthema: „Investigation of electromagnetic losses under magnetic reversal with toroidal samples“
Juni 1998	Diplom in Physik
1997 – 1998	Studium an der Belarusian State University, Minsk, Weißrussland, Studiengang: Wirtschaftskybernetik
1998 – 2000	Wissenschaftlicher Angestellter am Institut für angewandte Physik, Akademie der Wissenschaften, Minsk, Weißrussland
2001 – 2005	Promotion im Studienfach Physik am Leibniz-Institut für Atmosphärenphysik an der Universität Rostock e.V., Anfertigung der Dissertation